A Systems Approach to Cardiovascular Health and Disease with a Focus on Aortic Wave Dynamics

Thesis by
Niema Mohammed Pahlevan

In Partial Fulfillment of the Requirements for the degree
of
Doctor of Philosophy

CALIFORNIA INSTITUTE OF TECHNOLOGY
Pasadena, California
2013
(Defended April 22, 2013)

I dedicate this thesis to my parents for their unconditional love and support.

ACKNOWLEDGEMENTS

I wish to express my gratitude to all of my teachers and mentors from my first grade teacher *Mrs Tahamtan* to my PhD advisor *Professor Mory Gharib*. I am particularly grateful to *Professor Mory Gharib* who provided the mentorship that helped me to become a creative and independent researcher. I would like to express my sincere thanks to my committee members, *Professor Tom Hou, Professor Niles Pierce,* and *Professor Guruswami Ravichandran*. I am also honored to have *Professor Fazle Hussain* (U of Houston &Texas Tech.) in my committee. I appreciate what I have learned from them. I am also grateful to our collaborators at USC, *Dr. Ray Matthews* and *Dr. Robbin Cohen,* whose insight and guidance are the essential part of this thesis. I highly appreciate the help and guidance of *Dr. Danny Petrasek* (Caltech &UCLA), *Dr Behrooz Sharifi* (Cedar Sinai Heart Institute), *Dr. Masoud Beizaie,* and *Professor Tim Colonius*.

I would like to thank *Professor Seyed Ahmad Nourbakhsh* (U of Tehran) who set me on the path that brought me to this point in my academic life. I would like to thank my MS advisor *Professor C.T. Lin* (CSUN) for teaching me how to perform a scientific research. I would like to thank *Professor Larry Caretto* (CSUN) who introduced me to the art of scientific computing. I would like to thank *Professor Richard Ehrgott* (CSUN) for teaching me how to use analytical approaches in research. I am grateful to my friend *Dr. Ben Lin* (Yale & Caltech) who taught me the basics of clinical research. I am also thankful to *Sid Mohasseb* for teaching me how to think as an entrepreneur.

I highly appreciate the support of all of my dear friends: *Mahdi Etemadi, Connie Nichole Etemadi, Alborz Mahdavi, Mohsen Chitsaz, Aydin Babakhani, Sepideh Nouri, Peyman Tavallali, Faisal Amlani, Manuel Lombardini, Farshid Roumi,* and *Shahab Mahdavi*. I am also thankful to *Rana Ahmadi* who was always supportive during our time together.

I would also like to thank my friends in Gharib's group who trained me on various experimental techniques: *Dr. Rob McGrath* (rest in peace), *Dr. Kim Daegyoum, Dr. Emilio Graff, Dr. Arian Forouhar,* and *Hesham Azizgolshani*. I would specially like to thank my friends *Dr. Derek Rinderknecht, Professor Arash Kheradvar* (UCI), and *Professor Ehsan Jabbarzadeh* (USC) who I have the opportunity to work with and learn from.

I am grateful to all the past and present staff of the Caltech specially *Martha Salcedo*, *Angie Gango*, and *Natalie Gilmore*. I am particularly grateful to *Dean Shepherd* for his support during my difficult times.

I would like to express my deepest gratitude and warmest appreciation to my family specially to my parents, *Kiarash Pahlevan* and *Nayereh Aghaei*, to my brother, *Sohrab*, and to my sister, *Nakta*.

ABSTRACT

Cardiovascular diseases (CVDs) have reached an epidemic proportion in the US and worldwide with serious consequences in terms of human suffering and economic impact. More than one third of American adults are suffering from CVDs. The total direct and indirect costs of CVDs are more than $500 billion per year. Therefore, there is an urgent need to develop noninvasive diagnostics methods, to design minimally invasive assist devices, and to develop economical and easy-to-use monitoring systems for cardiovascular diseases. In order to achieve these goals, it is necessary to gain a better understanding of the subsystems that constitute the cardiovascular system. The aorta is one of these subsystems whose role in cardiovascular functioning has been underestimated. Traditionally, the aorta and its branches have been viewed as resistive conduits connected to an active pump (left ventricle of the heart). However, this perception fails to explain many observed physiological results. My goal in this thesis is to demonstrate the subtle but important role of the aorta as a system, with focus on the wave dynamics in the aorta.

The operation of a healthy heart is based on an optimized balance between its pumping characteristics and the hemodynamics of the aorta and vascular branches. The delicate balance between the aorta and heart can be impaired due to aging, smoking, or disease. The heart generates pulsatile flow that produces pressure and flow waves as it enters into the compliant aorta. These aortic waves propagate and reflect from reflection sites (bifurcations and tapering). They can act constructively and assist the blood circulation. However, they may act destructively, promoting diseases or initiating sudden cardiac death. These waves also carry information about the diseases of the heart, vascular disease, and coupling of heart and aorta. In order to elucidate the role of the aorta as a dynamic system, the interplay between the dominant wave dynamic parameters is investigated in this study. These parameters are heart rate, aortic compliance (wave speed), and locations of reflection sites. Both computational and experimental approaches have been used in this research. In some cases, the results are further explained using theoretical models.

The main findings of this study are as follows: (i) developing a physiologically realistic outflow boundary condition for blood flow modeling in a compliant vasculature; (ii) demonstrating that pulse pressure as a single index cannot predict the true level of pulsatile workload on the left ventricle; (iii) proving that there is an optimum heart rate in which the pulsatile workload of the heart is minimized and that the optimum heart rate shifts to a higher value as aortic rigidity increases; (iv) introducing a simple bio-inspired device for correction and optimization of aortic wave reflection that reduces the workload on the heart; (v) deriving a non-dimensional number that can predict the optimum wave dynamic state in a mammalian cardiovascular system; (vi) demonstrating that waves can create a pumping effect in the aorta; (vii) introducing a system parameter and a new medical index, Intrinsic Frequency, that can be used for noninvasive diagnosis of heart and vascular diseases; and (viii) proposing a new medical hypothesis for sudden cardiac death in young athletes.

TABLE OF CONTENTS

LIST OF ILLUSTRATIONS

LIST OF TABLES

Chapter 1

INTRODUICTION

1.1 Motivation

Cardiovascular diseases (CVDs) are the underlying cause of about one out of every three deaths in the United States each year. Thirty-four percent of American adults are suffering from one or more types of CVD. In 2010, the total direct and indirect cost of CVDs was approximately $503 billion [1]. Certainly, there is an urgent need to develop new methods and devices for diagnosing and monitoring CVDs. In order to meet this need, it is necessary to gain a better understanding of the dynamics of the systems that constitute the cardiovascular system. Traditionally, the cardiovascular system has been viewed as an active pump connected to a passive vascular network. In this thesis, I looked at the aorta and its vascular branches as a system with a dynamic behavior. This new perspective enables us to achieve the following: (i) designing new approaches for therapeutics; (ii) developing new noninvasive methods for diagnostics; (iii) finding optimization criteria in the mammalian cardiovascular system; (iv) explaining paradoxical results in medical literature; and (v) proposing solutions for unsolved medical problems.

1.2 Systems Approach

The systems approach is a method of studying complex physiological and biological systems where global behaviors, properties and dynamics of the system are considered in an integrated context [2]. In this respect, the systems approach contrasts with the reductionist approach where individual components and local effects are being studied. The reductionist approach has dominated biology and physiology for nearly a century. While this approach has produced a treasure of information, it commonly fails when scaling up to macro-physiological systems. Here, I apply a systems approach to the cardiovascular system with a focus on the wave dynamics in the aorta. This thesis shows how such an approach helps us achieve the aforementioned goals.

1.3 Basic Cardiovascular Physiology and Anatomy

The cardiovascular system is composed of a four-chambered pump (the heart) and two networks of vessels, systemic vasculature and pulmonary vasculature. The heart provides the required energy to propel the blood throughout the vascular trees. The systemic vascular vessels deliver the blood, which contains nutrient and oxygen, to all organs, tissues, and cells in the body, and remove waste and carbon dioxide from them. The pulmonary vasculature works with the pulmonary system to exchange oxygen and carbon dioxide. The cardiovascular system also cooperates closely with the endocrine system, immune system, renal system, and gastrointestinal system closely [3].

1.3.1 Heart

The heart is a muscular pump which consists of four chambers and four valves. It pumps the blood through the systemic vascular tree by contraction of the left ventricle through the aortic valve and aorta (the largest artery of the body and the focus of this research). Blood returns to the right atrium by using veins. After passing through the tricuspid valve, blood is sent to the pulmonary vascular bed (lung) by contraction of the right ventricle and opening and closure of the pulmonary valve (Figure 1.1).

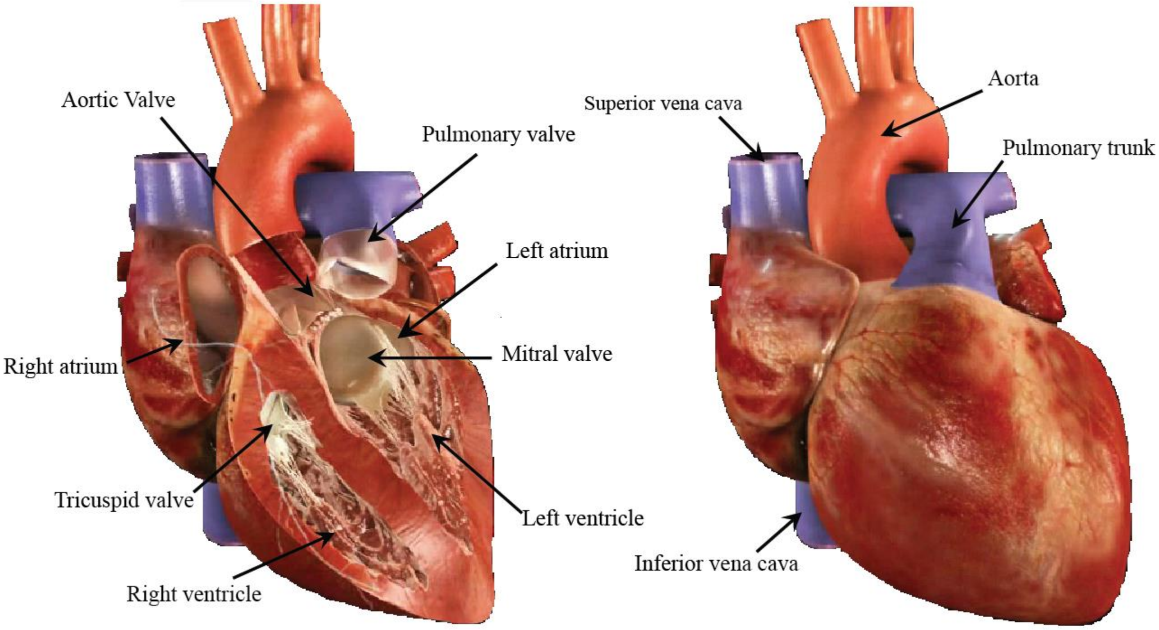

Figure 1.1: Human heart. Figure is adapted from Parker [4].

Four important factors have been introduced which quantify the performance and output of the heart. These factors are cardiac output (CO), stroke volume (SV), heart rate (HR), and ejection fraction (EF).

Stroke volume is the volume of blood that goes out in each contraction. It can be calculated by subtraction of the end systolic volume (ESV) from the end diastolic volume (EDV). The heart rate is the frequency of the heart's contraction. For humans, it ranges from 40 to 200 beats per minute (bpm). Cardiac output (CO) is defined as the volume of the blood sent out per minute. CO can be calculated by multiplication of the stroke volume and the heart rate. Ejection fraction is the ratio of stroke volume to end-diastolic volume and is an index for estimation of myocardial contractility.

The relationships between these factors are represented by the following equations [3]:

$$SV = EDV - ESV, \tag{1.1}$$

$$CO = (SV)(HR), \tag{1.2}$$

$$\left(EF = \frac{SV}{EDV}\right) \propto Contractility\,. \tag{1.3}$$

1.3.2 Vascular System

The vascular system is composed of two parallel circulation paths, Pulmonary and Systemic, each with two different kinds of conduits: arteries and veins (Figure 1.2). Pulmonary circulation refers to the vessels that transfer poorly oxygenated blood from the right ventricle to the lungs and returns the richly oxygenated blood back to the heart. The systemic circulation is a part of the vascular system that delivers richly oxygenated blood from the left ventricle to different organs and tissues through the systemic arteries and returns it to the right atrium through systemic veins [3]. Arteries and veins are different in both structure and duty. Arteries have relatively thick and muscular walls which enable them to tolerated high pressure conditions. On the other hand, veins are noticeably thinner and hence more compliant than the arteries. The blood pressure in veins is a lot lower than in arteries (especially large arteries); as a result, the blood flow is smoother and slower. Large veins have valves that prevent blood flowing back in the opposite direction[3].

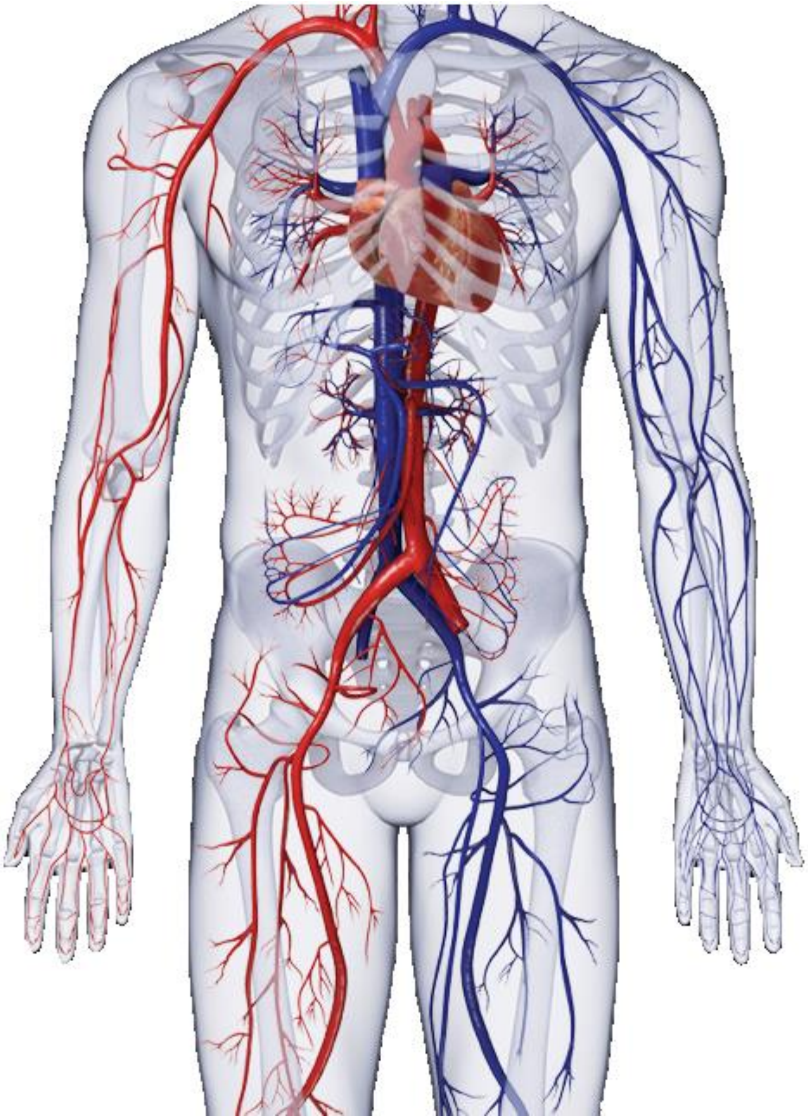

Figure 1.2: Human vascular system. Reds are arteries and blues are veins. Figure is adopted from Parker [4].

1.3.3 Aorta

The main focus of this research is the largest vessel of the systemic circulation or the aorta (see Figure 1.3). The initial part of the aorta, after the sinuses of valsalva, is called the ascending aorta. It is approximately 3 cm long and fairly straight. At the end of the ascending aorta, it curves 180 degrees in a three-dimensional pattern, having three branches (right subclavian artery, common carotid, and left subclavian). This curved vessel is named the aortic arch. It then goes straight down toward the abdomen passing the diaphragm. At the end of the abdominal aorta, it terminates into two iliac arteries. The bifurcation angles of the aorta's branches are different from one to another. The bifurcation angle is shown to be one of the important factors in energy dissipation and wave reflection at the bifurcation site [5].

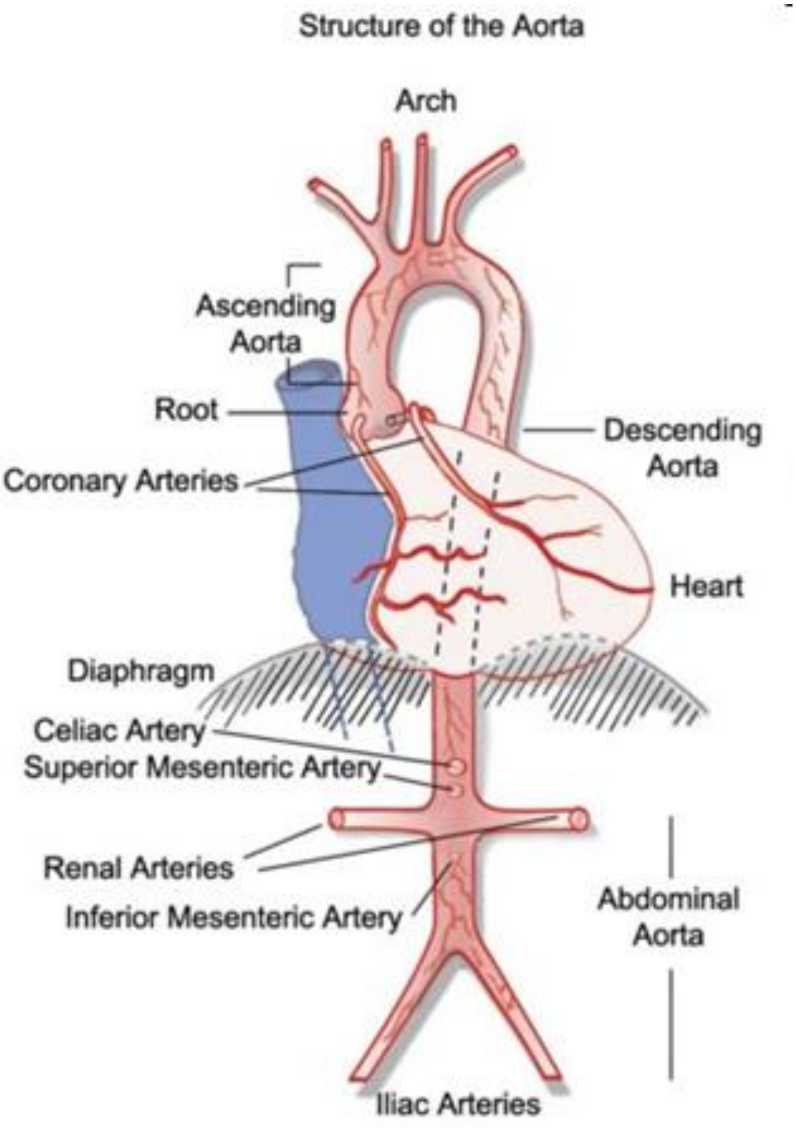

Figure 1.3: Human aorta and its main branches. Image from Cedars-Sinai Heart Institute.

The blood flow in the aorta is pulsatile and operates at the highest level of the body's blood pressure. The aorta is more compliant than other arteries and arterioles. It tapers along its length and its wall rigidity increases as it goes away from the heart. The rate of the tapering is slightly variable between animals. Although all arteries taper, the total cross-sectional area of the systemic vascular bed increases as it travels away from the heart [6, 7].

1.3.4 Blood

Blood is a viscoelastic, non-Newtonian, two-phase and shear-thinning fluid. However, in large and medium arteries blood acts as a Newtonian, one phase, and incompressible fluid [6]. The major task of blood is to transport oxygen and nutrients to the tissues and remove CO_2 and waste from them. In addition, blood contributes in homeostasis by distributing water, solutes and heat. The major components of blood are Erythrocytes (red blood cells), Leukocytes (white blood cells), and platelets [3].

1.4 Impedance Pump and Wave Dynamics in a Compliant Tube

The wave dynamics in a compliant tube is a complex nonlinear phenomenon that includes wave interactions and resonance [8-12]. Waves in compliant tubes can create a pumping effect as first observed by Liebau [13]. In 1954, Liebau recognized it is possible to flow a fluid against a pressure gradient by compressing an elastic tube in a periodic fashion at an asymmetric location. He suggested that elasticity, inertia, and viscosity of the tube are the dominant factors that affect the performance of the device. However, he did not explain the role of each parameter. The study of the physics of wave propagation in fluid filled elastic tubes goes back to nineteenth century when Lamb and Korteweg were working on this phenomenon [14]. This study was carried on by Womersley, Morgan, and Kiely in the 1950’s ,who used linear approximation theory to investigate the effect of viscosity on flow behavior and wave propagation in elastic tubes[15, 16].

In its simplest form, an impedance pump (Liebau pump) is composed of a compliant tube connected to two rigid tubes at both ends, and a pincher. The pincher hits the compliant tube and creates waves. These waves propagate toward both ends, where they reflect upon the impact on the rigid boundary (Figure 1.4). The wave propagation and reflection in the elastic tube create wave dynamics which may produce pumping effects. The direction and magnitude of the net flow in the impedance pump depends on the state of the wave dynamics, which are mainly dominated by three factors: (1) material properties of the compliant tube (that defines the wave speed), (2) frequency of the excitation (pincher frequency), and (3) locations of reflection sites (distance between pincher and rigid tubes) [8-11, 17-19].

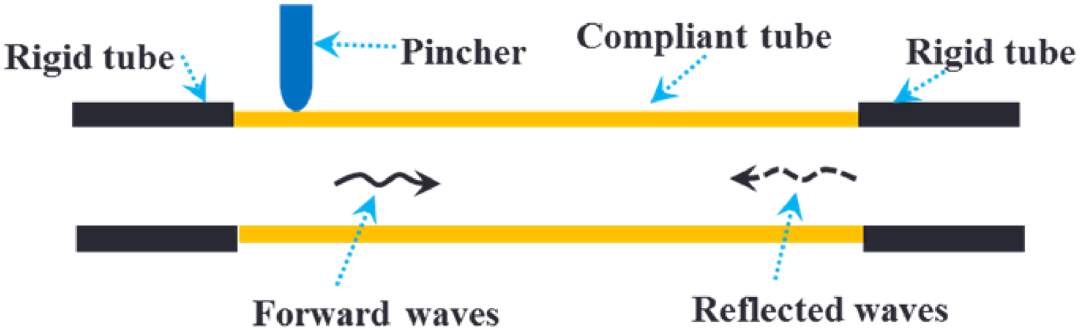

Figure 1.4: Schematic of a simple impedance pump.

Despite the complicated physics of the impedance pump, it provides a simple message: waves can assist circulating fluid flow in a compliant tubing system in a certain direction. The direction and the magnitude of the net flow depend on the wave dynamic characteristics which show nonlinear-type behavior and resonance [8, 11, 20].

1.4 Thesis Outline

A realistic outflow boundary model for blood flow modeling in compliant vessels is introduced in Chapter 2. This boundary model takes into account the important physiological effects of the eliminated vasculature. In fact, this boundary condition is a system equivalent to the truncated vascular network. The advantages of this outflow boundary condition over other existed boundary conditions will be discussed in this chapter.

It will be shown in Chapter 3 that using pulse pressure (*pp*) as a single index (reductionist approach) can result in an underestimation of the level of left ventricular (LV) workload under abnormal wave conditions. I show that due to the destructive interaction of aortic waves, the pulsatile LV workload can still be abnormally high when *pp* seems normal. Therefore, in hypertensive patients, a systems approach with full analysis of wave dynamics in the aorta is essential for the prevention and management of left ventricular hypertrophy (LVH), heart failure (HF), and sudden cardiac death (SCD).

The concept of optimum heart rate for minimization of left ventricular workload is introduced in Chapter 4. It is shown in this chapter that there is an optimum condition for aortic waves that minimizes the pulsatile workload on the heart. The results of this chapter suggest that controlling and modifying aortic wave dynamics—as the determinant of LV pulsatile load—can be a therapeutic approach for the reversal or prevention of HF.

In Chapter 5, I use an in-vitro experimental approach to validate the finding of our computational study in Chapter 4. A simple bio-inspired device that works based on the principles of wave dynamics is also introduced in Chapter 5. This device is minimally invasive and can potentially be used to reduce the LV workload in heart failure patients.

In Chapter 6, I introduce a non-dimensional number (wave condition number) that can predict the optimum wave state in a mammalian cardiovascular system. I show this number is universal among all mammals, independent of animal size, maintaining a value of 0.1. Using an *in-vitro* model of a human aorta, I show that the optimum value of the wave condition number is 0.1 for a wide range of aortic rigidities. Therefore, this non-dimensional number can be useful as a diagnostic tool in the development of new therapeutic strategies. The results of this chapter also suggest that aortic wave optimization is one of the design characteristics of the mammalian cardiovascular system.

The results of Chapter 7 demonstrate that wave reflection in the aorta creates a pumping effect similar to an impedance pump. The pumping effect can generate net flow in both forward and backward directions depending on the state of the wave dynamics. The aorta facilitates the circulation of the blood when it pumps forward. When the aorta is pumping backward, the heart needs to generate more power to overcome the extra load created by the aorta.

In Chapter 8, the concept of *Intrinsic Frequency* as a systems parameter is developed. It is shown that by using such a parameter we gain a deeper level of understanding of cardiovascular physiology. I show that intrinsic frequencies can be used as medical indices. These indices enable physicians to diagnose various cardiovascular diseases and to detect the optimum ventricular-arterial coupling. Using only the pressure waveform, the intrinsic frequency concept can be used to quantify the impaired balance between the heart and aorta under various disease conditions. One important advantage of this method is that only the shape of the pressure waveform, not the magnitude, is required.

In Chapter 9, a new medical hypothesis for sudden cardiac death (SCD) in young athletes is proposed. The hypothesis states that abnormalities in aortic wave dynamics and coronary wave dynamics may be responsible for SCD in these athletes. These abnormal waves—pathological waves—can act as a trigger toward cardiac death in the presence of cardiovascular diseases. These waves may initiate SCD in the absence of apparent cardiovascular abnormalities.

Chapter 2

A PHYSIOLOGICALLY RELEVANT, SIMPLE OUTFLOW BOUNDARY MODEL FOR TRUNCATED VASCULATURE

This chapter is based on the following published manuscript: N. M. Pahlevan, F. Amlani, H. Gorji, F. Hussain, and M. Gharib. A Physiologically Relevant, Simple Outflow Boundary Model for Truncated Vasculature. *Annals of Biomedical Engineering* 39(5): 1470-1481

2.1 Chapter Abstract

A realistic outflow boundary condition model for pulsatile flow in a compliant vessel is studied by taking into account physiological effects: compliance, resistance, and wave reflection of the downstream vasculature. The new model extends the computational domain with an elastic tube terminated in a rigid contraction. The contraction ratio, the length, and elasticity of the terminal tube can be adjusted to represent effects of the truncated vasculature. Using the wave intensity analysis method, I apply the model to the test cases of a straight vessel and the aorta and find good agreement with the physiological characteristics of blood flow and pressure. The model is suitable for cardiac transient (non-periodic) events and easily employed using so-called black box software.

2.2 Introduction

Computational modeling of blood flow is an important tool for better understanding of the underlying mechanisms of cardiovascular diseases such as atherosclerosis, aneurysms, heart attack, congestive heart failure, and aortic valve disorder. It is also an essential tool in the design and performance evaluation of cardiovascular devices such as left ventricular assist devices (LVAD), artificial heart valves, stents, and grafts.

The heart generates pulsatile flow that enters the compliant aorta and propagates as flow and pressure waves, which reflect due to the tapering of vessels, bifurcations, and variations in arterial wall properties. The intensity and pulsatility of pressure waves, often accompanied by dilations of local vessels, decrease as the waves enter smaller vessels and eventually disappear into the capillary bed. The history of blood flow simulation dates back to the 1960's [21-23], and significant progress has been made from patient-specific image-based modeling to fluid-solid interaction modeling. Realistic outflow boundary conditions are critical in acquiring physiologically relevant solutions for pressure and flow waves. The most commonly used outflow conditions have been (i) constant pressure, (ii) pure resistance, (iii) three element Windkessel, and (iv) structure tree (impedance) boundary models.

2.2.1 Constant Pressure

This outflow condition assumes that the pressure at the outflow boundary is constant. It does not give accurate results for the pressure wave, and it is difficult to account for the pressure phase shift when multiple branches are present[24, 25]. This condition is mostly valid only at the end of a capillary bed where the venules begin.

2.2.2 Pure Resistance

This outflow condition relates the pressure (p) to the flow (q) by a constant resistance (R),

$$p = qR \tag{2.1}$$

Forcing the flow and pressure waves to be in phase, results in a non-physiological solution. This model also eliminates the compliant effect of the truncated vascular network. Thus, this condition is mostly valid only at the level of the arterioles and the capillaries [24, 26, 27].

2.2.3 Three Element Windkessel (RCR model)

This is a lumped model that includes both the compliant and resistive effects of the truncated vascular network. The flow and pressure are related through a linear ordinary differential equation

(ODE),

$$\frac{dp}{dt} = R_1 \frac{dq}{dt} + \frac{1}{R_2 C}\big((R_1 + R_2)q - p\big). \tag{2.2}$$

The constants R_1, R_2, and C depend on the specified level of truncation, as detailed by Stergiopulos[28]. Although this model admits a phase shift between the pressure and the flow, the shift is not significant compared to physiological values [29]. Furthermore, the Windkessel family models (RC, RCR, transient RCR, etc.) do not capture the wave reflections. However, the RCR model has been recently modified for non-periodic phenomena in the cardiac cycle[25].

2.2.4 Structured Tree (Impedance Boundary Condition)

This boundary condition was developed by Olufsen[30] in 1999 for linearized one-dimensional (viscous) Navier-Stokes equations and was later modified by Vignon-Clementel *et al* [31] as the *impedance boundary condition* for three-dimensional finite element models of blood flow. Defining the impedance $\hat{Z}(x,\omega)$ as the ratio of $\hat{p}(x,\omega)$ to $\hat{q}(x,\omega)$, which are pressure p and the flow q in the frequency domain respectively;

$$\hat{p}(x,\omega) = \hat{Z}(x,\omega)\hat{q}(x,\omega). \tag{2.3}$$

The impedance boundary condition relates pressure and flow in the time domain as an integral equation (a convolution),

$$p(x,t) = \frac{1}{T}\int_{-T/2}^{T/2} Z(x,t-\xi)q(x,\xi)d\xi\ , \tag{2.4}$$

where $Z(x,t)$ is the inverse Fourier transform of $\hat{Z}(x,\omega)$. This boundary condition maintains the phase shift between pressure and flow and contains the wave propagation effects of the truncated vascular bed [30]. However; the periodicity assumption is not applicable for the simulation of non-periodic phenomena like missing heart beats or external traumatic intervention [25]. This boundary condition also assumes the same wave arrival times for all heart rates (HR)—a major drawback when the effects of HR on hemodynamics is of interest.

Boundary conditions must account for the three important effects generated by vascular networks on their upstream vessels: compliance, resistance, and wave reflection (whose arrival times are clinically important)[6, 29, 32-37]. I present here a new outflow boundary model for two- and three-dimensional fluid-solid interaction (FSI) simulation of blood flow in compliant vessels. This model can be easily implemented and has none of the drawbacks of the four methods described above. In lieu of an integral or differential representation, the new outflow model extends the computational domain to represent the compliance, resistance, and wave dynamics of the truncated vascular network. This new model can be used for transient and non-periodic events, and can also be conveniently implemented by so called black box (commercial) finite element or CFD software packages. The extended domain includes a straight elastic tube connected to a rigid tube that has a reduced diameter midway down its length (henceforth called a *rigid contraction tube*.) Three main parameters—length, Young's modulus of the elastic tube, and contraction ratio of the rigid tube—are selected so that the boundary domain best represents the truncated vascular network's resistance and compliance, as well as the arrival time of the reflected waves.

2.3 Methods

The truncated vascular network has the important feature of adding compliance, resistance and reflected waves to the upstream vessel. Our outflow boundary model accounts for these additional features by using a straight elastic tube connected to a rigid contraction tube. This extends the domain at a low computational cost relative to that of the anatomically constructed vessel model. The parameters of the elastic tube (Young's modulus, wall thickness and length) as well as the rigid contraction tube (the contraction ratio) are selected to match the desired volume compliance, resistance and wave reflections of the truncated networks. A summary of the procedure is shown in the flowchart of Figure 2.1.

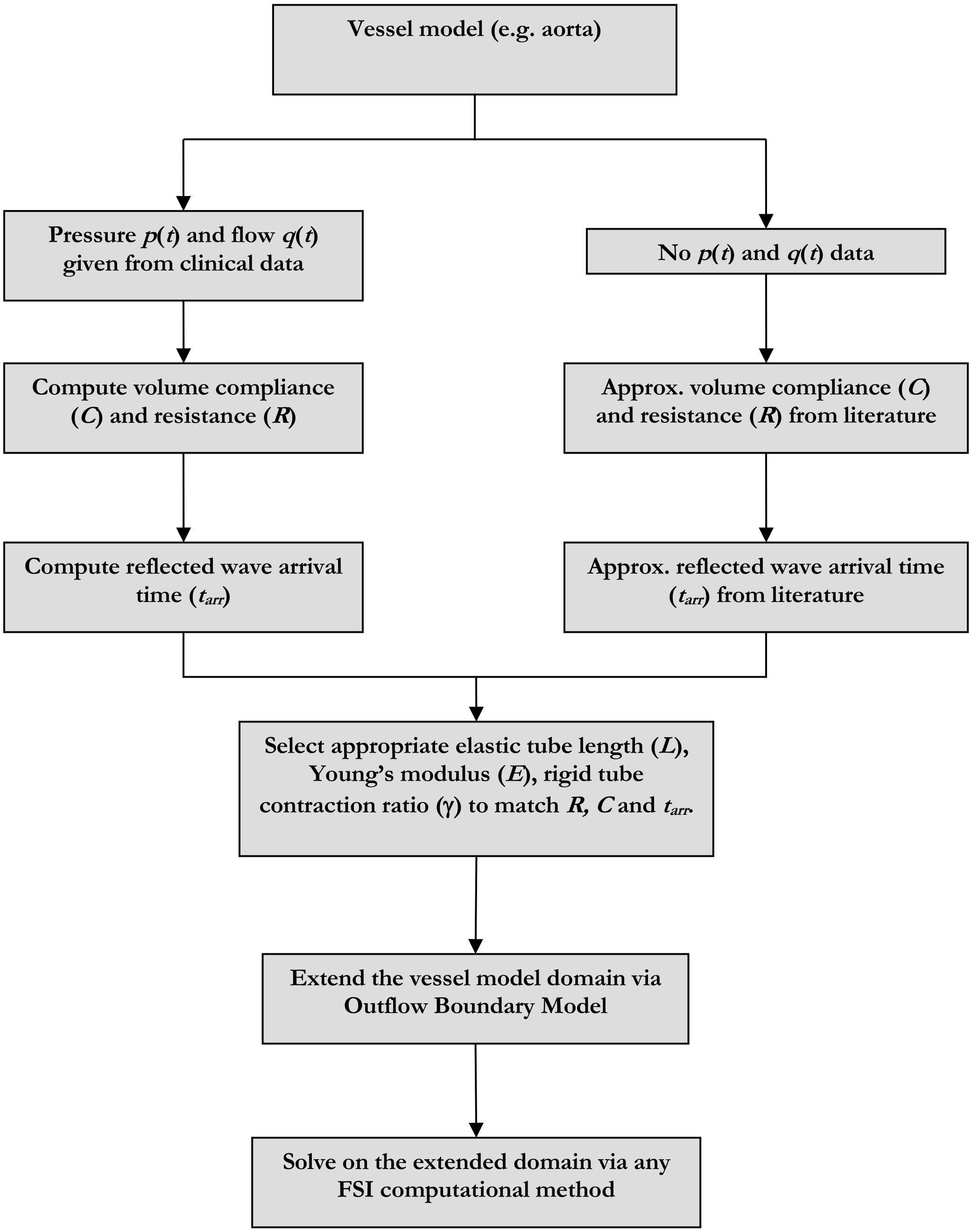

Figure 2.1: Summary of the procedures for using the outflow boundary model

2.3.1 Computing Volume Compliance and Resistance

Approximate physiological values of the total and terminal volume compliances and resistances have been calculated for the main arterial vessels[23, 28, 38]. However, more precise values are necessary for patient specific studies. Stergiopulos *et al*[39] evaluated the accuracy and applicability of all proposed compliance estimation methods. They have shown that two-area and pulse pressure methods—both based on the two element Windkessel model—are more accurate than others. These methods can be applied to all locations in the arterial network[40], but they require data of both pressure *p(t)* and flow *q(t).*

2.3.1.1 Two Area Method (Self *et al*[38])

The cardiac cycle is divided into two parts. The first begins with the onset of systole (t_0) and ends with the peak of the systole (t_1), and the second part begins with the peak of the systole and ends with the termination of the cycle (t_2). Knowing the flow *q(t)* and the pressure *p(t)* for the whole cycle, one can solve for resistance *R* and compliance *C* of the truncated vascular tree by the system[38]

$$\begin{cases} \displaystyle\int_{t_0}^{t_1} q(t)dt = C\big(p(t_1) - p(t_0)\big) + \frac{1}{R}\int_{t_0}^{t_1} p(t)dt \\ \displaystyle\int_{t_1}^{t_2} q(t)dt = C\big(p(t_2) - p(t_1)\big) + \frac{1}{R}\int_{t_1}^{t_2} p(t)dt. \end{cases} \tag{2.5}$$

2.3.1.2 Pulse pressure method[39]

Given the pressure and flow at certain points in the arterial network, *R* is calculated by dividing the mean value of the pressure by the mean value of the flow. Then fitting the two-element Windkessel model,

$$C\frac{dp}{dt}+\frac{p}{R}=q\ , \tag{2.6}$$

to the measured pulse pressure and flow rate gives the required compliance C.

2.3.2 Reflected wave arrival time and analysis of wave dynamics

In order to determine the wave arrival time required for the boundary model, it is imperative that I first introduce the wave intensity (WI) analysis method developed by Parker *et al* [41], a method that I will also employ to analyze the wave dynamics in the time domain of our computational results.

2.3.2.1 Wave Intensity (WI) Analysis

The method is based on the well-known method of characteristics and follows the propagation of infinitesimal waves. The one-dimensional equations of the motion, where z is the direction along the axis of the vessel,

$$\frac{\partial A}{\partial t}+\frac{\partial (UA)}{\partial z}=-q_l \tag{2.7}$$

$$\frac{\partial U}{\partial t}+U\frac{\partial U}{\partial z}=-\frac{1}{\rho}\frac{\partial p}{\partial z}+F_R\ , \tag{2.8}$$

result from integrating the momentum and continuity equations of an incompressible fluid inside a vessel [42]; q_l is a volumetric outflow rate per unit length of the vessel (leakage); F_R is the vector sum of all forces excluding pressure per unit mass; U is average velocity over the cross section; p is pressure; t is time; and ρ is density. If we assume area is a function of the local instantaneous pressure, $A=A(p(z,t);t)$, then Equations 2.7 and 2.8 can be written in matrix form as

$$\frac{\partial}{\partial t}\begin{bmatrix} p \\ U \end{bmatrix} + \begin{bmatrix} U & \rho c^2 \\ \frac{1}{\rho} & U \end{bmatrix} \frac{\partial}{\partial z}\begin{bmatrix} p \\ U \end{bmatrix} = \begin{bmatrix} -\rho c^2 q_l / A \\ F_R \end{bmatrix}, \tag{2.9}$$

where $c = \sqrt{\frac{A}{\rho \partial A / \partial p}}$ is the speed of propagation [42]. The coefficient matrix of the displacement derivative has eigenvalues $\lambda = U \pm c$ and hence the characteristics lines are $\frac{dz}{dt} = U \pm c$. The positive sign corresponds to the forward propagating wave and the negative sign, the backward wave [41].

Along the characteristics, we can write the time derivative as

$$\frac{d}{dt} = \frac{\partial}{\partial t} + \frac{dz}{dt}\frac{\partial}{\partial z} = \frac{\partial}{\partial t} + (U \pm c)\frac{\partial}{\partial z} \tag{2.10}$$

and apply it to Equation 2.9, transforming the partial differential equation into a system of two ODE's along each characteristics:

$$\frac{dU}{dt} + \frac{1}{\rho c}\frac{dp}{dt} = F_R - \frac{c q_l}{A} \quad on \quad \frac{dz}{dt} = U + c \tag{2.11}$$

$$\frac{dU}{dt} - \frac{1}{\rho c}\frac{dp}{dt} = F_R + \frac{c q_l}{A} \quad on \quad \frac{dz}{dt} = U - c \tag{2.12}$$

Assuming an impermeable wall ($q_l = 0$) as well as assuming that the location of interest is away from branches and other arterial discontinuities, it is reasonable to assume F_R is equal to zero locally [41]. Under these assumptions, the Riemann function is constant, so the Riemann invariants in terms of P and U can be written as[41]

$$dR_{\pm} = dU \pm \frac{1}{\rho c} dp\,. \tag{2.13}$$

Solving for *dp* and *dU*, their product

$$dI = dp dU = \frac{\rho c}{4}\left(dR_{+}^{2} - dR_{-}^{2}\right) \tag{2.14}$$

is defined as the wave intensity in units of power per unit area (e.g. W/m^2)[41, 43]. It is clear from Equation 2.14 that the contribution to the intensity of any forward wave (e.g. compression or decompression) is positive, and the contribution from a backward wave is negative. Therefore, if $dI > 0$, the forward waves dominate, and if $dI < 0$ the backwards (reflected) waves dominate, allowing one to easily determine wave propagation at each time. Because there is no assumption of linearity and periodicity, this method has a clear advantage over the often-used frequency (impedance) analysis, which requires those assumptions. Furthermore, the analysis being in time rather than frequency, every point on the dI graph directly corresponds to a specific point of the cardiac cycle.

If we also assume the incremental waves are additive, we can decompose the wave intensity into purely forward (+) and purely reflected (-) waves as [44, 45]

$$dI_+ = \frac{1}{4\rho c}(dp + \rho c dU)^2 \tag{2.15}$$

$$dI_- = \frac{-1}{4\rho c}(dp - \rho c dU)^2 \,. \tag{2.16}$$

2.3.2.2 Determining Wave Arrival Time (t_{arr})

Given data of pressure *p(t)* and flow *q(t)*, one can perform a WI analysis by the procedure outlined above. This analysis enables one to decompose the wave intensity into forward and reflected waves in the time domain. As will be demonstrated in the wave intensity tests in the results section of this paper, one can then easily determine when the reflected waves arrive from the WI graphs.

2.3.3 Selecting Boundary Model Parameters

The properties of the elastic tube and rigid contraction tube of the boundary model are selected to match the *C*, *R* and t_{arr} determined above. These properties—the Young's modulus (*E*) and length

(L) of the elastic tube, and the contraction ratio (γ) of the rigid tube—can be derived as functions of the determined C, R and t_{arr}.

2.3.3.1 Elastic Tube

Using a thin wall assumption, the wall stress can be written as [46]

$$\sigma = \frac{r\Delta p}{h}\,, \tag{2.17}$$

where σ is the wall stress, r is the tube radius, p is the pressure, and h is the tube thickness. For a linear elastic material, stress relates to strain (ε) and Young's modulus (E) as $\sigma = E\varepsilon$.

From Equation 2.17, $\frac{\Delta r}{\Delta p} = \frac{r^2}{Eh}$, where $\varepsilon = \Delta r/r$. In the limiting case, as $\Delta r, \Delta p \to 0$, we have

$$\frac{\Delta r}{\Delta p} = \frac{r^2}{Eh} \to \frac{dr}{dp} = \frac{r^2}{Eh}\,. \tag{2.18}$$

Substituting Equation 2.18 into the volume compliance $C = \frac{dV}{dp} = \left(\frac{dV}{dr}\right)\left(\frac{dr}{dp}\right)$ yields $C = \left(\frac{dV}{dr}\right)\left(\frac{r^2}{Eh}\right)$, which gives an approximate volume compliance formula for a cylindrical tube of length L and radius r as

$$C \approx 2\pi\frac{r^3 L}{Eh}\,. \tag{2.19}$$

To find a second relationship so that E, L can be uniquely determined, we note that the reflected wave arrival time is given by the time it takes for a wave to travel to the end of the elastic tube (the onset of the rigid tube, i.e. the reflection site), and travel back. That is,

$$t_{arr} = \frac{2L}{c}\,, \tag{2.20}$$

where the wave speed (c) can be approximated by [7]

$$c = \sqrt{\frac{Eh}{2\rho_f r(1-\nu^2)}} \,. \tag{2.21}$$

Solving Equations 2.20 and 2.21 for *E*, *L* gives

$$E = E(C, t_{arr}) = \left(\frac{\pi r^3 t_{arr}}{C\sqrt{2\rho_f rh(1-\nu^2)}}\right)^2 , \tag{2.22}$$

$$L = L(C, t_{arr}) = \frac{\pi r^2 t_{arr}^2}{4C\rho_f(1-\nu^2)} , \tag{2.23}$$

where *r*, *h* are the radius and wall thickness (respectively) of the elastic tube of the boundary model and must necessarily be the same as the vessel model for the geometry to be continuous.

2.3.3.2 Rigid Contraction Tube

Having the rigid contraction tube in the boundary domain provides the required resistance or pressure drop. Although blood flow is pulsatile, the resistance is related to the mean or steady part of the pressure and flow. Thus the steady formula can be used by setting the contraction ratio $= D_2/D_1$, where D_2 is the diameter of the narrower (small) part of the rigid tube and D_1 is the diameter of the wider part of the rigid tube. This gives the pressure drop for steady flow in the contraction tube as [47]

$$\frac{\Delta p}{{}^1\!/_2\,\rho V_2^2} = \left(1 - \left(\frac{D_2}{D_1}\right)^4\right) + \frac{8\dot{E}_\nu}{\rho\pi V_2^2 D_2^2} , \tag{2.24}$$

where $\dot{E}_\nu$ is the viscous energy loss, ρ is the density of the fluid, and V_2 is the average velocity over the cross section of the small tube (after contraction). By considering the fact that $A_1V_1 = A_1V_1 = \bar{Q}$, where *A* is the cross sectional area, Equation 2.24 can be rearranged as

$$\Delta p = k_1\gamma^{-4} + k_2 , \tag{2.25}$$

where $k_1 = 8\rho\bar{Q}^2/\pi^2 D_1^4$ and $k_2 = 8\dot{E}_v/\rho D_2^2 - 8\rho\bar{Q}^2/\pi^2 D_1^4$. Thus the pressure drop is of the order γ^{-4}. Noting that $\Delta p = R\bar{Q}$ [7], the contraction ratio then becomes a function of our required resistance *R* as

$$\gamma = \gamma(R) = \left(\frac{R\bar{Q} - k_2}{k_1}\right)^{\frac{-1}{4}} . \tag{2.26}$$

2.3.4 Computational Method

2.3.4.1 Mathematical Model

In the solid domain, where it is assumed the walls are composed of elastic isotropic material, a standard Lagrangian formulation for large deformations / small strain was used [48]. The dynamic motion of the wall is calculated by the Lagrangian form of the balance of momentum equations (Equation 2.27). To describe the elastic material for large deformation analysis, linear elastic relations generalized to the Total Lagrangian (TL) formulation were used (Equation 2.28)[48-50]. That is,

$$\sigma_{ij,j} + F_i = \rho_s \ddot{u}_i \, , \tag{2.27}$$

$$\sigma_{ij} = C_{ijrs}\varepsilon_{rs} \, , \tag{2.28}$$

where σ_{ij} is the second Piola-Kirchhoff stress tensor, F_i is the external force, u is the displacement vector, ρ_s is the wall density, ε_{rs} is the Green-Lagrange strain tensor, $C_{ijrs} = \lambda\delta_{ij}\delta_{rs} + \mu_l(\delta_{ir}\delta_{js} + \delta_{is}\delta_{jr})$ are the components of the constant elasticity tensor, δ_{ij} is the Kronecker delta, and λ, μ_l are Lamé constants.

Note that the second Piola-Kirchhoff and Green-Lagrange strain tensors do not change under rigid body motion. Therefore, as long as the straining is small, Equation 2.28 is completely equivalent to Hooke's law for infinitesimal displacement conditions [48].

For the fluid domain, the full incompressible Navier-Stokes (N-S) equations were used. In Eulerian form, they are

$$\vec{\nabla}.\vec{V} = 0\,, \tag{2.29}$$

$$\rho_f \left(\frac{\partial \vec{V}}{\partial t} + \vec{V}.\vec{\nabla}\vec{V} \right) + \vec{\nabla} p = \mu_f \nabla^2 \vec{V} + \vec{F}_b\,, \tag{2.30}$$

where $\vec{V} = (v_y, v_z)$ represents the flow velocity vector, ρ_f is the fluid density, p is the static pressure, μ_f is the dynamic viscosity of the fluid, and $\vec{F}_b$ is the body force.

Since our fluid domain has moving boundaries, an arbitrary Lagrangian-Eulerian (ALE) formulation is used for the analysis of the fluid flow [50-53]. This formulation can be directly coupled with the Lagrangian formulation of the solid domain. In an ALE formulation, the material derivative for all the solution variables is given by [54]

$$\frac{D(.)}{Dt} = \frac{\partial(.)}{\partial t} + (\vec{V} - \vec{W}).\vec{\nabla}(.), \tag{2.31}$$

where $\partial(.)/\partial t$ is the transient term at the considered mesh position, $\vec{W}$ is the corresponding mesh velocity, and $\vec{V}$ is the actual fluid particle velocity. In view of Equation 2.31, Equation 2.30 becomes

$$\rho_f \left(\frac{\partial \vec{V}}{\partial t} + (\vec{V} - \vec{W}).\vec{\nabla}\vec{V} \right) + \vec{\nabla} p = \mu_f \nabla^2 \vec{V} + \vec{F}_b. \tag{2.32}$$

Assuming no-slip boundary conditions at the wall, the coupling conditions at the fluid-solid interface are

$$Velocity: \vec{V_f} = \vec{u}_s\ , \tag{2.33}$$

$$Traction: \vec{n}.\underline{\underline{\sigma_f}} = \vec{n}.\underline{\underline{\sigma_s}} \tag{2.34}$$

where $\vec{V_f}$ and $\vec{u}_s$ are the velocities of the fluid and the solid at the interface, respectively, and $\underline{\underline{\sigma_f}}$ is the fluid stress tensor, $\underline{\underline{\sigma_s}}$ the solid stress tensor.

2.3.4.2 Finite Element Solution

To solve the equations of solids and fluids numerically, a Finite Element method was applied on the boundary condition model attached first to a straight vessel model and, second, to a three-dimensional axisymmetric model of the aorta.

At each time step, a direct coupling fluid structure interaction (FSI) method is used to solve the solid, fluid and interface equations simultaneously. After discretization of the equations of the fluid and solid, the algebraic system has the form[55, 56] :

$$\mathbf{F}(\mathbf{X}) = \begin{bmatrix} \mathbf{F}_f(\mathbf{X}_f, \mathbf{X}_s) \\ \mathbf{F}_s(\mathbf{X}_f, \mathbf{X}_s) \end{bmatrix} = \mathbf{0}\ , \tag{2.35}$$

where $\mathbf{X}_f$, $\mathbf{X}_s$ are the fluid and solid nodal solution variables, respectively, and $\mathbf{F}_f$, $\mathbf{F}_s$ are the finite element equations of the fluid and solid models, respectively [55].

In the direct coupling method, the equations become linearized as (by using, for example, the Newton-Raphson method at iteration k)[50]

$$\begin{bmatrix} \mathbf{A}_{ff} & \mathbf{A}_{fs} \\ \mathbf{A}_{sf} & \mathbf{A}_{ss} \end{bmatrix} \begin{bmatrix} \mathbf{X}_f^{k+1} - \mathbf{X}_f^k \\ \mathbf{X}_s^{k+1} - \mathbf{X}_s^k \end{bmatrix} = \begin{bmatrix} -\mathbf{F}_f^k(\mathbf{X}_f, \mathbf{X}_s) \\ -\mathbf{F}_s^k(\mathbf{X}_f, \mathbf{X}_s) \end{bmatrix}, \tag{2.36}$$

where $\mathbf{A}_{ff}$ and $\mathbf{A}_{ss}$ are the fluid Jacobian matrix and the solid Jacobian matrix, respectively, and $\mathbf{A}_{fs}$ and $\mathbf{A}_{sf}$ are the coupling Jacobian matrices. These Jacobian matrices are calculated as [55]

$$\begin{aligned} \mathbf{A}_{ff} &= \frac{\partial \mathbf{F}_f^k}{\partial \mathbf{X}_f^k}, \qquad & \mathbf{A}_{fs} &= \frac{\partial \mathbf{F}_f^k}{\partial \mathbf{X}_s^k}, \\ \mathbf{A}_{sf} &= \frac{\partial \mathbf{F}_s^k}{\partial \mathbf{X}_f^k}, \qquad & \mathbf{A}_{ss} &= \frac{\partial \mathbf{F}_s^k}{\partial \mathbf{X}_s^k}. \end{aligned} \tag{2.37}$$

This linearized system is solved at each (e.g. Newton) iteration k and the subsequent solutions for the solid and fluid are updated. Residuals (stress or displacement) are then computed and compared against specified tolerances. If the solutions have not yet converged, the procedure iterates to $k+1$ and repeats the above linearization procedure. Once the solutions have converged, the method proceeds to the next time step. In summary, the general computational steps in the employed direct coupling method were (1) to assemble the solid and fluid equations separately into a single fluid and single solid model; (2) to assemble the solid matrix, fluid matrix, and the coupling matrices into one coupled matrix system; (3) to solve the linearized equation of the coupled system and to update the solution; and (4) to compute and check the residuals against the specified tolerance. If the solution did not converge, the process was restarted from step (1) [50, 55, 56].

Three-dimensional axisymmetric elements were used for each domain in space, and an implicit Euler method was used for the integration in time. The final discretized equations were solved using the commercial software package, ADINA (ADINA R&D Inc.)[49, 50].

2.4 Results

2.4.1 Straight Vessel

I first studied the boundary model applied to a straight vessel with uniform thickness and a circular cross section. The length, thickness and internal radius of the straight vessel were $L_v=20\ cm$, $h=0.1\ cm$, and $r_{in}= 1\ cm$ respectively. The vessel was connected to various cases of the outflow boundary model. The inflow boundary condition assumed to have flat velocity profile varying as a half-sine flow wave with a period of $T=0.8\ sec$ and a duty cycle of $dc = {}^{1}/_{3}$ (i.e. the inflow is equal to zero for 2/3rd of the cycle),

$$v_z(t) = \begin{cases} 60\ \sin\left(\frac{3\pi t}{T}\right) & t \leq \frac{T}{3} \\ 0 & t > \frac{T}{3} \end{cases} \quad \left(\frac{cm}{s}\right) \tag{2.38}$$

where $v_z(t)$ is the velocity, t is time, and T is the period of pulsation.

A zero traction boundary condition for the outer surface of the solid was used. In the fluid domain, a constant normal traction, called the end pressure $P_{end} = 10.5\ mmHg$ was applied to the end of the rigid boundary tube. The Young's modulus of the straight vessel was $E=10^6\ dyne/cm^2$. The Poisson's ratios and the densities of both the straight vessel and elastic boundary tube were set to be $\upsilon=0.45$ and $\rho_s=1$ gr/cm^3, respectively. For the fluid, viscosity was $\mu=0.051$ *Poise*, and density was $\rho_f=1.05\ gr/cm^3$. All material values were within physiological ranges [7]. The numerical models of both the solid and fluid components were meshed with 4-noded axisymmetric elements. All simulations started at rest with no loading condition, and the simulations were carried out to 18 cycles to ensure that the mean pressure reached a steady state.

2.4.1.1 Wave Intensity Analysis Test (Straight Vessel with Only Rigid Boundary Tube)

WI analysis was applied to a case with a known solution. A straight vessel was connected to only a rigid boundary tube (Figure 2.2). Point "B" is the end-point of the straight vessel and the beginning point of the rigid boundary tube. Since the fluid is incompressible, we expect no wave reflection in the rigid tube, i.e. beyond point B. All incoming waves should reflect at B and travel back towards point A, where they are reflected a second time as second generation waves. This cycle of reflections between A and B continues until the waves fully decay, with third and fourth generation waves, and so on. The time difference *Δt* between two consecutive wave generations is

$$\Delta t = \frac{2L_v}{c}, \tag{2.39}$$

where *c* can be approximated by Equation 2.21. From our previously defined parameters of ρ_f, r_{in}, *E*, *h*, ν, and L_v, Equation 2.39 predicts that for the approximate time difference between two wave generations $\Delta t \approx 0.16\ sec$.

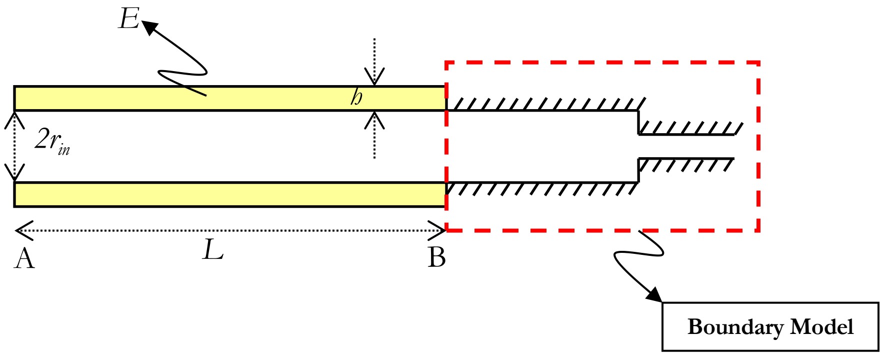

Figure 2.2: Straight vessel terminated by a rigid contraction tube.

Figure 2.3c shows the total wave intensity, *I(t)*, computed by using Equation 2.14 applied to the *p(t)* (Figure 2.3a) and *U(t)* (Figure 2.3b) obtained from numerical solutions at point B for one complete cycle. As expected, *I(t)* was never negative during the cycle since there were no backward waves propagating beyond B. Each generation of the reflected waves can be easily distinguished with a time difference of $\Delta t \approx 0.15\ sec$, close to our predicted value.

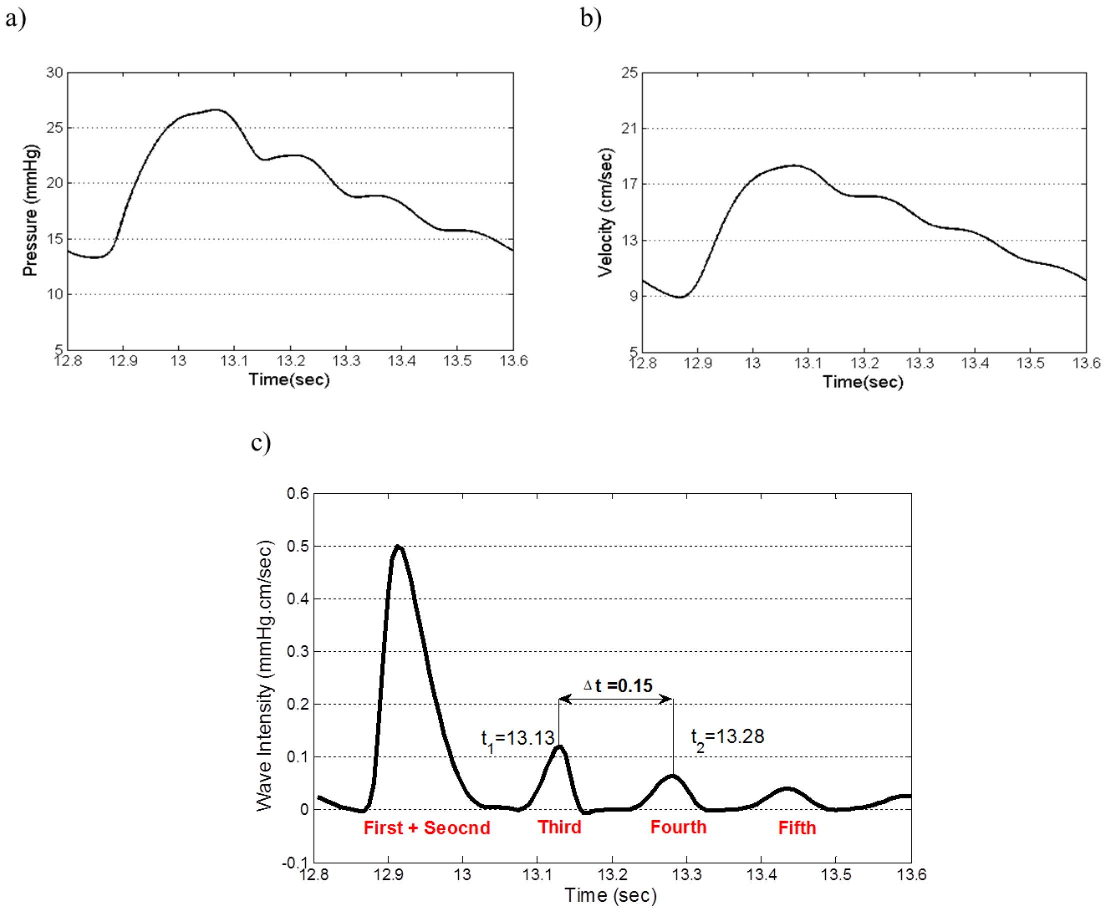

Figure 2.3: a) Pressure wave at point B of Figure 2.2. b) Velocity wave at point B. c) The corresponding wave intensity is nonnegative at all times indicating the absence of the backward waves. The first and second generations combine to create a resonance peak.

2.4.1.2 Straight Vessel with Full Outflow Boundary Model

A straight vessel connected to a full outflow boundary model was studied (with both an elastic and a rigid contraction tube) as seen in Figure 2.4. The parameters of the outflow boundary model are listed in Table 2.1.

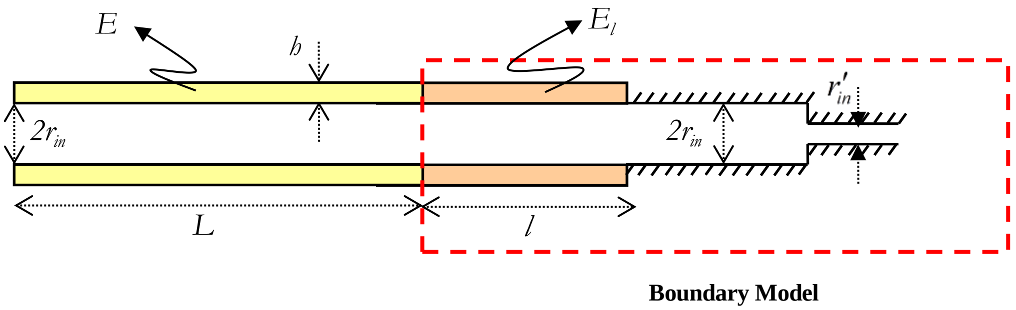

Figure 2.4: Straight vessel connected to the boundary model.

Table 2.1

Parameters of outflow boundary model for straight vessel case

Symbol	Description	Value
E_1	Young's modulus of the elastic boundary tube	$2 \times 10^6\ {dyne}/_{cm^2}$
L	Length of the elastic boundary tube	10 cm
h	Wall thickness of the elastic boundary tube	0.1 cm
γ	Contraction ratio of the rigid boundary tube	0.5
C	Volume compliance of the elastic boundary tube	$3.14 \times 10^{-4}\ {cm^5}/_{dyne}$

Note: γ is the ratio of the radii of the rigid boundary tube after contraction (r'_{in}) to that before contraction (r_{in}).

Zero normal traction was imposed on the outer surface of both the boundary and straight vessel elastic walls. In the fluid domain, a constant normal traction of $p_{end} = 10.5\ mmHg$ was imposed at the end of the boundary model. The thicknesses and inner radii of the elastic and rigid (before contraction) boundary tubes were the same as those of the straight vessel.

The results of the numerical simulation are shown in Figures 2.5a and 2.5b as pressure-velocity curves and wave intensities (forward, backward, total), respectively, at the onset of boundary. Wave speed was calculated from the left graph using the PU-loop method [44], where the slope of the pressure-velocity curve at the beginning of the cycle equaled ρc when reflected waves were absent. From the given density of ρ_f=$1.05\ gr/cm^3$, the computed slope of $0.25\ mmHg.sec/cm$ yielded a wave speed of $c = 3.18\, m/sec$. Equations 2.15 and 2.16 were used to decompose the total wave intensity into the red (forward) and blue (reflected) curves in Figure 2.5b.

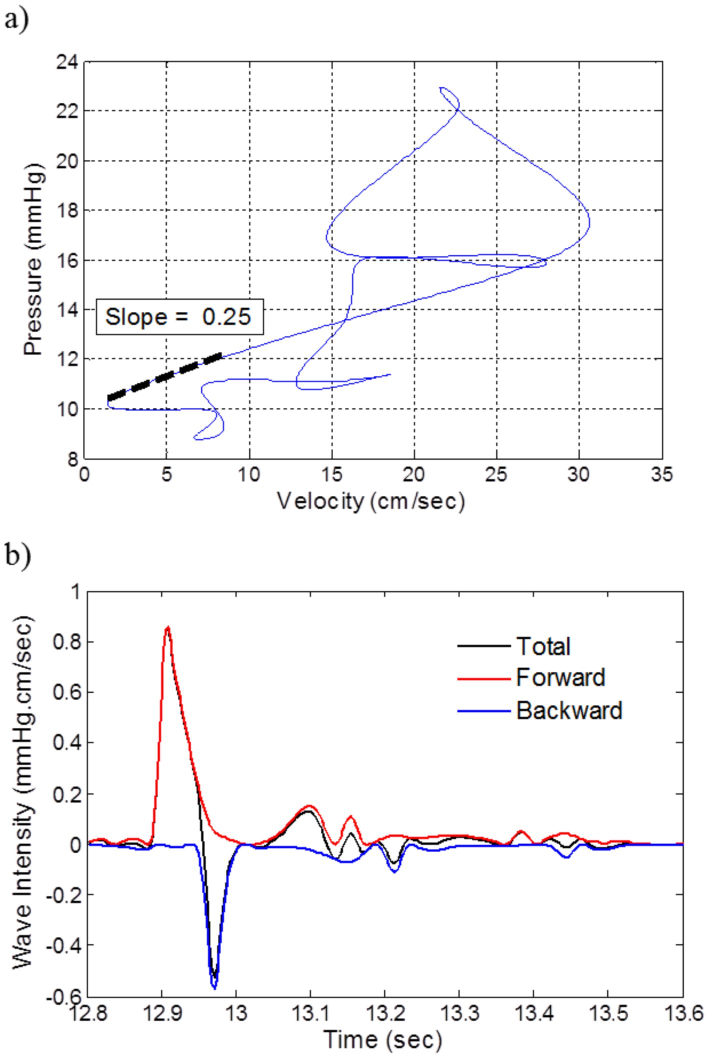

Figure 2.5: a) Pressure-velocity curves at the onset of the boundary were used to compute the local wave speeds by the PU-loop method. b) Wave intensities were calculated at the onset of the boundary, where black is the total wave intensity, red is the forward wave intensity, and blue is the backward (reflected) wave intensity.

The contraction of the rigid tube is expected to affect only the mean pressure. It should not affect the overall shape of pressure wave, nor should it affect the overall pattern of reflected wave intensity qualitatively. The arrival time of the reflected waves should not be affected by the contraction ratio. Indeed, the simulations (Figure 2.6) for three contraction ratios, *γ=0.5* (control case), *0.45*, and *0.6* confirmed this prediction. However, at high contraction ratios (low resistance), the pressure wave appeared to be slightly flatter after the systolic period, but the overall shape of the pressure wave and reflected wave intensity were not altered in Figure 2.6.

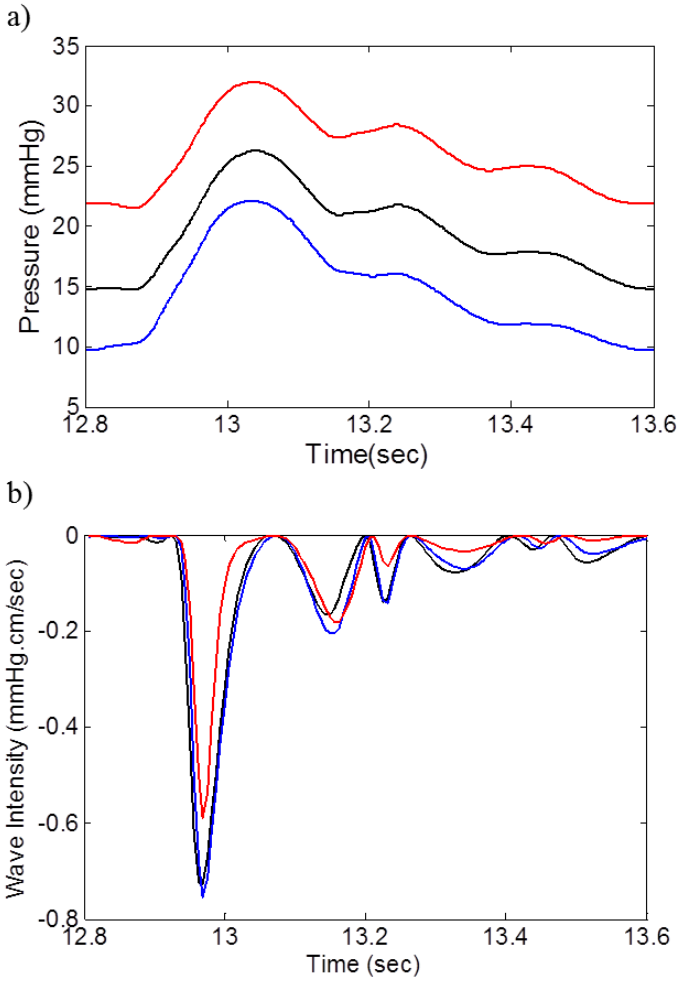

Figure 2.6: a) Pressure waves for γ=0.5 (black), 0.45 (red), and 0.6 (blue). b) Intensity and arrival times of those respective reflected waves.

2.4.2 Aortic Model

The outflow boundary model on a three-dimensional axisymmetric model of the aorta was studied in this section. The geometrical data of the aortic model, such as aortic length, inner diameter, and wall thickness, were within the average physiological range (Caro *et al* [6]). The change of stiffness along the aorta and tapering of the aorta were considered, but the aortic arc and bifurcations were excluded since the model is 3D axisymmetric. The Young's modulus of the aortic model wall was taken from a test case of a 30 year old healthy man studied in Nichols *et al* [7] and the blood was assumed to be an incompressible Newtonian fluid. The material properties of the aortic model are provided in Table 2.2, and the parameters of the outflow boundary model are provided in Table 2.3. A constant normal traction of *10.5 mmHg* was imposed at the end of boundary model, and zero normal traction was imposed on the outer surface of both the boundary and aortic model elastic walls.

Table 2.2

Parameters of aortic model

Parameter	Value	
Young modulus, Aortic sinus	3.5×10^6	dyne/cm^2
Young modulus, Ascending aorta	4.2×10^6	dyne/cm^2
Young modulus, Descending aorta	4.67×10^6	dyne/cm^2
Young modulus, Abdominal aorta	5.9×10^6	dyne/cm^2
Poisson ratio	0.45	
Vessel wall density	1.05	gr/cm^3
Blood viscosity	0.051	Poise
Blood density	1.05	gr/cm^3

The validity of the outflow boundary model was tested by specifying only the flow wave at the upstream inlet of the aortic model and checking if the resulting numerical pressure wave solution was physiologically accurate, both at the inlet and throughout the aorta. Hence, at the inlet, a physiological flow wave (Figure 2.7), from Matthys [57], with a flat velocity profile was imposed and it was scaled to give a cardiac output (CO) and heart rate (HR) of *4.6 L/min* and *120 bpm*, respectively.

Table 2.3
Parameters of outflow boundary model for aortic model

Symbol	Description	Value
r_{in}	The inner radius of the elastic boundary tube	0.631 *cm*
L	Total length of the elastic boundary tube	10.5 *cm*
h	Wall thickness of the elastic boundary tube	0.065 *cm*
γ	Contraction ratio of the rigid boundary tube	0.76
C_t	Total volume compliance of the boundary model	$9.96 \times 10^{-6}\ cm^5/_{dyne}$

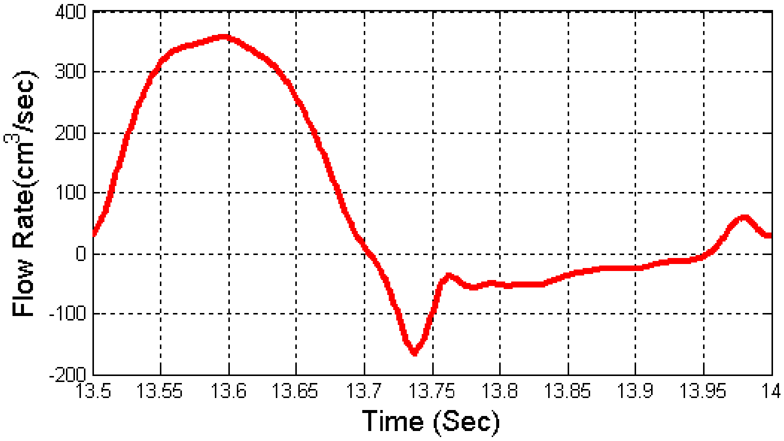

Figure 2.7: Inflow wave

A total of 17,416 three-node elements were used for the fluid domain, and a total of 2,420 nine-node elements were used in the solid domain. The simulations were run with a time step of *0.00125 sec* until the average pressure solution reached a steady state condition (Figure 2.8). The spatial element size in the radial direction ranged from *0.63mm-1.47mm*, and the element size in the axial direction ranged from *0.66mm-1mm*. Further simulations with different time steps and mesh sizes confirmed that these results were independent of spatial and temporal discretizations. For the same spatial discretization, the pressure wave solutions for time steps of *0.000625 sec* and *0.00125 sec* revealed a maximum relative error at the inlet of less than 1%. Similarly, for the same time step, doubling the number of spatial elements revealed a maximum relative error of less than 1.4%.

To confirm the physiological accuracy of the numerical pressure wave solution given only a flow wave at the inlet, four well-known characteristics of pressure waves in a human aorta were considered (as seen in the clinical results [7] of Figure 2.9 a): (i) the existence of a dicrotic notch; (ii) the increase and the (iii) narrowing of the highest pressure peak as it travels down the aorta; and (iv) the shifting of the second-highest pressure peak to the end of the cycle. Indeed, all four characteristics were clearly captured by our numerical simulations (Figure 2.9 b), indicating the value of our boundary model in acquiring physiological solutions within the aorta.

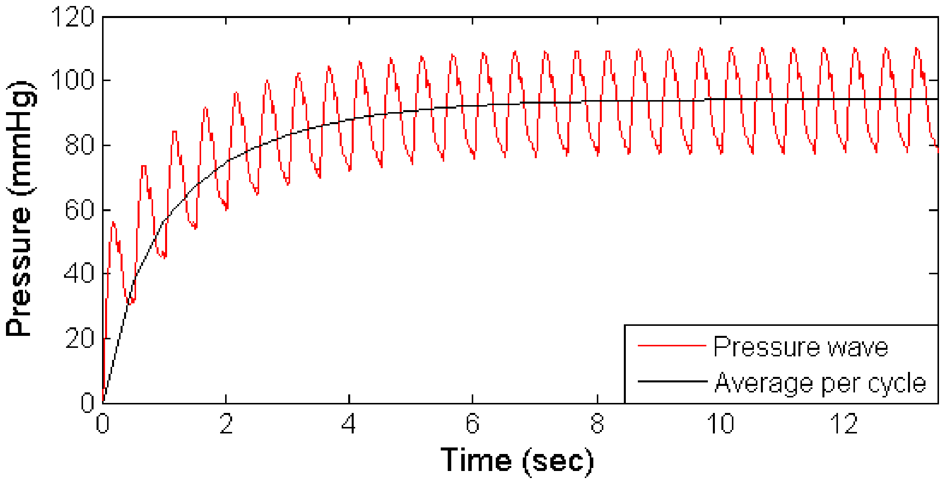

Figure 2.8: The mean pressure at the aortic input reaches a steady state for HR=120 bpm.

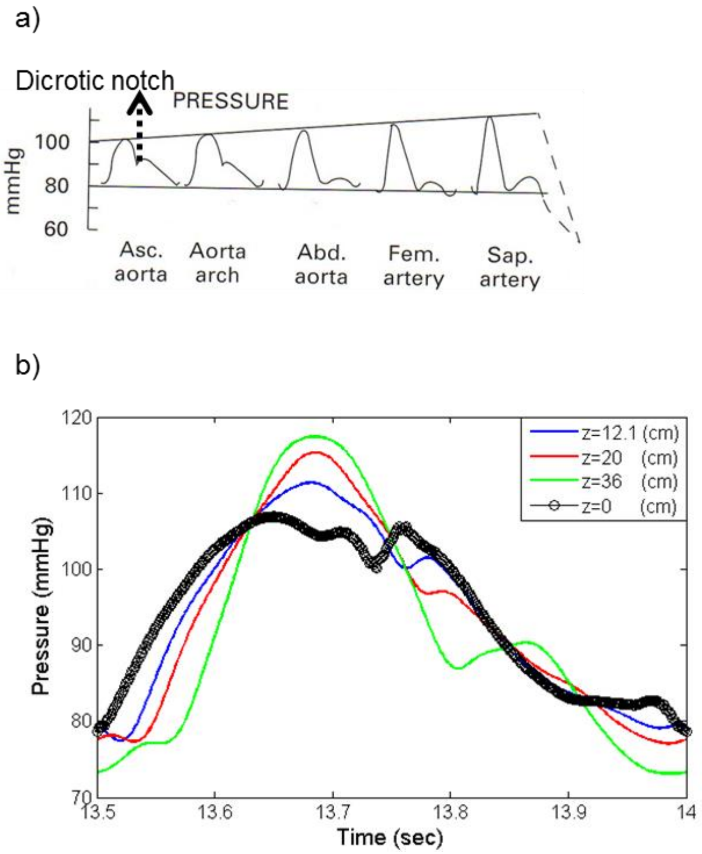

Figure 2.9: a) Pressure wave at different locations along the aorta (from Nicholes *et al* [7]) where the clinical dictoric notch can be seen. Also evident is the pressure peaking and pressure steeping phenomena as the pressure wave travels down the aorta. b) Pressure wave solution results from our aortic model, where z is the axial distance from the aortic input. The curve for z=0 corresponds to the numerical pressure wave solution at the aortic input. The curves for z=12, 20 and 38 cm (which approximately correspond to the aortic arc, the descending aorta and renal bifurcation, respectively) are all within the FSI domain. The characteristic dictoric notch in the obtained pressure wave solution is clearly evident at the aortic input. The pressure peak increase and narrowing, as well as the shifting of the second-highest peak, are also clearly evident. All results are from a 120 bpm heart rate during one cardiac cycle.

Two other important physical features of flow in the aorta can be seen in Figure 2.10 that demonstrates the decrease in average pressure per cycle, even as the peak of the pulsation increases—consistent with physical results. Additionally, our model correctly captures the expected phase shift between pressure and flow, seen in Figure 2.11, where the flow wave leads the pressure wave.

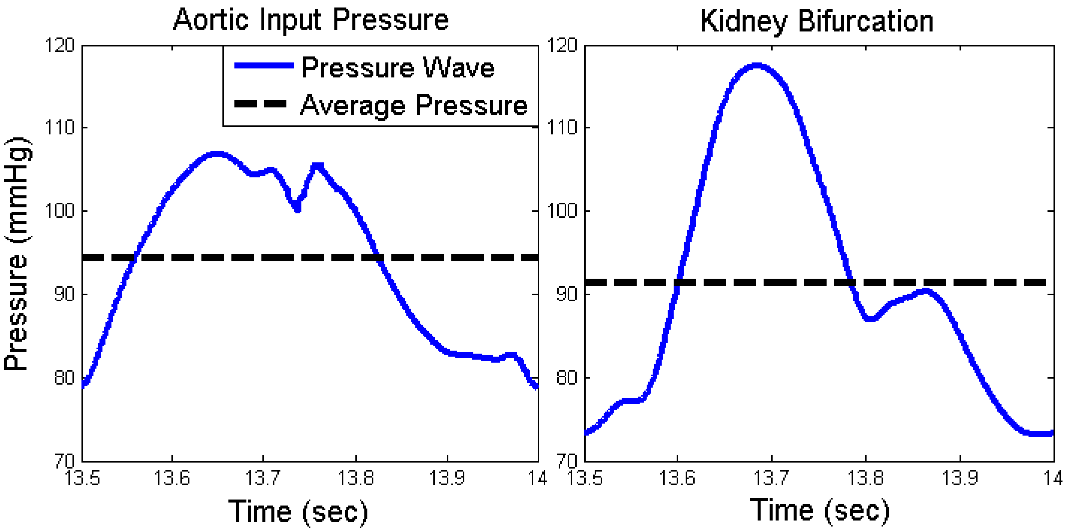

Figure 2.10: Pulsation increases while the average value per cycle decreases due to viscous losses.

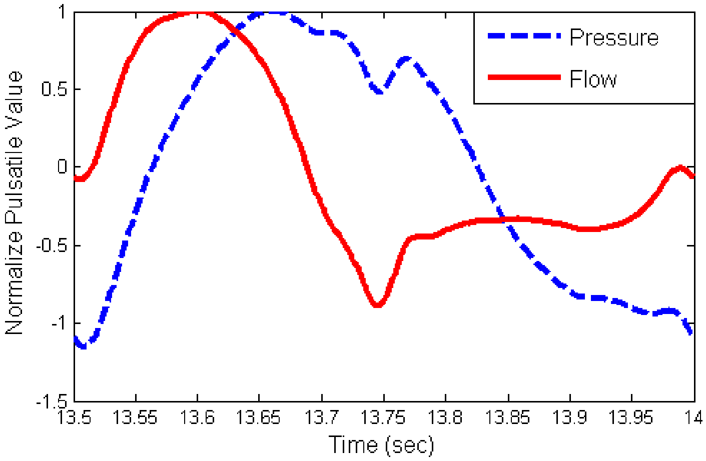

Figure 2.11: Flow wave leading the pressure wave; for better visualization, the respective normalized (dimensionless) pulsatile values of each as $\hat{p}_{pulse}$ and $\hat{q}_{pulse}$ were plotted, where $\hat{A}_{pulse} = (A - A_{mean})/Max(A - A_{mean})$.

2.5 Conclusions

A new outflow boundary model for modeling two- and three-dimensional fluid-solid interactions of blood flow in cardiovascular systems is introduced. The new technique involves extending the computational domain by an *elastic tube* connected to a *rigid contraction tube* (a contracted radius midway down its length). The user-defined geometrical and material properties of these boundary tubes allow us to retain the desired resistance, compliance and appropriate wave reflections of a truncated vascular network. This boundary condition can handle the transient (non-periodic) phenomena where the impedance boundary condition cannot [31] —events such as heartbeat skipping and external trauma.

To test the condition, I first re-introduced a common method of wave intensity (WI) analysis, decomposing the wave into both forward and backward components. I computationally tested this method by modeling a known solution of wave reflection in a straight vessel connected to only to the rigid contraction tube, achieving realistic results. I then connected the straight vessel to the outflow boundary model. The contraction ratio was specified to match the required resistance of the eliminated vasculature, and it was further shown that this ratio did not affect the shape of the wave intensity at the onset of the outflow boundary.

The outflow boundary model to a 3D axisymmetric model of the aorta was applied. The solution was shown to be consistent with clinical results, correctly capturing the dictrotic notch, the increasing and narrowing of the pressure peak, and the shifting of the second-highest peak. Furthermore, we saw that though the pressure peak increased, the average pressure decreased while traveling down the aorta, a physically realistic characteristic. Finally, it was demonstrated that this outflow condition produces the correct physiological phase shift between pressure and flow.

This boundary model has several advantages. It can account for both the resistance and volume compliance of a truncated vascular network, and it can be adjusted to have correct physiological wave arrival times. Furthermore, it is an excellent choice for researchers who are using black box software, as it can be easily employed in packages where it is often difficult or sometimes impossible to implement custom boundary conditions. It is important to note, however, that the outflow boundary model can only be used with fluid-solid interaction (FSI) modeling.

Our outflow boundary model may seem to be similar to Windkessel (RCR). However, it has been shown by Olufsen[30] that the Windkessel model is neither able to capture wave propagation phenomena in the parts of the vasculature where it applies, nor able to capture the phase lag between the pressure and flow [30].

Results have been shown for single outlets, but multiple outlets can be easily incorporated into our model by applying our outflow boundary model to each individual outlet. In cases such as in coronary arteries, where the resistance is variable during the cardiac cycle, our outflow model can be implemented by modifying the wall of the rigid contraction tube to a moving wall condition. For pulmonary arteries, modifications are necessary since these vessels have different wave dynamics due to lower wave reflections and variable resistance (dependent on arterial pressure)[7].

Chapter 3

LOW PULSE PRESSURE WITH HIGH PULSATILE EXTERNAL LEFT VENTRICULAR POWER: INFLUENCE OF AORTIC WAVES

This chapter is based on the following published manuscript: N. M. Pahlevan and M. Gharib. Low pulse pressure with high pulsatile external left ventricular power: Influence of aortic waves. *Journal of Biomechanics* 44(11): 2083-2089

3.1 Chapter Abstract

Elevated pulse pressure (*pp*) is considered to be a risk factor for adverse cardiovascular events since it is directly related to an elevated myocardial workload. Information about both pressure and flow wave must be provided to assess hemodynamic complexity and true level of external left ventricular power (ELVP). *pp* value as a single feature of aortic waves cannot identify true level of ELVP. However, it is generally presumed that ELVP (and consequently LV workload) is positively correlated with *pp*. This study examined this positive correlation. The aim of this chapter is to test the hypothesis that aortic wave dynamics can create destructive hemodynamic conditions that increase the ELVP even though *pp* appears to be normal. To test this hypothesis, a computational model of the aorta with physiological properties was used. A Finite Element Method with fluid-structure interaction was employed to solve the equations of the solid and fluid. The aortic wall was assumed to be elastic and isotropic. The blood was assumed to be an incompressible Newtonian fluid. Simulations were performed for various heart rates (HR) and different aortic compliances while keeping the shape of the inlet flow and peripheral resistance constant. As expected, in most of the cases studied here, higher *pp* was associated with higher LV power demand. However, for a given cardiac output, mean pressure, and location of total reflection site, cases have been found where the above-mentioned trend does not hold. The results suggest that using *pp* as a single index can result in an underestimation of the LV power demand under certain conditions related to the altered wave dynamics. Hence, in hypertensive patients, a full analysis of aortic wave dynamics (a

systems approach) is essential for the prevention and management of left ventricular hypertrophy (LVH) and congestive heart failure.

3.2 Introduction

The workload on the left ventricle (LV) is composed of steady and pulsatile components. The pulsatile load is the result of the complex dynamics of wave propagation and reflection in the compliant arterial vasculature. The dynamics depends on both the heart's pumping characteristics (stroke volume, heart rate, ejection fraction) and the arterial system's wave characteristics (wavelength, wave speed, and reflection sites)[7, 12, 58].

Pulse pressure (*pp*) is the difference between the peak and the foot of the pressure wave, and it has been known to be an indirect measure of pulsatile load on the LV. Clinical investigations have confirmed that an abnormal pulsatile load plays an important role in the pathogenesis of left ventricular hypertrophy (LVH) and progression of LVH to congestive heart failure (CHF)[37, 59-64]. Although the LV pulsatile load accounts only for approximately 6-12% of the total load in young healthy adults [65]; this percentage can increase significantly in subjects with vascular disease, hypertension, or vascular aging [66].

Wave dynamics in a compliant tube depends on three parameters: 1) fundamental frequency of the propagating waves 2) wave speed (which depends on material properties of the tube), and 3) reflection sites [8, 9, 67]. Therefore, for a given inlet flow wave generated by the heart, wave dynamics in the aorta (compliant tube) is controlled by the heart rate (fundamental frequency), aortic rigidity (which influences the wave speed), and location of the reflection sites.

The aim of this study was to test the hypothesis that aortic wave dynamics can create destructive hemodynamic conditions that increase the external LV power (ELVP) even though the *pp* appears to be normal. A computational approach was chosen to investigate our hypothesis since it enabled us to have better control over the various parameters that define wave dynamics and pulsatile ELVP. Some of these parameters are defined by the heart, such as cardiac output (CO), heart rate, and ejection fraction. Other parameters, such as wave speed, compliance, terminal compliance, peripheral resistance, and the location of the total reflection site are defined by the aorta and the arterial system. The focus was only on the parameters that characterize the wave dynamics and all the other parameters were fixed. Heart rate, aortic rigidity, and the location of the total reflection site are the characteristic parameters of aortic wave dynamics. These parameters are interrelated and define the state of wave dynamics in the aorta. By varying these parameters, one can obtain any desired pressure wave—referred to in this thesis as wave state (WS)—of the system. For example, the same WS can be generated at different heart rates by adjusting aortic rigidity and the location of the total reflection. Fifty six cases of WS were simulated through variations of the aortic rigidity (Young's modulus of the wall) and HR, both within physiological range.

3.3 Methods

3.3.1 Physical Model

A three-dimensional axisymmetric model of the aorta was used (Figure 3.1). The geometrical data of the aortic model, such as aortic length, inner diameter, and wall thickness, were within the average physiological range [6]. The change of stiffness along the aorta and tapering of the aorta were considered, but the aortic arc and bifurcations were excluded. The aortic wall was assumed to be elastic and isotropic. These material assumptions are applicable when modeling large central arteries, especially the aorta, but are not suitable for radial arteries or arterioles since these vessels are more anisotropic and viscoelastic[7]. It was also shown by Saito *et al* [68] that viscoelasticity of the vessel wall has insignificant effect on the development of the pressure and velocity waveform in large arteries, so the vessel's wall can be considered purely elastic. An objection to these wall assumptions might be the nonlinear dependency of the vessel's wall elasticity on the mean arterial pressure; however, for the normal mean pressure (less than *125 mmHg*) the relation is linear[7].

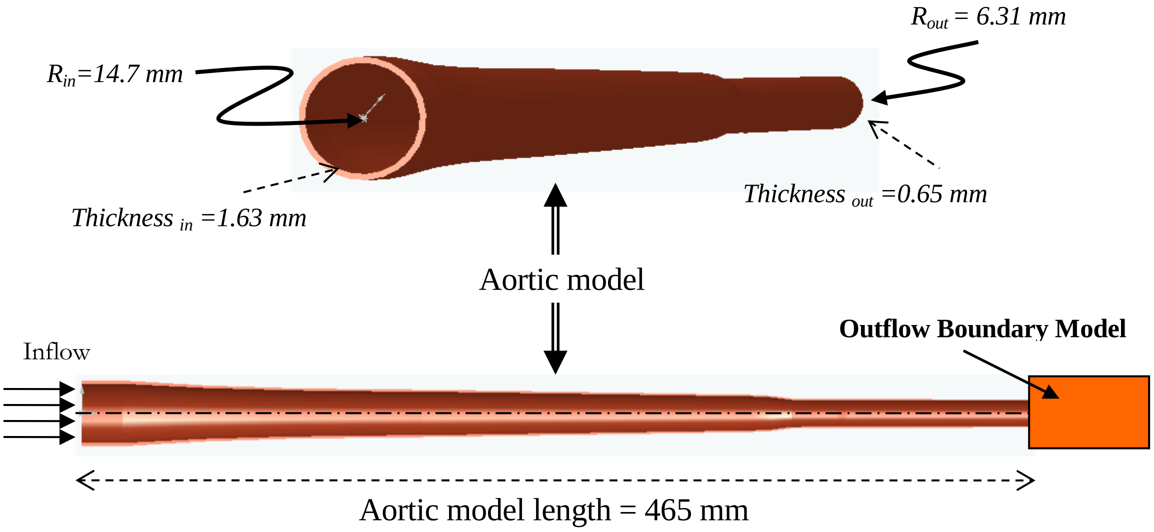

Figure 3.1: Aortic Model

The material properties of the wall were taken from Nichols *et al*[7]. The blood was assumed to be an incompressible Newtonian fluid. The physical parameters of the aortic model are provided in Table 3.1. Young's modulus values given in this table were referred to as aortic rigidity *E*, and all other cases of aortic rigidity were a specific factor of these values.

3.3.2 Mathematical Model

An arbitrary Lagrangian-Eulerian (ALE) formulation is used for the analysis of the fluid flow with moving boundaries. This formulation can be directly coupled with the Lagrangian formulation of the solid domain. In an ALE formulation for an incompressible fluid, the Navier-Stokes equations take the form shown in Equation 3.1[50-52]. With a no-slip boundary condition at the wall, the coupling equations at the solid-fluid interface are 1) displacement compatibility (Equation 3.2) and 2) traction equilibrium (Equation 3.3) at the wall.

$$\begin{cases} \vec{\nabla}.\vec{V} = 0\,, \\ \rho_f \left(\dfrac{\partial \vec{V}}{\partial t} + \left(\vec{V} - \overrightarrow{W}\right).\vec{\nabla}\vec{V} \right) + \vec{\nabla} p = \mu_f \nabla^2 \vec{V} + \vec{F}_b\,, \end{cases} \tag{3.1}$$

$$\vec{V}_f = \vec{\dot{u}}_s\,, \tag{3.2}$$

$$\vec{n}.\underline{\underline{\sigma_f}} = \vec{n}.\underline{\underline{\sigma_s}}. \tag{3.3}$$

In these equations $\vec{V}(V_y, V_z)$ is the flow velocity vector, p is the static pressure, μ_f is the dynamic viscosity of the fluid, $\vec{F}_b$ is the body force, $\overrightarrow{W}$ is the mesh velocity, $\vec{V}_f$ and $\vec{\dot{u}}_s$ are velocity of fluid and solid at the interface respectively, $\underline{\underline{\sigma_f}}$ is fluid stress tensor, and $\underline{\underline{\sigma_s}}$ is solid stress tensor.

For the solid domain, the wall was considered to be an elastic and isotropic material. The large deformation but small strain theory was used. Constitutive relation for a linear elastic isotropic material and a balance of momentum equation in Lagrangian form were used to calculate the dynamic motion of the elastic wall (Equations 3.4 and 3.5)[48, 49];

$$\sigma_{ij,j} + F_i = \rho_s \ddot{u}_i\,, \tag{3.4}$$

$$\sigma_{ij} = \lambda \varepsilon_{kk} \delta_{ij} + 2\mu_l \varepsilon_{ij}\,. \tag{3.5}$$

Here, σ_{ij} is the wall stress tensor, F is the external force, u is the displacement vector, ρ_s is the vessel wall density, and λ, μ_l are Lamé constants. The Lamé constants are related to ν (Poisson's ratio) and E (Young's modulus) $\lambda = E\nu/(1+\nu)(1-2\nu)$ and $\mu = E/2(1+\nu)$.

At the inlet, a physiological flow wave (Figure 3.2), from Matthys[57] , with a flat velocity profile was imposed and it was scaled to give a cardiac output (CO) of 4.6 *L/min* for any given heart rate.

Table 3.1
Physical parameters*

Parameter	Symbol	Value
Young's modulus of the sinus of Valsalva	E_{sin}	3.5×10^5 *Pa*
Young's modulus of the ascending aorta	E_{asc}	4.2×10^5 *Pa*
Young's modulus of the descending aorta	E_{des}	4.7×10^5 *Pa*
Young's modulus of the upper part of the abdominal aorta	E_{upab}	5.3×10^5 *Pa*
Young's modulus of the lower part of the abdominal aorta	E_{lowab}	8.6×10^5 *Pa*
Blood density	ρ_f	1050 kg/m^3
Blood viscosity	μ_f	0.0051 *kg/m.sec*
Aortic wall density	ρ_s	1050 kg/m^3
Aortic wall Poisson's ratio	ν	0.45
Wall thickness of the sinus of Valsalva	h_{sin}	1.6 *mm*
Wall thickness of the ascending aorta	h_{asc}	1.4 *mm*
Wall thickness of the descending aorta	h_{des}	1 *mm*
Wall thickness of the upper part of the abdominal aorta	h_{upab}	0.9 *mm*
Wall thickness of the lower part of the abdominal aorta	h_{lowab}	0.8 *mm*

Since the physical parameters vary in each aortic wall section, the average values within the sections have been given. Young's modulus values in this table are for the case of minimum rigidity in this study (E_1). The sinus of Valsalva and the ascending aorta are the regions ($0<z<2$ *mm*) and ($2<z<10$ *mm*) respectively, where z is the distance from the aortic input.

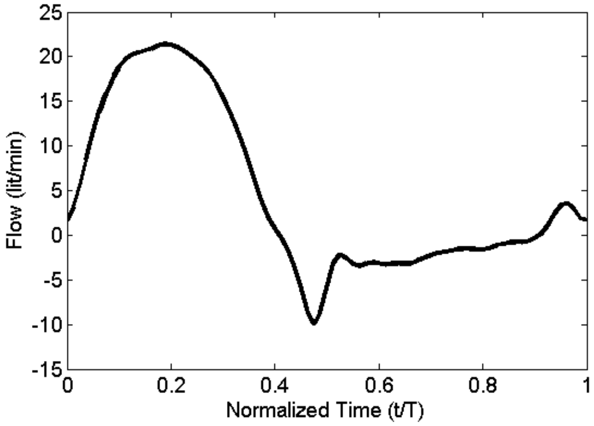

Figure 3.2: Input flow wave (cardiac output = 4.6 L/min)

The outflow boundary is the extension tube boundary condition (See Chapter 2 for details)[69]. This outflow boundary model involves extending the computational domain by an elastic tube connected to a rigid contraction tube (a contracted radius midway down its length). The user-defined geometrical and material properties of these boundary tubes (Table 3.2) allow us to retain the desired resistance, compliance and wave reflections of the truncated vascular network.

Table 3.2
Outflow boundary parameters

Description	Value
The inner radius of the elastic boundary tube	6.31 mm
Total length of the elastic boundary tube	105 mm
Total length of the rigid boundary tube	283 mm
Wall thickness of the elastic boundary tube	0.65 mm
Total volume compliance of the boundary model	$9.96 \times 10^{-11}\ m^3/Pa$
Contraction ratio of the rigid boundary tube*	0.76

The contraction ratio is defined as the ratio of the radii of the rigid boundary tube after contraction to that before contraction.

3.3.3 Computational Model

The finite element method with the direct two-way coupling method of fluid-structure interaction (FSI) was employed to solve the equations of solid and fluid at each time step. The time integration scheme was the implicit Euler method with a time step of 0.00125s. A total number of 17,416 three-node 3D axisymmetric elements were used for the fluid domain, and a total of 2420 nine-node 3D axisymmetric elements were used in the solid domain. Further simulations with different time steps and mesh sizes showed that the results were independent of spatial and temporal discretizations. The commercial package ADINA, version 8.6 (ADINA R&D, Inc., MA) was used to run the simulations[49, 50].

3.3.4 Wave Analysis Method

To analyze the obtained solution, the wave intensity (WI) method was used, developed by Parker *et al* [41], as a time domain analysis of wave propagation in the arterial system. It is based on the well-known method of characteristics which follows the propagation of individual wave fronts characterized by incremental changes in pressure *dp* and velocity dU [41],

$$dI = dp.dU \quad . \tag{3.6}$$

The wave intensity has a unit of power per area and it is an index of energy per unit area carried by the wave[70]. WI can be decomposed into forward (+) and reflected (-) waves as[44, 45]

$$dI_{+} = \frac{1}{4\rho c}(dp + \rho c\, dU)^2 \tag{3.7}$$

$$dI_{-} = \frac{-1}{4\rho c}(dp - \rho c\, dU)^2. \tag{3.8}$$

The PU-loop method was used to compute the wave speed (c)[44]. This method uses the slope of the pressure-velocity curve at the beginning of the cycle when reflected waves are absent. At the beginning of the cycle: $dp = dp+$ and $dU = dU+$; therefore, $dp+ = \rho cdU+$ and the slope of the PU-loop curve gives ρc. The value for ρc was then substituted into Equations 3.7 and 3.8 for $dI+$ and *dI*- calculations [44]. The PU-loop method, like any other method of wave speed calculation, may contain errors. However, it has been shown that even 20% error in calculation of the wave speed does not significantly changes the pattern of the reflected wave intensity[44] (see Appendix A for more details).

3.3.5 Power Calculation

The total power ($\bar{P}_{total}$) was calculated as the average of the product of the pressure ($p(t)$) and flow ($q(t)$) over a cardiac cycle. The steady power ($\bar{P}_s$) is the product of mean pressure (p_{mean}) and mean flow (q_{mean}), and the pulsatile ELVP ($\bar{P}_{pulse}$) is the difference between the total power and steady power,

$$\bar{P}_{total} = \frac{1}{T}\int_{0}^{T} p(t)q(t)dt, \tag{3.9}$$

$$\bar{P}_s = p_{mean}q_{mean}\ , \tag{3.10}$$

$$\bar{P}_{pulse} = \bar{P}_{total} - \bar{P}_s\ . \tag{3.11}$$

3.4 Results

To test the hypothesis, fifty-six different cases of aortic wave dynamic states were generated by varying the HR and aortic rigidity. The heart rates ranged from 70.5 bpm to 187.5 bpm. The rigidity levels used were multiplicative factors of $E_1(x)$ (Table 3.1) as $E_2=1.25E_1$, $E_3=1.5E_1$, $E_4=1.75E_1$, $E_5=2E_1$, $E_6=2.5E_1$, and $E_7=3E_1$. In all simulations, cardiac output, peripheral resistance, terminal compliance, and the shape of the inflow wave were kept constant. Results were normalized in time with the period of the cardiac cycle.

3.4.1 Pressure Wave Solution

To study the validity of our computational model, four well-known features of pressure waves in a human aorta were considered [7, 46]: (i) the pulse pressure amplification; (ii) the narrowing of the pressure waves as they travel down the aorta; (iii) the existence of a dicrotic notch; and (iv) the shifting of the second-highest pressure peak to the end of the cycle. Indeed, all four features were clearly captured by our computational model as shown in Figure 3.3. This figure also demonstrates an important physical feature of blood flow in the aorta: the mean pressure is slightly decreased due to viscous losses.

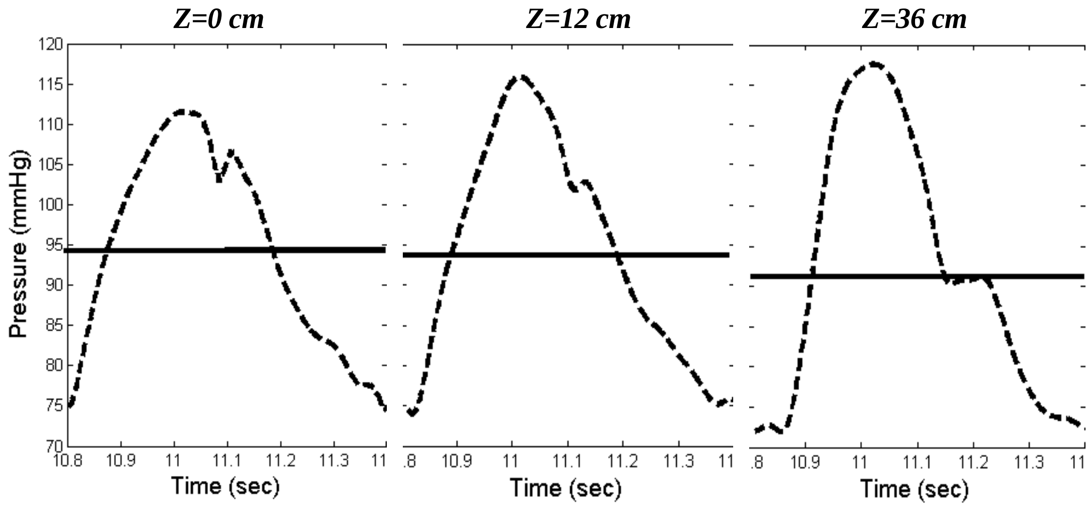

Figure 3.3: Simulated results from the aorta model showing the (i) pulse pressure amplification, (ii) pressure narrowing, (iii) shifting of the second-highest peak, and (iv) the existence of the dicrotic notch. The average per cycle (black straight line) decreases due to losses. Data is for a 100 bpm heart rate and an aortic rigidity of E_1 taken during one cycle. Z is the distance from aortic input.

3.4.2 Normal Cases: When Higher Pulsatile ELVP Is Associated with Higher Pulse Pressure

Figure 3.4a shows the three cases of aortic wave states named WS_a, WS_b, and WS_c. In these cases, higher *pp* is associated with higher pulsatile ELVP ($\bar{P}_{pulse}$) :

$$pp_c > pp_b > pp_a \quad \Longrightarrow \quad \bar{P}_{pulse}(WS_c) > \bar{P}_{pulse}(WS_b) > \bar{P}_{pulse}(WS_a). \tag{4.12}$$

Using Equation 3.8, the reflected (backward) wave intensity (RWI) was calculated for the three cases of WS above. The corresponding RWI graph is shown in Figure 3.4b. All wave states demonstrate three distinct peaks of decreasing amplitude for RWI (The peaks correspond to the first, second and third generation of the reflected waves and the decreasing amplitude is due to the attenuation of the waves as they travel through) where, clearly, higher power is associated with the higher peaks. The amplitude of the first peak of RWI is also correlated with *pp*.

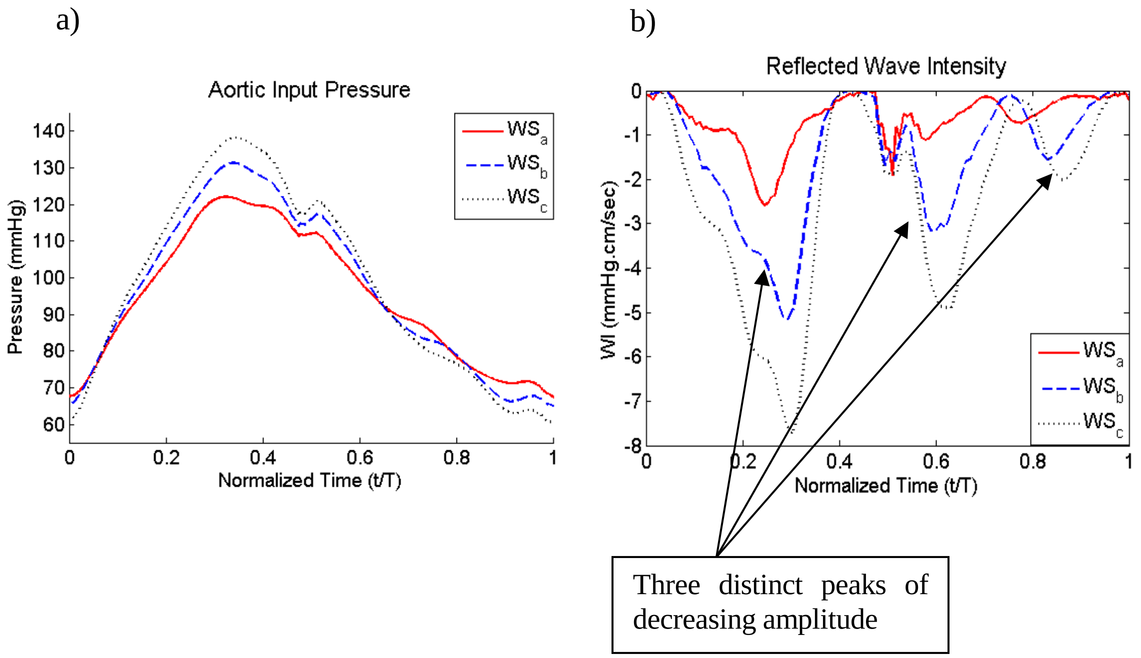

Figure 3.4: a) Pressure waves at the aortic input during a complete cardiac cycle. The time was normalized with the cardiac period (*T*). In these cases, higher pulse pressure is associated with higher pulsatile ELVP ($\bar{P}_{pulse}$). The pulsatile ELVP for WS_a, WS_b, and WS_c are *55.84*, *66.28*, and *77.38mW* respectively. The pulse pressures are pp_a=*54.64 (mmHg)*, pp_b=*66.24 (mmHg)*, and pp_c=*73.75 (mmHg)*. b) Wave intensity of reflected waves at the aortic input during a complete cardiac cycle. Three distinct peaks of decreasing amplitude (corresponding to the first, second and third generational reflected waves, respectively) are observed for all cases. The time was normalized with the cardiac period (*T*). The length of the incremental time interval for calculating dI_- was $dt = 0.00625\ s$.

3.4.3 Abnormal Cases: When Higher Pulsatile ELVP Is Not Associated with Higher Pulse Pressure

Figure 3.5 shows pressure waves and RWI for an example aortic wave state with abnormally elevated pulsatile ELVP. For comparison, a normal wave state (WS$_1$) is also shown against the abnormal case (WS$_2$), where WS$_1$, and WS$_2$ have pulse pressures $pp_1 = 52.6\,(mmHg)$, $pp_2 = 37.8\,(mmHg)$ and respective pulsatile LV powers of $\bar{P}_{pulse}(WS_1) = 66.28\,(mW)$, and $\bar{P}_{pulse}(WS_2) = 77.15\,(mW)$. Although WS$_2$ has a *pp* that is 14.8 mmHg (28.1%) lower than WS$_1$, it retains a higher (16.3%) pulsatile ELVP. The wave intensity graph of the WS$_1$ is just as the normal cases demonstrated above (three distinct peaks of decreasing amplitude.) In contrast, the second and third RWI peaks of WS_2 were replaced with a single peak of greater magnitude than the first peak. Similar to normal cases shown before, the wave state (WS_1) has a first peak RWI with higher amplitude.

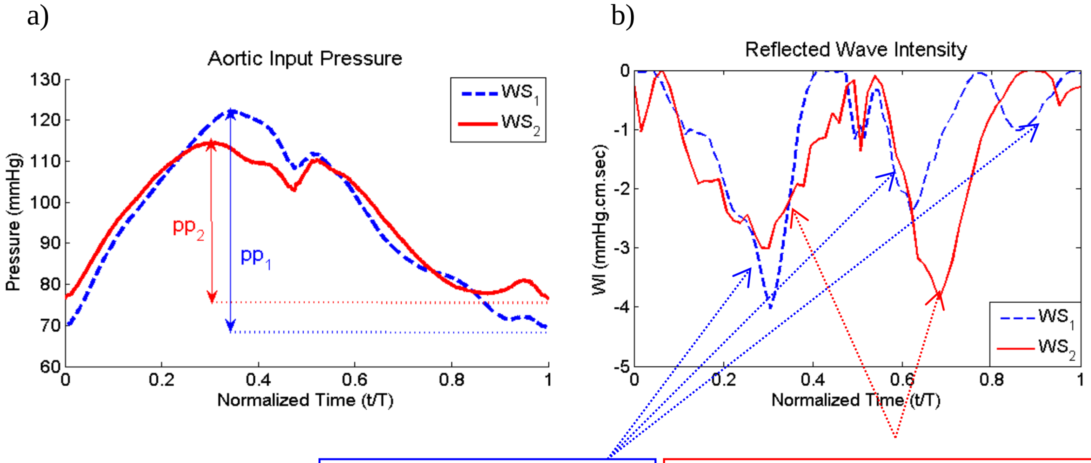

Three distinct peaks of decreasing amplitude

Second and third peaks were replaced with a single peak of greater magnitude than the first peak

Figure 3.5: Pressure waves (left) and their reflected wave intensity (right) at the aortic input during a complete cardiac cycle for waves states 1 and 2 (WS_1 and WS_2). The length of the incremental time interval for calculating *dI-* was $dt = 0.00625\ s$. The time was normalized with the cardiac period (T). The case WS_2 (solid line) has *14.8 mmHg* lower *pp* compared to WS_1 (dash line), but pulsatile ELVP ($\bar{P}_{pulse}$) of WS_2 is abnormally 16.3% higher compared to WS_1. Both pressure waves have approximately the same mean. (See Table 3.3 for values). Notice how the second and third peaks of WS_2 are replaced with single bigger amplitude peak. Also, WS_2 has a lower *pp* and lower first RWI peak amplitude.

Table 3.3

pp, $\bar{P}_{pulse}$, and p_{mean} of the cases given in Figures 3.5-7

Wave State	Pulse Pressure	Pulsatile LV Power	Mean Pressure
WS_1	52.6 (mmHg)	66.28 (mW)	95.8 (mmHg)
WS_2	37.8 (mmHg)	77.15 (mW)	96.3 (mmHg)
WS_3	37.1 (mmHg)	49.23 (mW)	94.4 (mmHg)
WS_4	23.0 (mmHg)	64.38 (mW)	94.6 (mmHg)
WS_5	89.5 (mmHg)	105.60 (mW)	97.9 (mmHg)
WS_6	34.4 (mmHg)	109.30 (mW)	96.7 (mmHg)

Further examples of abnormally elevated pulsatile ELVP are shown in Figures 3.6 and 3.7, with the pressure and power values summarized in Table 3.3. Again, each of these abnormal cases, WS_4 and WS_6, are shown against normal cases, WS_3 and WS_5, respectively. In particular, note in Figure 3.7 that WS_6 has an apparently normal *pp* of 34.4 mmHg, but due to destructive wave interaction within the aorta, the pulsatile ELVP that it applies on the left ventricle is remarkably similar to a significantly higher *pp* of 89.5 mmHg (WS_5). As before, there is a positive correlation between the amplitude of the first peak of RWI and *pp* in all of the cases shown here. Although the results of each WS do not depend on specific choice of HR and aortic rigidity as explained earlier, these value are provided in Table 3.4.

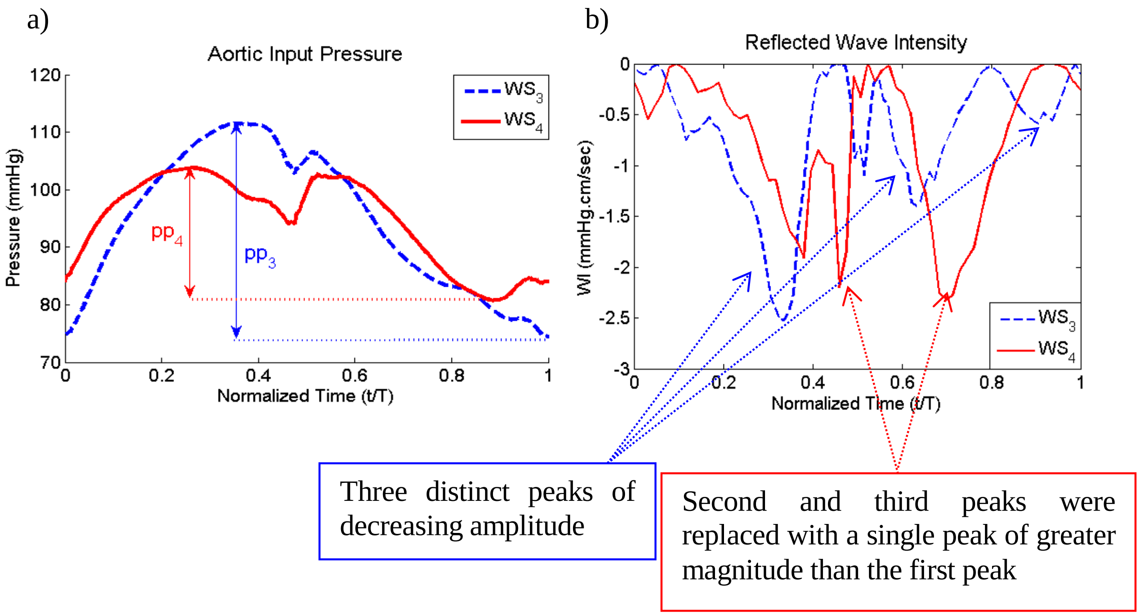

Three distinct peaks of decreasing amplitude

Second and third peaks were replaced with a single peak of greater magnitude than the first peak

Figure 3.6: Pressure waves (left) and their reflected wave intensity (right) at the aortic input during a complete cardiac cycle for wave states WS_3 and WS_4. The time was normalized with the cardiac period (T). The length of the incremental time interval for calculating dI_- was $dt = 0.00625\ s$. The case WS_4 (solid line) has *14.1 mmHg* lower *pp* compared to WS_3 (dash line), but pulsatile ELVP ($\bar{P}_{pulse}$) of WS_4 is 30.8% higher compared to WS_3. Both pressure waves have approximately the same mean. (See Table 3.3 for values). Notice again how the second and third peaks of WS_4 replaced with single bigger amplitude peak. Also, WS_4 has a lower *pp* and lower first RWI peak amplitude.

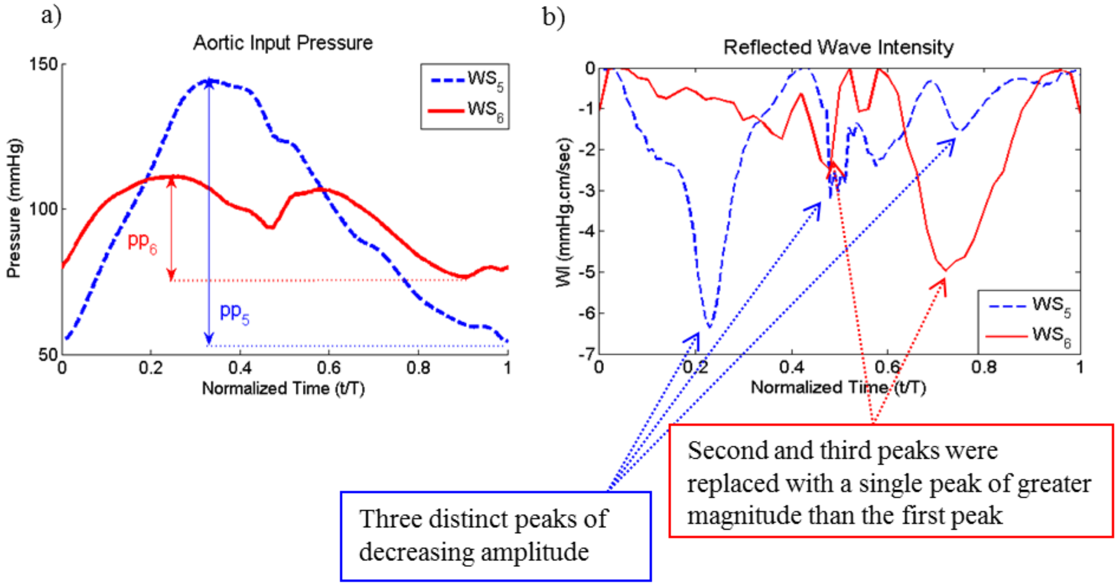

Three distinct peaks of decreasing amplitude

Second and third peaks were replaced with a single peak of greater magnitude than the first peak

Figure 3.7: Pressure waves (left) and their reflected wave intensity (right) at the aortic input during a complete cardiac cycle for wave states WS_5 and WS_6. The time was normalized with the cardiac period (T). The length of the incremental time interval for calculating dI_- was $dt = 0.00625\ s$. pp_6 (red) of WS_6 seems to be normal ($=34.4\ mmHg$), but its pulsatile ELVP ($\bar{P}_{pulse}$) is slightly higher (3.5%) than pp_5 ($=89.5\ mmHg$) of WS_5. Both pressure waves have approximately the same mean (See Table 3.3 for values). Notice that the second and third peaks of WS_6 are replaced with single bigger amplitude peak. Also, WS_6 has a lower *pp* and lower first RWI peak amplitude.

Table 3.4
Rigidity and *HR* of the wave states (WS) in Figures 3.4-7

Wave State	Rigidity	HR (bmp)
WS_a	E_1	70
WS_b	E_3	100
WS_c	E_5	120
WS_1	E_2	100
WS_2	E_3	150
WS_3	E_1	100
WS_4	E_1	150
WS_5	E_3	75
WS_6	E_3	187

3.5 Discussion

These results demonstrate for the first time that even with a low *pp*—at a specific mean pressure—the external left ventricular power (ELVP) can be high. We showed that complex wave dynamic phenomena in the aorta can create destructive hemodynamic conditions that can increase the external left ventricular power. Though *pp* has long been thought to be a surrogate of LV pulsatile load, our findings demonstrate that these adverse wave conditions cannot be diagnosed by monitoring the pulse pressure alone. It is generally accepted that *pp* value as a single feature of aortic waves cannot identify the hemodynamic complexity and true level of external left ventricular power (ELVP). Therefore, information about both pressure and flow wave must be provided to assess ELVP and hemodynamic complexity, as waves depend on parameters such as HR, stroke volume, duty cycle, reflection sites, arterial stiffness, and peripheral resistance.

Pulse pressure (*pp*) is still a significant feature of the pressure wave that reflects the complex interaction between the heart pumping condition and the wave characteristics of the arterial network. Increased LV workload has been proposed as a plausible mechanism underlying the association between increased *pp* and the development of LVH and CHF[37, 60, 63, 66, 71, 72]. Hence, high *pp* and an abnormal pulsatile load have become a potential target for therapeutic intervention[66].

Indeed, in wave dynamics under normal conditions, a higher pulse pressure corresponds to a higher pulsatile ELVP. Wave states under these normal conditions show a similar shape in the reflected wave intensity graph, namely three distinct peaks of decreasing amplitude over time (see Figure 3.4). Each of the first, second and third peaks correspond to the first, second and third generation, respectively, of reflected waves. The decreasing amplitude is due to the attenuation of the waves as they travel through.

However, due to certain wave interactions, there exist abnormal conditions where a higher pulsatile ELVP does not follow from a higher pulse pressure. In these cases, the second and third peaks, which have low amplitude, are replaced with a single peak of higher amplitude. The appearance of this single peak might be the result of a resonant condition between the second and third generation of reflected waves. We showed in Figures 3.5-7 examples of abnormally elevated loads from different levels of pulse pressures and aortic rigidities. In Figure 3.5, although WS_1 has a pulse pressure of 14.8 mmHg (28.1%) higher than WS_2, it has a 10.87 mW (16.3%) lower pulsatile ELVP. Figures 3.6 and 3.7 show further varying examples of destructive wave dynamics that cause abnormal elevations of pulsatile ELVP. A particularly interesting example is shown in Figure 3.7 where, although WS_6 has a normal pulse pressure (34.4 mmHg), its pulsatile ELVP is very similar to a case of dangerously high pulse pressure (WS_5, 89.5 mmHg).

In all cases (either normal or abnormal)—as shown in Figures 3.4-7—the *pp* was positively correlated with the amplitude of the first peak of the RWI. It can be conjectured that the first peak of RWI is the main contributor to the elevation of *pp*. A plausible explanation is that the first high energy reflected wave—represented by the first peak—always needs to be overcome by the inflow waves, hence elevating the pulse pressure. Therefore, in cases WS_1-WS_6 when the first peak of RWI is smaller, the corresponding *pp* is lower. In contrast, in abnormal wave states, there is a second peak with amplitude larger than the first. This second larger peak is the result of the destructive interaction of reflected waves in the aorta that elevate the pulsatile ELVP, but it does not have a significant influence on *pp*.

It must be mentioned again that the purpose of changing HR and Young's modulus is to generate different WS. Since HR, rigidity (Young's modulus), and location of the reflection site are interrelated, every WS can be generated by fixing one and changing the other two. This also means that the same WS can be generated at two different HR by two different rigidities and locations of reflection sites.

The advantage of the computational approach used in this study is to allow control and flexibility over determining parameters—defined by the heart, aorta and arterial system—to achieve particular wave states and pulsatile ELVPs. However, it would be interesting to conduct a clinical study to reconfirm these findings.

The computational model used here is limited by the exclusion of aortic branches and the aortic arch. However, the influence of the branches is accounted for by considering the fact that they produce summated reflected waves from the upper body and lower body sites or, in some cases, a single reflection site [73]. These summated reflected waves are included in the outflow boundary condition of the model, but only from a lower body site. This is due to the fact that majority of wave reflection comes from the lower part of the body, and the peak of the aortic pulse is also created mostly by reflected waves from the lower body[7]. Therefore, exclusion of the wave reflection from upper body doesn't affect the overall finding of this study.

The exclusion of the aortic arch is justified by the fact that, although the flow pattern is significantly influenced by the arch, there is no significant effect on the pressure wave (which is the focus of this study). In fact, the pressure wave shows little or no detectible change when transmitted from the aortic input through the arch and into the upper descending thoracic aorta[7].

3.6 Conclusion

Our computational study suggests that using *pp* as a single index can result in an underestimation of the level of LV workload under abnormal wave conditions. Pulse pressure (*pp*) only provides limited information about the pressure wave in the aorta. It is generally assumed that *pp* is positively correlated with external LV power—and as result to LV workload. In order to identify the true level of workload on LV, information about both pressure and flow waves is required. These two waves are 1) a function of heart pumping characteristics (HR, stroke volume, and duty cycle) and 2) a function of properties and the arterial network (reflection sites, stiffness, and peripheral resistance). Therefore, in hypertensive patients, a full analysis of wave dynamics in the aorta is essential for the prevention and management of LVH and CHF. It was shown that due to the destructive interaction of aortic waves, the pulsatile ELVP can still be abnormally high when pulse pressure seems normal.

Additional studies are needed to specifically evaluate the aortic wave dynamic effects on the pathogenesis of HF and the development of novel therapies. Further clinical studies are also needed to see whether the abnormal RWI pattern (the resonance of the second and third peaks) can be used as a predictor of LVH in young adults and cardiovascular complications in the elderly.

Chapter 4

AORTIC WAVE DYNAMICS AND ITS INFLUENCE ON LEFT VENTRICULAR WORKLOAD

This chapter is based on the following published manuscript: N. M. Pahlevan and M. Gharib. Aortic Wave Dynamics and Its Influence on Left Ventricular Workload. *PLoS ONE* 6(8): e23106

4.1 Chapter Abstract

The pumping mechanism of the heart is pulsatile, so the heart generates pulsatile flow that enters into the compliant aorta in the form of pressure and flow waves. It was hypothesized that there exists a specific heart rate at which the external left ventricular (LV) power is minimized. To test this hypothesis, a computational model was used to explore the effects of heart rate (HR) and aortic rigidity on left ventricular (LV) power requirement. While both mean and pulsatile parts of the pressure play an important role in LV power requirement elevation, at higher rigidities the effect of pulsatility becomes more dominant. For any given aortic rigidity, there exists an optimum HR that minimizes the LV power requirement at a given cardiac output. The optimum HR shifts to higher values as the aorta becomes more rigid. To conclude, there is an optimum condition for aortic waves that minimizes the LV pulsatile load and consequently the total LV workload.

4.2 Introduction

Congestive heart failure (CHF) has reached an epidemic proportion in the US and worldwide with serious consequences in terms of human suffering and economic impact. In the US alone, there are 60,000 patients dying each year with CHF as the underlying cause. Approximately 5,800,000 Americans have been diagnosed with this condition and this number is increasing every year[1]. In the absence of myocardial infarction, hypertension is a primary risk factor of CHF [74] mainly due to the chronic elevation of the left ventricular (LV) workload and the development of left ventricular hypertrophy (LVH)[59, 61, 75].

Pulsatile flow generated by the heart enters the compliant aorta as pressure and flow waves. These waves propagate and reflect throughout arterial vasculature, thus playing a dominant role in the hemodynamics of the arterial system. The hemodynamic load on the heart has two parts: steady and pulsatile. The steady load is the result of the resistance from the arterial network to the mean part of the flow. The pulsatile load depends on the interaction between the heart's pumping characteristics (stroke volume, heart rate, and ejection fraction) and arterial wave dynamics. Significant efforts have been made in the past to elucidate the role of wave reflections in heart failure [34, 37, 59]. Clinical studies have confirmed that abnormal pulsatile loads play an important role in the pathogenesis of left ventricular hypertrophy (LVH) and CHF[61, 63, 66]. O'Rourke[65] suggested four important factors that control the level of the pulsatile load applied to the heart: 1) rigidity of the aorta and other large vessels, 2) interaction between the left ventricular and the terminal of the vasculature in the upper and lower parts of the body, 3) wave reflection, and 4) balance between the heart rate and the body length. He showed in an animal (dog) study that the ratio of the pulsatile load over the total load decreased as the heart rate increased, and that the ratio increased as the aortic distensibility decreased. However, previous studies did not investigate the interplay between aortic rigidity and heart rate (HR)[65].

The wave dynamics in a compliant tube is controlled by the fundamental frequency of the propagating waves, the material properties of the tube, and wave reflections[8, 9]. Similarly, aortic wave dynamics depend on heart rate, aortic compliance, and the locations of reflection sites. I hypothesized that there exists a specific heart rate at which LV pulsatile load becomes a minimum for a given physiological condition.

To test the hypothesis, a computational approach was implemented in order to be able to examine a large spectrum of wave states. This approach enabled us to study aortic rigidity and HR while having a better control on parameters such as the aortic input flow wave (ventricular ejection wave), terminal compliance, peripheral resistance (PR), cardiac output (CO), and the locations of reflection sites.

The goal in this chapter is to investigate the effects of different states of aortic wave dynamics on the LV power requirement (LVPR). Various states of aortic wave dynamics are produced by changing the heart rate and aortic wall rigidity (aortic compliance) while fixing other determinant factors of wave dynamics and power requirements.

4.3 Methods

4.3.1 Physical Model

A three-dimensional axisymmetric model of the aorta was used (Figure 4.1). The geometrical data of the aortic model, such as aortic length, inner diameter, and wall thickness, were within the average physiological range[6]. The aortic wall was assumed to be elastic and isotropic. These wall material assumptions are applicable when modeling large central arteries, especially the aorta, but may not be suitable for radial arteries or arterioles since these vessels are more anisotropic and viscoelastic[7]. A further concern about this wall assumption might be the nonlinear dependency of the vessel's wall elasticity on the mean arterial pressure; however, for the normal mean pressure (less than 125 mmHg), the relation is linear [7]. The material properties of the wall were taken from Nichols *et al*[7]. The tapering and the change of wall stiffness along the aorta were considered, though the aortic arc and bifurcation were excluded since the model is 3D axisymmetric. The blood was assumed to be an incompressible Newtonian fluid, and the different levels of aortic rigidity considered were multiplicative factors of a minimum rigidity level $E_1(x)$ (x is the distance from the heart) of a healthy 30-year-old man taken from Nichols *et al*[7]. The physical parameters of the aortic model are summarized in Table 4.1.

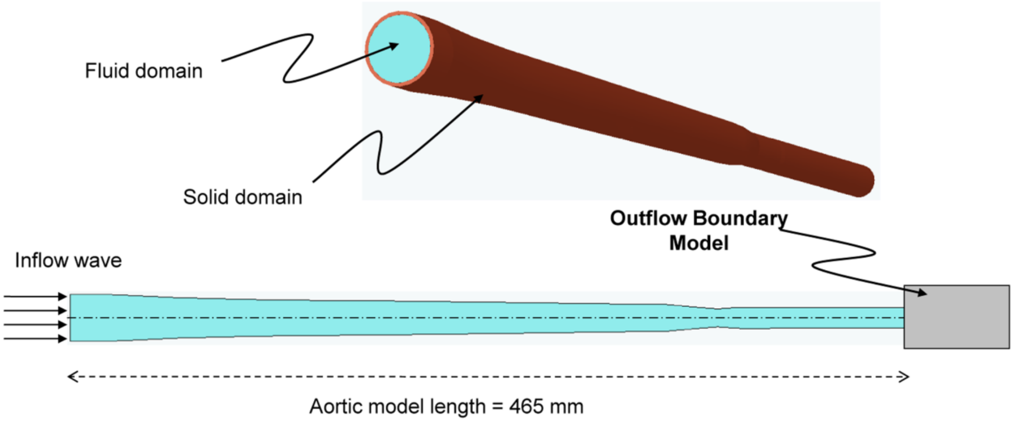

Figure 4.1. Computational model of the aorta.

Table 4.1.
Physical parameters*

Parameters	Symbol	Value
Blood density	ρ_f	1050 kg/m^3
Blood viscosity	μ	0.0051 $kg/m.sec$
Aortic wall density	ρ_s	1050 kg/m^3
Young's modulus of the sinus of Valsalva	E_{sin}	$3.5\times10^5\ Pa$
Young's modulus of the ascending aorta	E_{asc}	$4.2\times10^5\ Pa$
Young's modulus of the descending aorta	E_{des}	$4.7\times10^5\ Pa$
Young's modulus of the upper part of the abdominal aorta	E_{upab}	$5.3\times10^5\ Pa$
Young's modulus of the lower part of the abdominal aorta	E_{lowab}	$8.6\times10^5\ Pa$
Aortic wall Poisson's ratio	υ	0.45
Wall thickness of the sinus of Valsalva	h_{sin}	1.6 mm
Wall thickness of the ascending aorta	h_{asc}	1.4 mm
Wall thickness of the descending aorta	h_{des}	1 mm
Wall thickness of the upper part of the abdominal aorta	h_{upab}	0.9 mm
Wall thickness of the lower part of the abdominal aorta	h_{lowab}	0.8 mm

*Since the physical parameters vary in each aortic section, the average values within the sections have been given. The Young's modulus values in this Table are for the case of minimum rigidity (E_1)

At the inlet, a physiological flow wave (Figure 4.2), from Matthys[76], with a flat velocity profile was imposed and it was scaled to give a cardiac output (CO) of 4.6 L/min for any given heart rate.

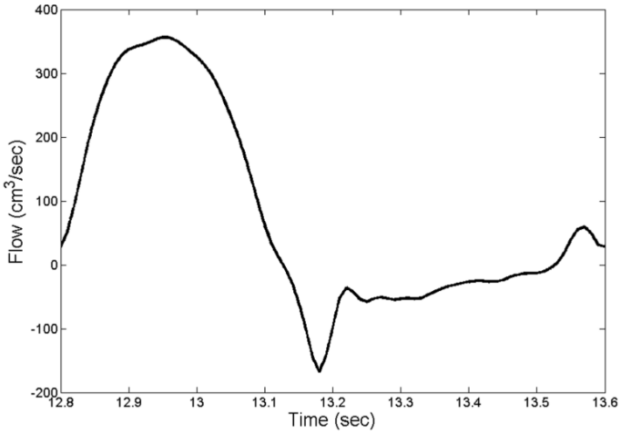

Figure 4.2. Inflow wave

4.3.2 Mathematical Model

4.3.2.1 Solid Model

Large deformation with small strain theory was assumed for the formulation of elastic wall motion.[17] It is assumed that the walls are composed of elastic isotropic material. Dynamic motion of the aortic wall was formulated by a constitutive relation for linear elastic isotropic materials and balance of momentum equations in Lagrangian form as[48, 49]

$$\sigma_{ij,j} + F_i = \rho_s \ddot{u}_i \,, \tag{4.1}$$

$$\sigma_{ij} = \lambda \varepsilon_{kk} \delta_{ij} + 2\mu_l \varepsilon_{ij} \,. \tag{4.2}$$

Here, σ_{ij} is the wall stress tensor, F is the external force, u is the displacement vector, ρ_s is the vessel wall density, and λ, μ_l are Lamé constants.

4.3.2.2 Fluid Model

To solve for pressure and flow fields in the fluid domain, the full Navier-Stokes (N-S) equations was used. In Eulerian form, they are

$$\vec{\nabla}.\vec{V} = 0 \,, \tag{4.3}$$

$$\rho_f \left(\frac{\partial \vec{V}}{\partial t} + \vec{V}.\vec{\nabla}\vec{V} \right) + \vec{\nabla} p = \mu_f \nabla^2 \vec{V} + \vec{F}_b \,, \tag{4.4}$$

where $\vec{V} = (v_y, v_z)$ represents the flow velocity vector, ρ_f is the fluid density, p is the static pressure, μ_f is the dynamic viscosity of the fluid, and $\vec{F}_b$ is the body force.

Since our fluid domain has moving boundaries, an arbitrary Lagrangian-Eulerian (ALE) formulation is used for the analysis of the fluid flow[50-53]. This formulation can be directly coupled with the Lagrangian formulation of the solid domain. In an ALE formulation, the total time derivative (*D/Dt*) for all the solution variables is given by [54]

$$\frac{D(.)}{Dt} = \frac{\partial(.)}{\partial t} + (\vec{V} - \vec{W}).\vec{\nabla}(.), \tag{4.5}$$

where $\partial(.)/\partial t$ is the transient term at the mesh position, $\vec{W}$ is the mesh velocity, and $\vec{V}$ is the actual fluid particle velocity. Applying Equation 4.5 in Equation 4.4 gives [54]

$$\rho_f \left(\frac{\partial \vec{V}}{\partial t} + (\vec{V} - \vec{W}).\vec{\nabla}\vec{V} \right) + \vec{\nabla} p = \mu_f \nabla^2 \vec{V} + \vec{F}_b \,. \tag{4.6}$$

4.3.2.3 Coupling Conditions

With no-slip boundary conditions at the wall, the coupling equations at the solid-fluid interface are

$$\vec{V}_f = \vec{\dot{u}}_s \text{ (Velocity condition)}, \tag{4.7}$$

$$\vec{n}.\underline{\underline{\sigma}}_f = \vec{n}.\underline{\underline{\sigma}}_s \text{ (Traction equilibrium)}, \tag{4.8}$$

where $\vec{V}_f$ and $\vec{\dot{u}}_s$ are the respective velocities of the fluid and solid at the interface, $\underline{\underline{\sigma_f}}$ is fluid stress tensor, $\underline{\underline{\sigma_s}}$ is solid stress tensor, and $\vec{n}$ is the unit vector in the normal direction.

4.3.2.4 Boundary Conditions

A novel extension tube boundary model was used for the outflow boundary condition at the terminal of the abdominal aorta. This boundary model extends the computational domain with a straight elastic tube connected to a contracted rigid tube (see Chapter 2 for details)[77]. Parameters such as the ratio of the radii of the rigid tube together with the length and elasticity of the elastic boundary tube are selected to represent the effects of a truncated vascular network (resistance, compliance, and wave reflection)[77].

The parameters of the outflow boundary condition model are given in Table 4.2, where the contraction ratio is the ratio of the radius of the rigid boundary tube beyond the contraction to the original radius before the contraction. The parameters of outflow boundary condition were kept the same for all simulations.

Table 4.2.
Outflow boundary parameters

Description	value
The inner radius of the elastic boundary tube	6.31 *mm*
Total length of the elastic boundary tube	105 *mm*
Wall thickness of the elastic boundary tube	0.65 *mm*
Contraction ratio of the rigid boundary tube	0.76
Total volume compliance of the boundary model	$9.96 \times 10^{-11}\ {}^{m^3}\!/_{Pa}$

4.3.3 Numerical Method

A finite-element scheme was applied to solve the equations of the solid and fluid models incrementally in time using the commercial package ADINA 8.6 (ADINA R&D, Inc., MA). A direct two-way coupling fluid-structure interaction (FSI) method (simultaneous solution method) was used to couple the fluid and solid domains at the interface. In this method, the discretized fluid, solid, and coupling equations are all combined in one matrix[50]. In summary, the general computational steps in the employed direct coupling method were (i) to assemble the solid and fluid equations separately into a single fluid and single solid model; (ii) to assemble the solid matrix, fluid matrix, and the coupling matrices into one coupled matrix system; (iii) to solve the linearized equation of the coupled system and to update the solution; and (iv) to compute and check the residuals against the specified tolerance. If the solution did not converge, the process was restarted from step (i)[50, 77].

An implicit Euler backward method with Newton-Raphson iteration was used for the time integration with a time step of 0.00125s. A total of 2420 nine-node axisymmetric elements were used to mesh the solid domain, and a total of 17,416 three-node axisymmetric elements were used for the fluid domain. Further simulations with different time steps and mesh sizes confirmed that these results were independent of spatial and temporal discretizations. All simulations started from rest until the mean of the aortic input pressure reached a steady state as shown in Figure 4.3.

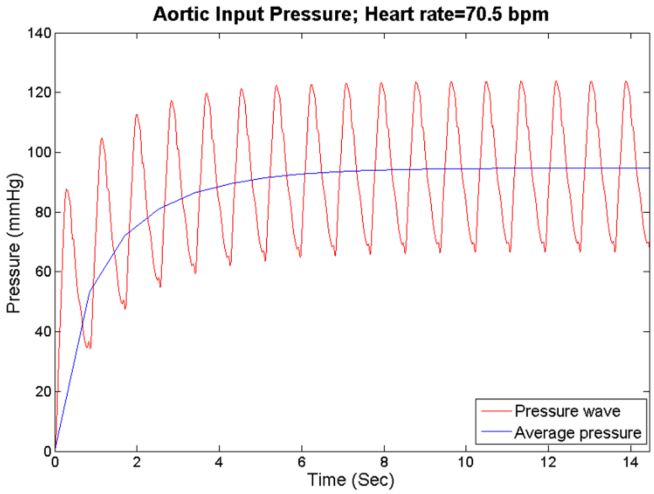

Figure 4.3. The mean pressure at the aortic input reaches a steady state for HR = 70.5 bpm

4.3.4 Power Calculation

The total power ($\bar{P}_{total}$) was calculated as the average of the product of the pressure (*p(t)*) and flow (*q(t)*) over a cardiac cycle. The steady power ($\bar{P}_s$) was the product of mean pressure (p_{mean}) and mean flow (q_{mean}), and the pulsatile power ($\bar{P}_{pulse}$) is the difference of the total power and steady power.

$$\bar{P}_{total} = \frac{1}{T}\int_0^T p(t)q(t)dt \ , \tag{4.9}$$

$$\bar{P}_s = p_{mean}q_{mean} \ , \tag{4.10}$$

$$\bar{P}_{pulse} = \bar{P}_{total} - \bar{P}_s \ . \tag{4.11}$$

4.4 Results

The simulations were run for seven different levels of aortic rigidities, ranging from a 30-year old healthy individual ($E_1(x)$) to a 70-year old sick individual suffering from aortic stiffening ($E_7(x)$) (values taken from Nichols *et al*)[7]. Here, $E_i(x)$ indicates that Young's modulus changes along the aorta, where x is the axial distance from aortic input. The different levels used were multiplicative factors of $E_1(x)$ (Table 4.1) as $E_2=1.25E_1$, $E_3=1.5E_1$, $E_4=1.75E_1$, $E_5=2E_1$, $E_6=2.5E_1$, and $E_7=3E_1$. Each case of the aortic rigidity was run for eight heart rates (70.5, 75, 89.5, 100, 120, 136.4, 150, and 187.5 beats per minute (bpm)). In all simulations, CO, PR, the terminal compliance, and the shape of the inflow wave were kept constant.

4.4.1 Pressure Wave Solution

To verify the model, the results were compared with well-known features of aortic pressure waves [7, 46]: (i) the pulse pressure amplification; (ii) the narrowing of the pressure waves as they travel down the aorta; (iii) the existence of a dicrotic notch; and (iv) the shifting of the second-highest pressure peak to the end of the cycle. Figure 4.4 shows that our computational model captured all four characteristics of the pressure wave. The model additionally captured another important physical feature of the blood flow—that the mean pressure decreased down the aorta (see Figure 4.4).

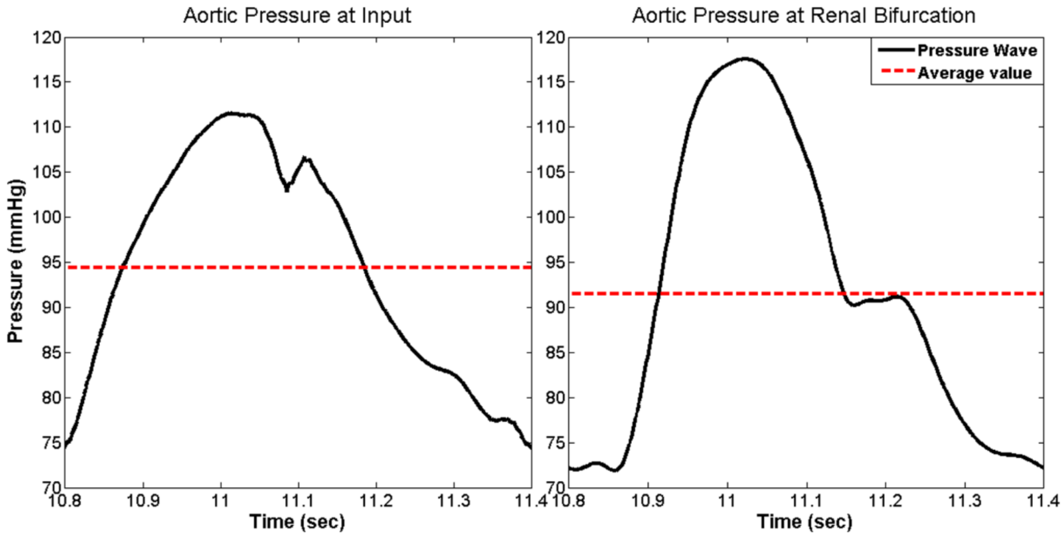
Aortic Pressure at Input

Aortic Pressure at Renal Bifurcation

Figure 4.4. Simulated results from our aortic model showing pulse pressure amplification, pressure narrowing, shifting of the second-highest peak, and the existence of the dicrotic notch. The average per cycle decreases due to viscous losses, consistent with realistic results. Data is for a 100 bpm heart rate and aortic rigidity of E_1 taken during one cycle after reaching steady state.

4.4.2 Effects of Aortic Compliance on Left Ventricular Power Requirement

Figure 4.5 shows average values per cycle for the total LV power requirement—external LV power ($\bar{P}_{total}$) —and the steady power ($\bar{P}_s$) versus aortic rigidity for an HR of 75 bpm. It shows that both $\bar{P}_{total}$ and $\bar{P}_s$, as well as the pulsatile power ($\bar{P}_{pulse} = \bar{P}_{total} - \bar{P}_s$), increased at higher rigidities. This is in agreement with clinical findings[78].

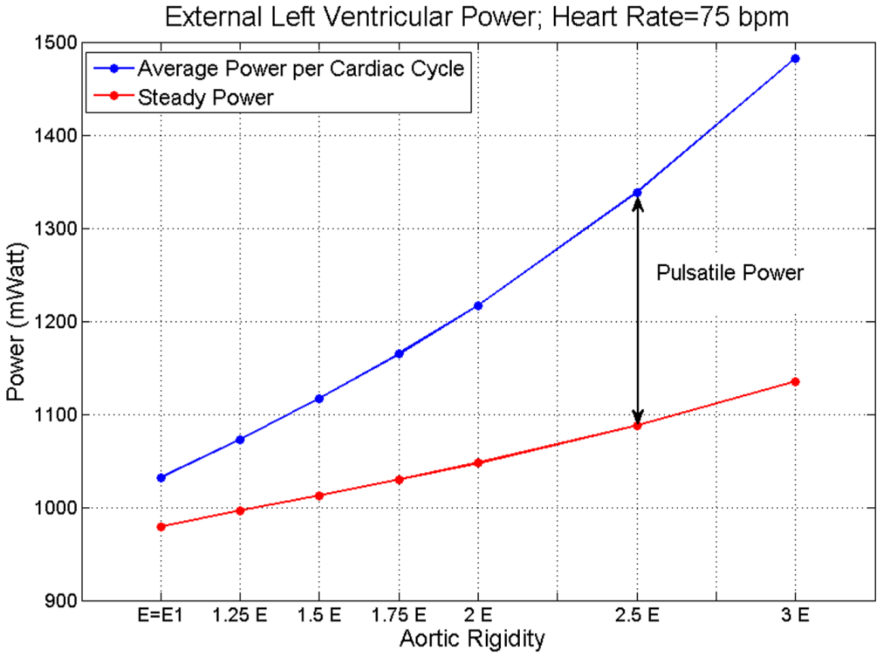

Figure 4.5. The blue line is average per cycle of the total external left ventricular power ($\bar{P}_{total}$) and the red line is the external steady power ($\bar{P}_{s}$) at different levels of aortic rigidities. The value of $E=E_1$ corresponds to the level of aortic rigidity given in Table 4.1. The difference between the two curves shown by the double arrow is pulsatile power ($\bar{P}_{pulse}$). The results are for HR = 75 bpm.

4.4.3 Effect of Heart Rate on Left Ventricular Power Requirement

Figure 4.6 shows $\bar{P}_{pulse}$ as a function of HR for three levels of aortic rigidity. As mentioned before, the cardiac output (average flow per cardiac cycle) is kept the same for all cases. As the HR increases, the $\bar{P}_{pulse}$ decreases until the HR reaches an optimum point where $\bar{P}_{pulse}$ is minimized (and as a result $\bar{P}_{total}$ is minimized). The $\bar{P}_{pulse}$ increases with HR beyond this optimum point. This phenomenon is present for all three cases. Interestingly, the optimum point shifted towards higher HR as aortic rigidity increased. In fact, as Figure 4.7 demonstrates, these phenomena still exist at very high rigidities, two- or three-fold greater than those of Figure 4.6.

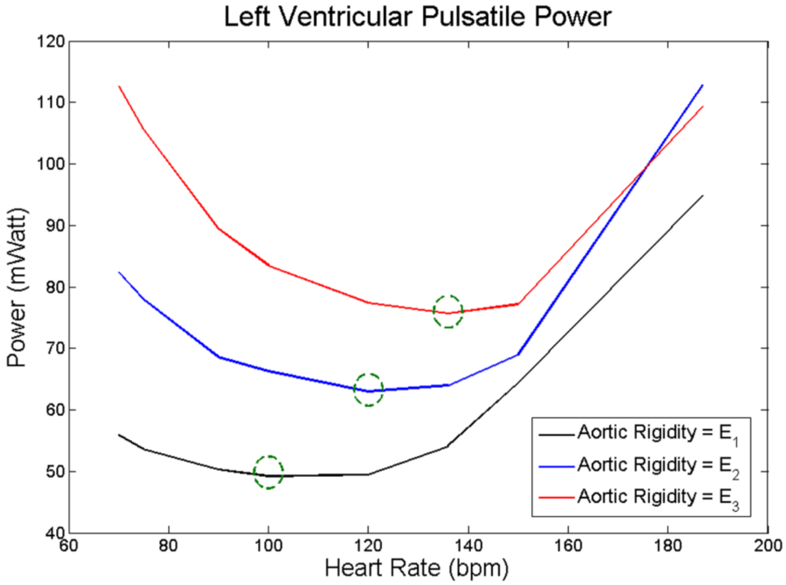

Figure 4.6. Average value per cycle of pulsatile power $\bar{P}_{pulse}$ versus HR for three different levels of aortic rigidities. E_1 (black) corresponds to the values given in Table 4.1, $E_2 = 1.25E_1$ (blue), and $E_3 = 1.5E_1$ (red). Green circles are the heart rates corresponding to the minimum $\bar{P}_{pulse}$ value at each level of aortic rigidity.

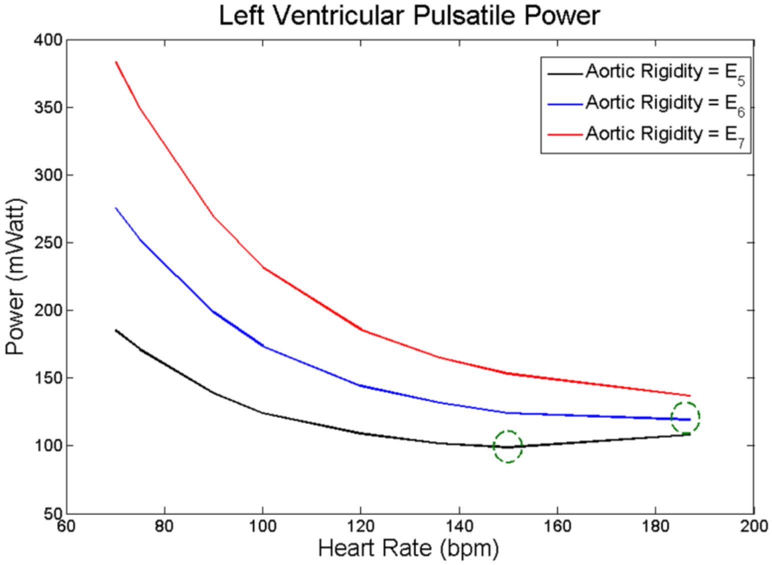

Figure 4.7. $\bar{P}_{pulse}$ versus HR for extreme values of aortic rigidity. $E_5=2E_1$ (black), $E_6 = 2.5E_1$ (blue), and $E_7=3E_1$ (red), where E_1 corresponds to the values given in Table 4.1. Green circles are the heart rates corresponding to the minimum $\bar{P}_{pulse}$ value at each level of aortic rigidity.

4.5 Discussion

The main findings of this chapter are as follows: (i) an increase in aortic rigidity leads to an increase in both the steady and pulsatile loads on LV; (ii) at higher aortic rigidities, the effect of pulsatile load becomes more dominant; (iii) at a given heart pumping condition (cardiac output and inlet flow wave), there is an optimum heart rate that minimizes the pulsatile LV power; and (iv) the optimum HR shifts to higher values as aortic rigidity increases.

Pulsatile load on the LV is the result of complex wave dynamics in the arterial network. As the largest and most compliant vessel extending from the heart, the aorta dominates the wave dynamics that the LV experiences. Although pulsatile load on the LV only accounts for a small portion of the total energy of the heart [58, 79], its adverse effect on the LV has been well accepted. Indeed, clinical studies have confirmed that abnormal pulsatile load plays an important role in the development of LVH and progression of LVH to CHF [37, 61, 63, 66]. Hence, aortic wave dynamics—as the determinant of LV pulsatile load—plays an important role in pathogenesis of LVH and CHF.

First, the effect of aortic wave dynamics on LV power requirements was investigated by changing aortic rigidity at a fixed HR(=75 bpm) while keeping constant all the other aortic wave dynamic determinants such as CO, shape of inflow wave, peripheral resistance, terminal compliance, and the locations of the reflection sites. Both steady power and pulsatile power increase at higher rigidities. The increase in pulsatile load is due to both reduced compliance and wave dynamics.

Second, for a fixed cardiac output (CO=4.6 *L/min*), the effect of aortic wave dynamics on the pulsatile LV power requirement across a physiological range of heart rates was studied. The results reveal that there is an optimum HR (within physiological range) at which pulsatile LV power requirement becomes a minimum, thereby confirming a prediction by O’Rourke [80].

The pulsatile power continues to decrease with increasing HR until it reaches its minimum point. Beyond the minimum point, the aortic waves start acting destructively, and as a result, the pulsatile power starts elevating with the HR (see Figures 4.6 and 4.7). The same pattern has been shown in an animal study performed by O'Rourke [65]. He studied the effect of HR on the ratio of the pulsatile to total LV power. In Figure 1 of his paper, he showed the pulsatile/total percentage versus HR for 3 dogs (dog 7, 9, and 32) where dog 32 showed the same pattern as in Figure 4.5 and it had an optimum HR of around 120 bpm; however, he did not explain the existence of this minimum point in the paper. Notice that "pulsatile" load versus HR was sketched in Figure 4.6 and 4.7. However, as Figure 4.8 shows, the shape of the graphs in Figures 4.6 and 4.7 will be preserved if one sketches the percentage of pulsatile load over total power versus HR.

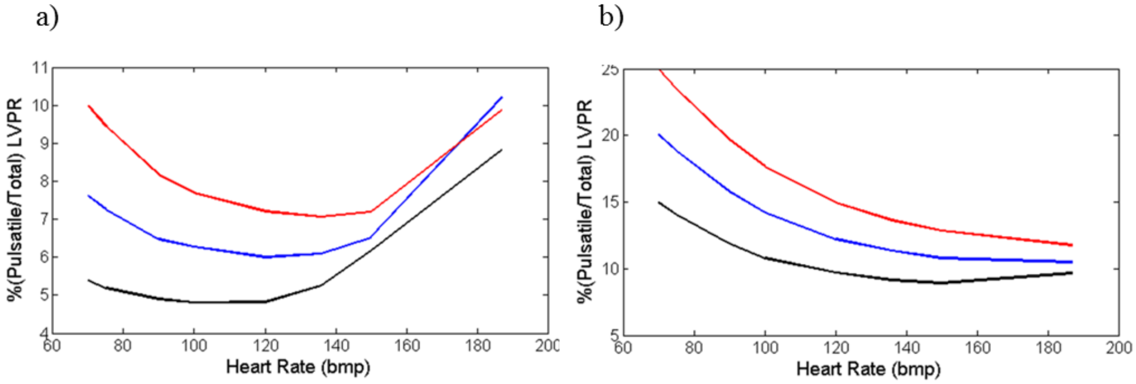

Figure 4.8. a) Percentage of $\bar{P}_{pulse}/\bar{P}_{total}$ versus HR for the cases given in Figure 6; E_1 (black) corresponds to the values given in Table 4.1, $E_2=1.25E_1$ (blue), and $E_3=1.5E_1$ (red). b) Percentage of $\bar{P}_{pulse}/\bar{P}_{total}$ versus HR for the cases given in Figure 4.7.

4.5.1 Clinical example: Smoking, Aortic Stiffness, and Heart rate

It has been shown in clinical studies that both aortic rigidity and HR are higher in habitual smokers compared to nonsmokers [66, 81-83]. It has also been shown that even smoking a single cigarette leads to a transient increase in pulse wave velocity (aortic rigidity), whether habitual or not [66, 84]. Hence in all cases the HR—even for habitual smokers whose HR level is generally higher—will increase during and immediately after smoking even one cigarette [85, 86]. It was shown that the optimum wave condition leads to a minimum pulsatile load at a specific HR. Hence, our results suggest a possible explanation for HR elevation in smoking. As aortic rigidity increases—such as from short-term or long-term smoking—the optimum wave condition shifts to a higher HR and therefore the heart increases the HR to reach the new optimum.

Some may argue that increasing HR as a compensatory mechanism for decreasing LV pulsatile load can have a metabolic disadvantage for the heart in terms of increased myocardial oxygen consumption and impaired ventricular-arterial coupling. However, it has been shown in previous studies that under normal conditions and in the absence of heart diseases (e,g. dilated cardiomyopathy), increased HR may even result in enhanced LV systolic and diastolic performance[87, 88]. Furthermore, under normal conditions, the LV-arterial coupling remains optimal after a moderate increase in HR [89].

4.5.2 Model Limitation

In this study, it was assumed that the heart acts as a flow source and hence specified the flow wave at the inlet. Although in general the heart is neither a flow nor a pressure source, the behavior of a normal heart is closer to a flow source [90]. In fact, in the case of a hypertrophied left ventricle (LVH condition), the heart acts completely as a flow source [90]. For a given metabolic condition, the body requires a certain flow rate and therefore it is reasonable to consider the heart as a flow source in this study.

Additionally, the aortic curve (arch) and the aortic branches were not included in our computational model (see Figure 4.1). However, the influences of branches in terms of wave reflection were included in the outflow boundary condition of the model (by assuming that the branches produce summated reflected waves). Exclusion of the arch can be justified by considering the fact that the curve has an insignificant effect on pressure waves[7].

4.6 Conclusion

The results of this computational study show that at a given heart's pumping condition, there is an optimum condition for aortic waves that minimizes the pulsatile load (and consequently total workload) on the heart. In addition, based on clinical observations, these results suggest that the heart may use this fact as a temporary compensatory mechanism to reduce myocardial workload. Therefore, controlling and modifying aortic wave dynamics—as the determinant of LV pulsatile load—can be a therapeutic approach for the reversal of LVH and the prevention of HF.

Chapter 5

A BIO-INSPIRED APPROACH FOR THE REDUCTION OF LEFT VENTRICULAR WORKLOAD

5.1 Chapter Abstract

Previous studies have demonstrated the existence of optimization criteria in the design and development of mammalians cardiovascular systems. Similarities in mammalian arterial wave reflection suggest there are certain design criteria for the optimization of arterial wave dynamics which stem from the existence of natural reflection sites such as renal and iliac branches. Inspired by these natural optimization criteria, the feasibility of optimizing the aortic waves by modifying wave reflection sites was investigated. A hydraulic model that has physical and dynamical properties similar to a human aorta and left ventricle was used for a series of in-vitro experiments. The results indicate that placing an artificial reflection site (a ring) at a specific location along the aorta may create a constructive wave dynamic that could reduce LV pulsatile workload. This simple bio-inspired approach may have important implications for the future of treatment strategies for diseased aorta.

5.2 Introduction

Congestive Heart Failure (CHF) is a condition in which the heart fails to circulate enough blood in the vascular networks. CHF has reached an epidemic level where the number of patients suffering from this condition in the U.S. alone is more than five million and growing[1]. Clinical investigations have confirmed that pulsatile load plays an important role in the pathogenesis of left ventricular hypertrophy (LVH) and the progression of LVH to CHF [34, 37, 90]. The pulsatile load is the result of the complex dynamics of wave propagation and reflection in compliant arterial vasculature [7, 12, 91].

Significant efforts have been made to understand the wave dynamics of the arterial system and to clarify its role in heart failure and other cardiovascular diseases [34, 37, 90, 92-94].

The pulsatile load on the left ventricle is controlled by the wave dynamics of arterial vasculature [7, 12]. Wave dynamics in a compliant tube is mainly dominated by three parameters: (1) fundamental frequency (or wavelength) of the waves; (2) wave speed (which is defined by material properties of the tube); and (3) the location of reflection sites [8, 9, 18]. Similarly, wave dynamics in the aorta and arterial network is determined by heart rate (HR), pulse wave velocity (PWV), and reflection sites. The interplay among these three parameters defines a wave dynamics condition where the pulsatile workload on the heart is minimized. Using a simplified computation model of the aorta it was shown the interplay among these wave dynamic parameters results in an optimum HR in which the pulsatile workload is minimized (see Chapter 4)[95]. There were several limitations involved with this computational study; therefore, it is necessary to confirm the finding using a physiologically relevant experimental model. The goal in this chapter is to introduce a bio-inspired approach to reduce the pulsatile workload. In this chapter, I also present validation of the finding of the previous computational study (the optimum HR concept in Chapter 4) using an in-vitro experimental approach.

Previous studies have demonstrated the existence of optimization criteria in design and development of mammalian cardiovascular systems [58, 79, 96-99]. Arterial wave dynamic parameters such as the reflection coefficient [100], normalized input impedance [101], and pulse wave velocity [58, 98], as well as the product of the propagation constant and the aortic length [100] are all invariant of mammalian size. These similarities in mammalian arterial wave reflection suggest there are certain design criteria for the optimization of arterial wave dynamics. Quick *et al* [102] showed that wave reflections are optimized in animals under normal physiological conditions. They also showed that either reducing or increasing wave reflections results in an elevation of LV pulsatile workload [102]. Their study suggests that the mammalian arterial system is designed to optimize the wave reflections rather than minimize them. Inspired by this natural optimization criterion, I will investigate in this chapter if it is possible to optimize the aortic waves by simply modifying reflection sites in order to reduce the pulsatile workload on the heart.

5.3 Materials and Methods

5.3.1 Equipment and Materials

An experimental hydraulic model called the aortic simulator was used in this study (Figure 5.1). The aortic simulator is a hydraulic model that has physical and dynamical properties similar to a human aorta and left ventricle which can be used for the *in-vitro* hemodynamic studies.

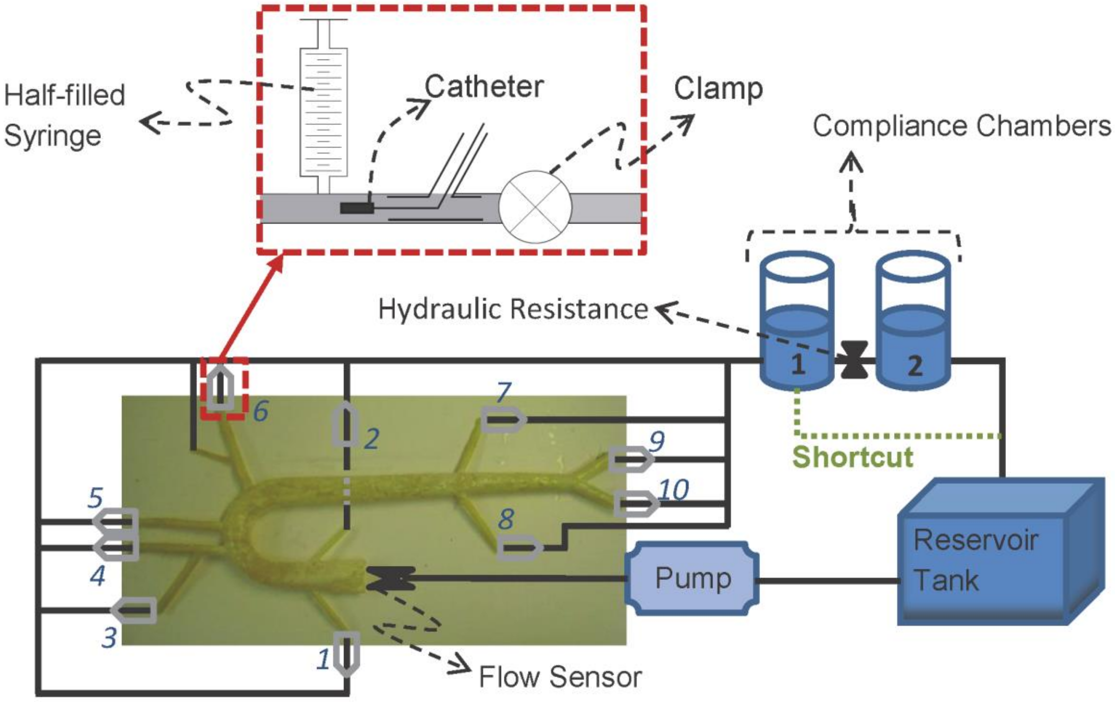

Figure 5.1: Schematic of the aortic simulator. Schematics of the outlet units are shown in the dashed-red box. The numbers at the outlets correspond to the value given in Table 5.1.

The left ventricle was simulated by a piston-in-cylinder pump (ViVitro Labs Inc. SuperPump System: Model SPS3891) that generates the pulsatile flow (using a programmed waveform generator WG5891) and sends it into a compliant aorta. The artificial aortas were built based on a 1-1 scale of a human aorta mold and it includes major branches of the aorta, aortic arch, and aortic tapering (Figure 5.1). Different compliant models of the artificial aorta were made from clear natural latex (Chemionics Corp.) and silicone (39 Shore A Hardness RTV Silicone). I made aortas with different compliances by changing the number of applications of dipping (for latex aortas) or coating (for silicone aortas). Different compliances resulted in different wave speeds (PWV). The foot-to-foot method [103] was applied to compute the PWV of each aorta (Table 5.1).

Table 5.1
Aortic pulse wave velocity (PWV)

Aorta No.	material	PWV (*m/s*)
1	*Silicone*	6.7
2	*Latex*	8.6
3	*Latex*	9.5
4	*Silicone*	11.4
5	*Latex*	13
6	*Latex*	13.5
7	*Latex*	15

A unit was designed for the end of each outlet that mimics the resistance and compliance of the eliminated vasculature. This unit includes one syringe, one clamp, and one port for catheter insertion (Figure 5.1). The syringe is half-filled with air which provides the required compliance of the eliminated vascular network (Table 5.2). The purpose of the clamp was to increase the terminal resistance. The aortic simulator also includes two compliance chambers, with hydraulic resistance in between, which were installed at the end of the aortic loop. These chambers enabled us to control the total volume compliance (the values are provides in Table 5.2). The reservoir tank is the last component of the aortic simulator. It connects the second chambers to the inlet of the pump (Figure 5.1).

Table 5.2
Volume compliance

Outlet location	air volume (*mL*)
Location 1 and 2	*6*
Location 3 and 6	12
Location 4 and 5	15
Location 7 and 8	15
Location 9 and 10	24
Cylindrical Chamber 1	1402
Cylindrical Chamber 2	1402

5.3.2 Measurements and Procedures

The pressure data was measured at the aortic input and outlet of the compliant aorta (outlet 9 in Figure 5.1) using Swan-Ganz catheters (Swan-Ganz 116F4 pediatric double lumen monitoring catheter at the inlet and Swan-Ganz 116F5 pediatric double lumen monitoring catheter at the outlet, Edwards Life Sciences) and Utah Medical Disposable pressure transducers (DPT-400). The signals were collected using the Tri-pack pressure measuring systems (TP8891, Vivitro Labs Inc.). The Tri-pack system consists of three bridge amplifiers. An H16XL Transonic flow sensor (Transonic Systems Inc.) in combination with a T110 Transonic Bypass flow meter was used to measure the volume flow rate at the inlet. The pressure and flow measurements have been done simultaneously. The pressure and flow data were collected for 4 seconds and each experiment was repeated at least five times.

Experiments were completed at various heart rates (ranging from 60 bpm to 200 bpm) with seven different aortas (see Table 5.1). In all experiments, water was used as the circulating fluid and any visible air bubbles were removed prior to the experiments. The pump was operating under 40% systole (waveform C, waveform generator WG5891) in all experiments. Three experimental setups were used in this study. These setups are as follows:

Setup 1: This setup is the same as the one shown in Figure 5.1. This setup included two compliance chambers and the resistance between the two.

Setup 2 (low volume compliance and low resistance setup): In this setup, the first chamber was shortcut to the tank (green dashed-line in Figure 5.1). Since the second chamber and the resistance between chambers were removed in this setup, the aortic simulator had lower total volume compliance and lower resistance compared to setup 1 (the mean pressure in setup 1 and setup 2 were 104.5±3.5 mmHg and 84±2 mmHg respectively).

Setup 3: This is the setup for the reflection site experiment. It is similar to setup 1. In this setup, an extra reflection site (a ring) was placed at different locations along the aorta (see Figure 5.2). This extra reflection site was used to alter the aortic wave reflection. The pressure and flow data were collected for 4 seconds and each experiment was repeated nine times.

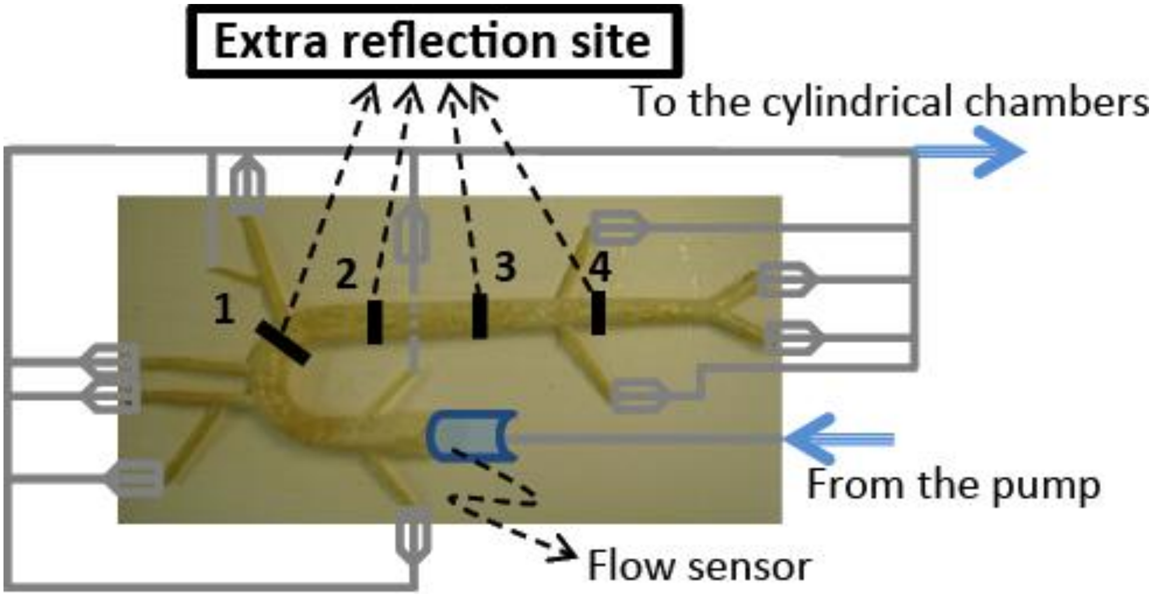

Figure 5.2: The aortic simulator for setup 3. An extra reflection site (a ring) was considered at different locations along the aorta marked by numbers 1-4. They are located at approximately 15, 25, 35 and 45 cm from the aortic input.

5.3.3 Power calculation

The pulsatile power was calculated using Equation 5.1:

$$\bar{P}_{pulse} = \underbrace{\frac{1}{T}\int_{0}^{T} p(t)q(t)dt}_{total\ power} - \underbrace{\frac{1}{T^2}\int_{0}^{T} p(t)dt \int_{0}^{T} q(t)dt}_{steady\ power} \ . \qquad (5.1)$$

Here, *T* is the period of the cardiac cycle, *p(t)* is the pressure, and *q(t)* is the flow.

5.4 Results

5.4.1 Effect of Heart Rate and Aortic Rigidity on Left Ventricular Pulsatile Workload

Sample measured flow and pressure waveforms from setup 1 and setup 2 are provided in Figure 5.3a and 5.3b respectively. Figure 5.4 demonstrates the effect of aortic rigidity and heart rate (HR) on input pulsatile power. Figure 5.4a shows the results of setup 2 that have lower total volume compliance and resistance compared to setup 1 (Figure 5.4b). These figures show that there is an optimum HR at each level of aortic rigidity in which pulsatile external power (pulsatile workload) is minimized. The optimum HR has a higher value in more rigid aortas (Figure 5.4a and 4.5b). These results are in agreement with the results of the computational study in Chapter 4 [95].

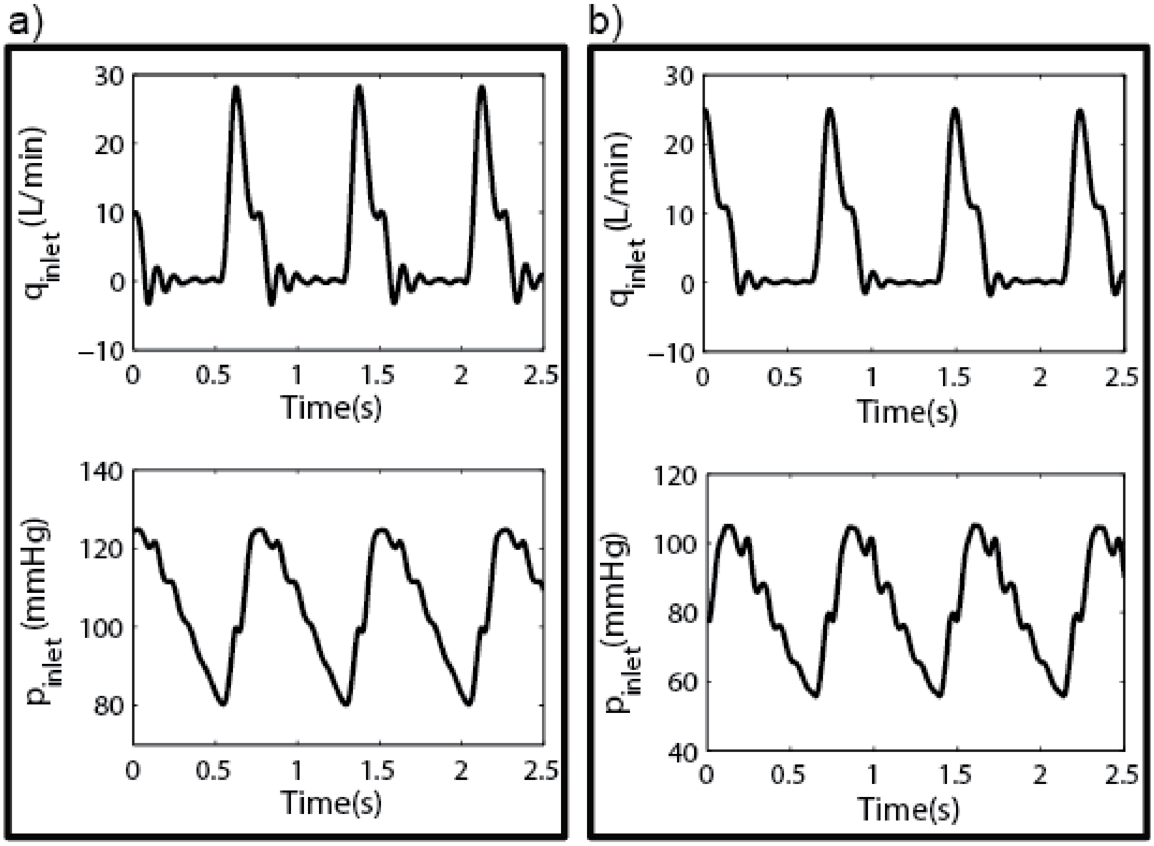

Figure 5.3: a) A sample of an aortic input flow wave (top) and a sample of the aortic input pressure wave (bottom) at HR= 80 bpm and CO=5 *L/min* for setup 1. b) A sample of an aortic input flow wave (top) and a sample of the aortic input pressure wave (bottom) at HR= 72 bpm and CO=5 *L/min* for setup 2.

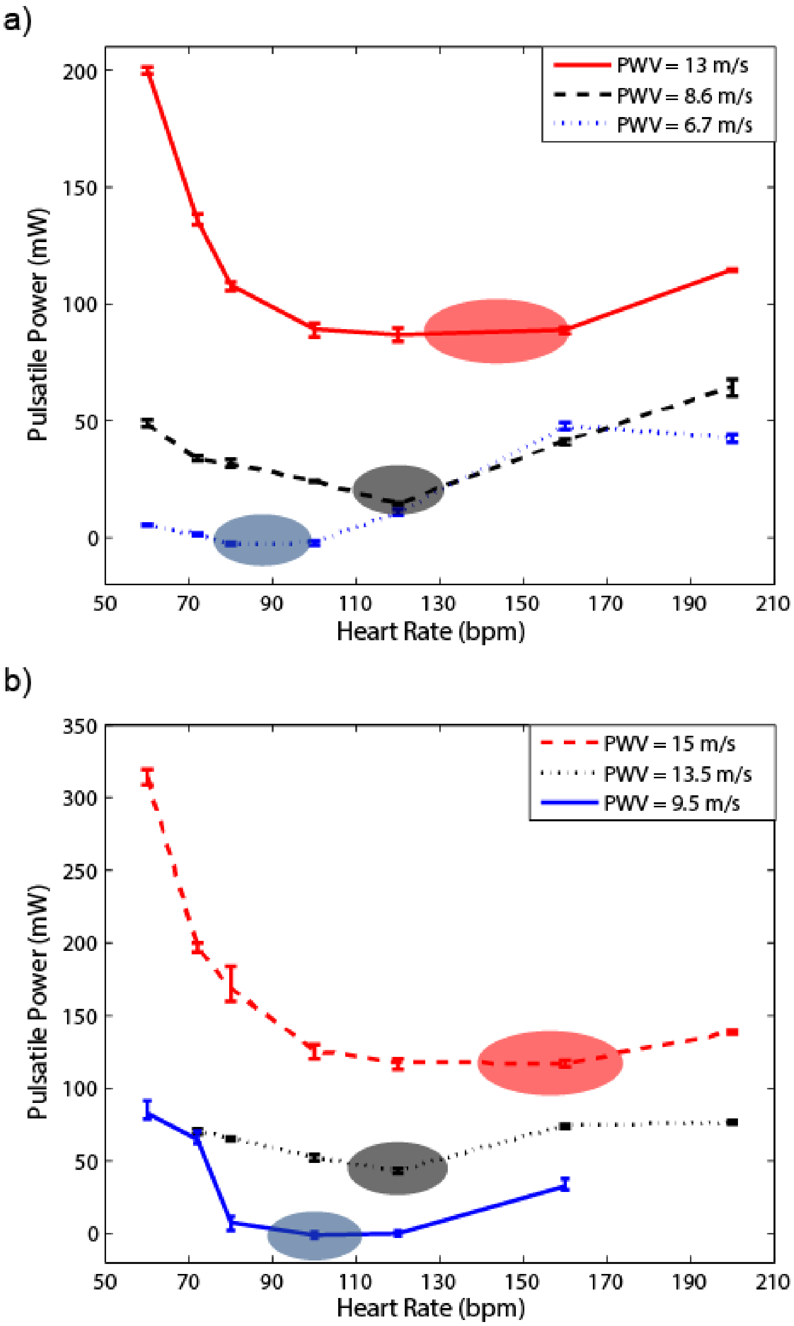

Figure 5.4: Pulsatile power versus heart rate (HR). a) Results of setup 2 (low resistance and low total volume compliance condition) for three different aortic rigidities; CO=5 *L/min* for all data points. b) Results of setup 1 for three different aortic rigidities; CO=5 *L/min* for all data points. There is an optimum HR in which pulsatile power is minimized. As the aortic rigidity increases, the optimum HR shifts to a higher value. Pulse wave velocity (PWV) is the wave speed and it is an index for aortic rigidity. Each power data point is the result of the respective experiment repeated five times.

5.4.2 Effect of Total Volume Compliance and Resistance on Optimum HR

Figure 5.5a and 5.5b show the effect of total volume compliance and peripheral resistance on the optimum value of HR for two aortas with different rigidities (PWV = 9.5 m/s and PWV=13 m/s). Although changing total resistance and total compliance alters mean and pulse pressure (as can be seen in Figure 5.3), the optimum wave condition (that results in optimum HR) does not depend on total volume compliance and total resistance as demonstrated in Figure 5.5. Due to the limitations of our pump, the experiments were performed at particular discrete heart rates. As a result, the exact optimum HR sometimes could not be identified.

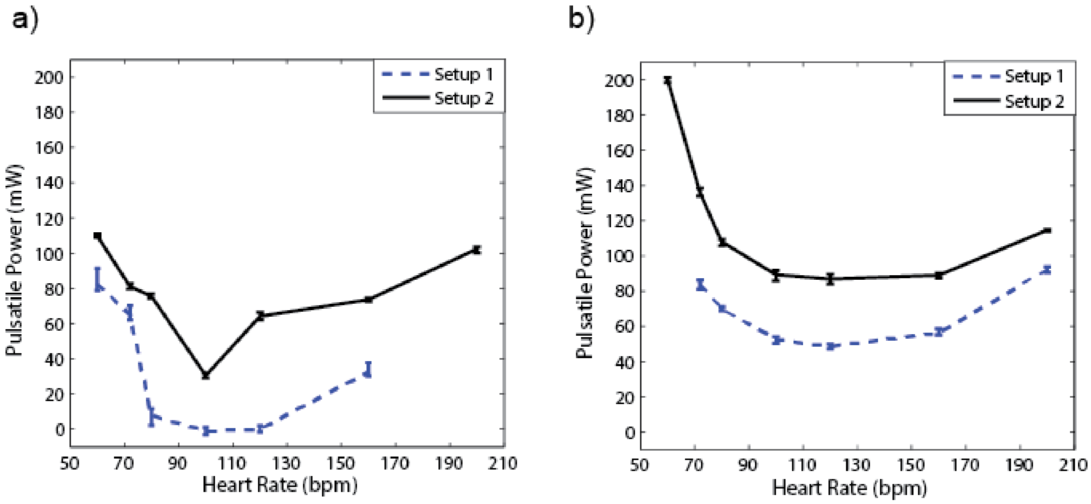

Figure 5.5: Effect of total volume compliance and peripheral resistance on optimum HR. a) Pulsatile power versus HR for the aorta with PWV = 9.5 m/s. b) Pulsatile power versus HR for the aorta with PWV=13 m/s. Changing total resistance and total compliance affect mean, pulse pressure, and pulsatile power; however, they do not alter the optimum HR (optimum wave condition). Each power data point is the result of the respective experiment repeated five times.

5.4.3 Bio-Inspired Approach: Optimizing the Location for Reflection Sites

As shown in previous sections, a specific combination of the three wave parameters (HR, PWV, and location of reflection site) creates a condition in which the LV pulsatile power is minimized. In this section, I tested the hypothesis that the reflection sites can be modified to improve the effect of wave reflection. Figure 5.6 demonstrates that placing an extra reflection site (a ring) at a particular location along the aorta could reduce the LV pulsatile power (workload). This has been shown for two different HRs in Figure 5.6a and 5.6b where it is clear that the pulsatile power can increase (destructive wave dynamics) or decrease (constructive wave dynamics) based on the location of the new reflection site.

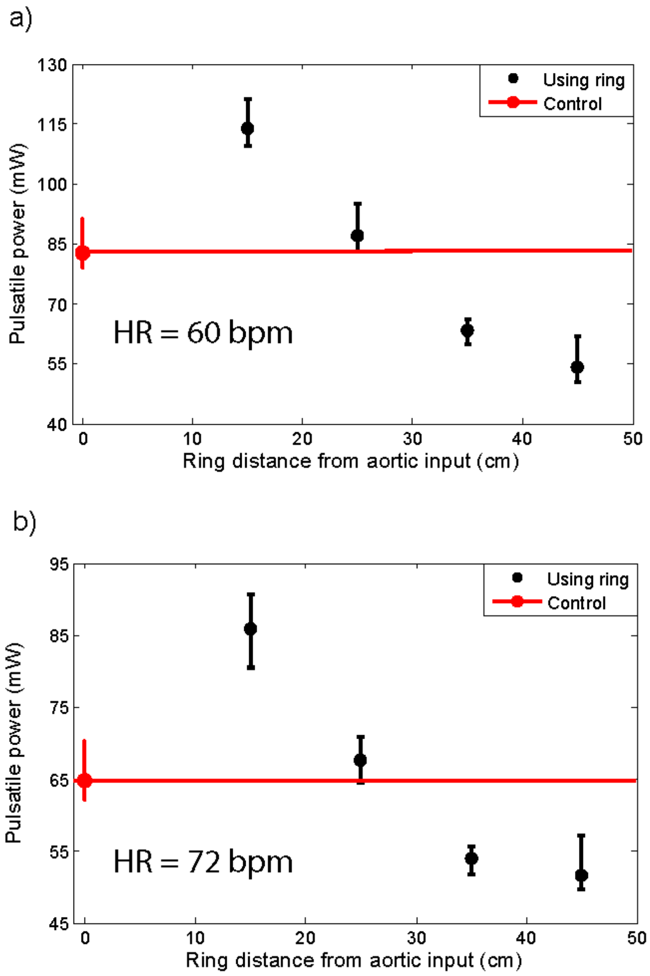

Figure 5.6: The effect of an extra reflection site created by a ring on input pulsatile power. a) Results are for aorta No.3 (see Table 5.1) with PWV=9.5 and HR=60 bpm. b) Results are for aorta No. 3 with PWV=9.5 and HR= 72 bpm. The control case is the aorta without an extra reflection site and the red line is the pulsatile power of the aorta without any rings (i.e. sans extra reflection sites). The pulsatile power can increase or decrease compared to the control case (control is the aorta without the ring), the nature of which depends on the location of the ring. Each data point is the result of the respective experiment repeated nine times.

5.5 Discussion

5.5.1 Optimum Heart Rate for Left Ventricle Pulsatile Workload

Using an experimental approach, it was shown in Figure 5.4a and 5.4b that there is an optimum HR at each stage of aortic rigidity in which the LV external pulsatile power (LV pulsatile workload) is minimized. This optimum HR shifts to higher values as aortic rigidity increases. It can be concluded that the interplay between HR and wave speed (which depends on the wall rigidity) changes the optimum point. These findings confirm earlier results that were obtained from the computational study in Chapter 4 [95].

The wave dynamics in a compliant tube is mainly dominated by the frequency of excitation (HR), the wave speed, and the reflection sites as shown in previous studies [8, 9, 18]. Similarly, aortic wave dynamics is controlled by the heart rate (HR), the pulse wave velocity (PWV), and the locations of the reflection sites. The optimum aortic wave condition depends on these interrelated parameters. Figure 5.5a and 5.5b show that parameters such as total volume compliance and total resistance do not affect the optimum HR value. In fact, the value of the optimum HR only depends on wave dynamic parameters such as PWV (wave speed) as demonstrated in Figure 5.4a and 5.4b. As expected, the pulsatile power-HR curves shift up when total compliance decreases (Figure 5.5a and 5.5b).

5.5.2 A Bio-Inspired Approach: Correction and Optimization of Aortic Waves

Traditionally, there was a misconception that wave reflections have only negative effects and that reducing the wave reflections is always beneficial. However, Zamir [104] proposed that wave reflections can in fact be beneficial and can even assist blood flow rather than impeding it. Not long after, Quick *et al* [102] showed that either increasing or decreasing wave reflection results in the elevation of pulsatile workload. Based on this observation, they have concluded that arterial wave dynamic is optimum under normal physiological conditions. This inspired me to investigate if it is possible to reduce LV pulsatile workload through the correction and optimization of aortic wave dynamics. Under healthy condition, this workload accounts only for 6-12% of the total LV workload [65]. However, the pulsatile workload significantly increases under vascular disease conditions [66].

Optimization of wave reflections as a therapeutic approach was first suggested by O'Rourke [80]. It was shown in this chapter that the introduction of properly positioned extra reflection sites in the aorta can result in a constructive wave dynamic state and a subsequent reduction of LV pulsatile workload. To test this idea, a ring (rigid reflection site) was placed at various locations along the aorta to alter the dynamics of wave reflection. Decreasing the pulsatile load in a heart failure patient is critically important [34, 37]. HF is usually accompanied by increased arterial stiffness. It is clinically impractical to increase the HR in order to reach a new optimum HR. Therefore our proposed “reflection site modification” method can potentially be used for reduction of the LV pulsatile workload for HF patients.

Figure 5.6a and 5.6b show that alteration of the wave reflection site can result in either an increase (a destructive effect) or decrease (a constructive effect) of the pulsatile power. The constructive and destructive effects of waves depend on the location of the ring (reflection site) since different locations cause different wave interactions. In other words, the phase of the global reflection coefficient varies with the location of the extra reflection site. To understand this phenomenon, consider that the pulsatile power can be written as a summation of the pressure and flow harmonics as [58]

$$\bar{P}_{pulse} = \frac{1}{2}\sum_{N=1}^{N} p_n q_n \cos(\beta_n - \varphi_n), \tag{5.2}$$

where p_n and q_n are the harmonic and phase of the pressure wave, respectively, and φ_n and β_n are the harmonic and phase of the flow, respectively.

The reflection coefficient (R) is defined as the ratio of the harmonics of the reflected pressure (p_n^r) to the harmonics of the forward pressure (p_n^f) in the frequency domain as [105]

$$R = |R|e^{i\theta^R}: \quad |R_n| = \frac{|p_n^r|}{|p_n^f|}\ , \theta_n^R = \varphi_n^f - \varphi_n^r\ . \tag{5.3}$$

It can also be written in terms of the impedances as [105]

$$R = \frac{Z_{in} - Z_0}{Z_{in} + Z_0}\ , \tag{5.4}$$

where Z_{in} is the input impedance, Z_0 is the characteristic impedance, and "$\beta - \varphi$" is the phase of the input impedance (θ^{in}) of the system. Therefore, $\cos(\beta - \varphi)$ can be computed as

$$\cos(\beta - \varphi) = \cos\theta^{in} = \frac{\Re[Z_{in}]}{|Z_{in}|}\ , \tag{5.5}$$

where, $\Re$ is the symbol denoting the real part of a complex function. Solving Equation 5.4 for Z_{in} gives

$$Z_{in} = Z_0\frac{1+R}{1-R}\ , \tag{5.6}$$

when combined with Equation 5.4 and 5.5, it gives

$$\cos(\beta - \varphi) = \frac{\Re\left[Z_0\frac{1+R}{1-R}\right]}{\left|Z_0\frac{1+R}{1-R}\right|}\ . \tag{5.7}$$

In the case of an aorta where viscoelastic properties are negligible, the characteristic impedance is real (it has a negligible imaginary part [102]). Hence, in this condition, Equation 5.7 can be simplified as

$$\cos(\beta - \varphi) = \frac{\Re\left[\frac{1+R}{1-R}\right]}{\left|\frac{1+R}{1-R}\right|} \,. \tag{5.8}$$

Using the impedance definition, the ratio of flow and pressure are related as

$$|p_n| = |q_n|\left|Z_n^{in}\right| \,. \tag{5.9}$$

Finally, substituting Equation 5.8 and Equation 5.9 into Equation 5.2, noting the relations $\left|Z_{in}\right| = \left|Z_0 \, \frac{1+R}{1-R}\right|$ and $R = |R|e^{i\theta^R}$ results in

$$\bar{P}_{pulse}^{n} = \frac{1}{2} q_n Z_0 \Re\left[\frac{1 + |R_n| e^{i\theta_n^R}}{1 - |R_n| e^{i\theta_n^R}}\right] , \tag{5.10}$$

where, for simplicity, only one harmonic of the series representation for pulsatile power has been shown. To find the condition where an increase in reflection will result in a decrease of the input pulsatile power, the function $(R_n, \theta_n) = \Re\left[\frac{1+|R_n|e^{i\theta_n^R}}{1-|R_n|e^{i\theta_n^R}}\right] = \frac{1-|R|^2}{1+|R|^2-2|R|\cos\theta}$, was considered (for simplicity, $R_n = R$ and $\theta_n^R = \theta$). The region where $\frac{\partial G}{\partial |R|} < 0$ corresponds to the range of $|R|$ and θ where pulsatile power is decreasing while wave reflection is increasing. This region depends on both the magnitude of the wave reflection ($|R|$) and its phase (θ), and is described as

$$\frac{\partial G}{\partial |R|} = \frac{2\cos\theta |R|^2 - 4|R| + 2\cos\theta}{(1 + |R|^2 - 2|R|\cos\theta)^2} < 0 \xrightarrow{yields} \boxed{2\cos\theta |R|^2 - 4|R| + 2\cos\theta < 0} \,. \tag{5.11}$$

Obviously for any value of $|R|$, this condition is satisfied if $\frac{\pi}{2} < \theta < \frac{3\pi}{2}$ since $\cos\theta < 0$ and $|R| > 0$. This means that increasing the wave reflection causes a decrease in pulsatile power when the phase falls in the second or third quadrant. In the first and fourth quadrants (where $0 < \theta < \frac{\pi}{2}$ and $\frac{3\pi}{2} < \theta < 2\pi$ respectively), increasing the wave reflection can increase or decrease (depending on the magnitude and phase) the input pulsatile power. This is illustrated in Figure 5.7, the grey area denoting the range of $|R|$ and θ where pulsatile power decreases by the act of increasing the wave reflection. Similar analyses have been done by Quick *et al* [102]. However, our contour for the boundary between the two regions has a teardrop shape, whereas the one presented by Quick *et al* is circular [102].

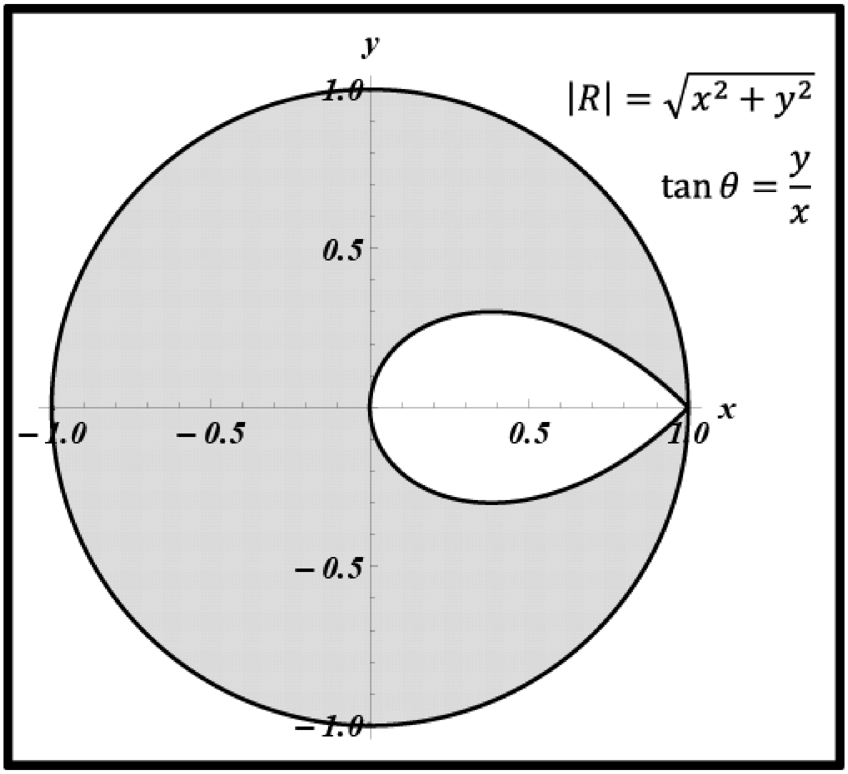

Figure 5.7: The grey area is the region where increasing wave reflection is beneficial. In this region, increasing wave reflection results in a decrease of the input pulsatile power ($|R| \uparrow \Rightarrow \bar{P}_{pulse} \downarrow$). In the white region, increasing wave reflection is disadvantageous and results in an elevation of the pulsatile power ($|R| \uparrow \Rightarrow \bar{P}_{pulse} \uparrow$).

The above analysis can be used to explain the observed phenomena in Figure 5.6a and 5.6b. In my experiments, when the ring was located at Position 1 (15 cm from the input, see Figure 5.2) the operation point of the system was in a state similar to the white area (Figure 5.7); hence, increasing the wave reflection increased the pulsatile power. At Position 2 (25 cm from the input), the system is found to be in the boundary between the two regions of Figure 5.7 where the pulsatile power does not change significantly with the increased reflection. For Positions 3 and 4, the system lies in the operational region similar to the gray area where increasing wave reflection results in a decrease of pulsatile power. Under this beneficial wave condition, an extra reflection site reduces the input pulsatile power as shown in Figure 5.6a and 5.6b.

5.5.3 Limitation

The major limitation of this study is related to the fact that an in-vitro model of the systemic arterial system was considered. In fact, the dynamics of the LV-arterial system in a true physiological situation may be slightly different from our *in-vitro* experimental model. This means that the optimum HR and optimum ring location in our model may not be exactly the same as the in-vivo situation. Another limitation of this study is related to oversimplification of microvasculature in our model; however, this simplification does not change the main finding of this study since microvasculature does not influence the aortic wave dynamics. The microvascular network only contributes as a discrete reflection site and as a resistance to blood flow, and both of these effects are properly modeled in our *in-vitro* experimental setup. In addition, water as a circulatory fluid was used in this study, but this does not affect the results since the fluid viscosity plays a negligible role in the dynamics of aortic waves[7, 12].

5.6 Conclusion

Using an *in-vitro* experimental approach I have validated my finding in the computational study of Chapter 4. It has been found in this chapter that there is an optimum heart rate at which the pulsatile workload on the left ventricle is minimized. The optimum heart rate shifts to a higher value as the aortic rigidity increases.

A simple bio-inspired concept, based on the principles of wave dynamics, was also introduced to improve the LV workload in heart failure patients. A device based on this concept could be in the form of a ring or a band wrapped around the aorta to act as an extra reflection site that alters wave reflection. This device can be designed to be minimally invasive due to its lack of complexity. However, the effectiveness of such a device is yet to be determined and is the subject of future work.

Chapter 6

A WAVE DYNAMICS CRITERION FOR OPTIMIZATION OF MAMMALIAN CARDIOVASCULAR SYSTEM

6.1 Chapter Abstract

The cardiovascular system in mammals follows various optimization criteria covering the heart, the vascular network, and the coupling of the two. Through a simple dimensional analysis I arrived at a non-dimensional number (wave condition number) that can predict the optimum wave state in which the left ventricular (LV) pulsatile power (LV workload) is minimized in a mammalian cardiovascular system. This number is also universal among all mammals, independent of animal size, maintaining a value of 0.1. By utilizing a unique *in-vitro* model of human aorta, I tested my hypothesis against a wide range of aortic rigidity. It was concluded that the optimum value of the wave condition number remains approximately 0.1 for a wide range of aorta rigidities that I could simulate in our *in-vitro* system.

6.2 Introduction

The cardiovascular system in mammals benefits from various optimization criteria covering the heart, the vascular network, and the coupling of the two [58, 79, 96-99]. The heart's pumping characteristics and vascular network properties of mammals are either scaled with allometric parameters or some invariants of the animal size [79, 100, 106-108]. Parameters such as the pulse wave velocity [58, 98], reflection coefficient [100], the product of the propagation constant and the aortic length [100], mean blood velocity in the ascending aorta [107], the product of heart rate and arterial decay time [101], as well as the normalized input impedance [101] are all invariant of mammalian size. These functional and other geometric similarities indicate that there are optimization principles for the heart operations and arterial system functions, as well as for the subsequent coupling of the two.

Many previous studies have attempted to identify these optimization criteria [58, 79, 96-99]. Among these studies, Taylor reported that the nonuniform distensibility of the arterial system in mammals results in reduction of cardiac work [97]. Milnor looked at the aortic input impedance of mammals of different sizes, and proposed that the heart rate (HR) is fast enough to avoid the high impedance at low frequencies and slow enough to allow normal relaxation and recovery of the heart [98]. Elzinga and Westerhof proposed that the heart and arterial systems should have a minimum size, and that the range of the resting HR is selected only to maintain the required diastolic pressure[79]. They used in-vivo experimental approaches to show that the left ventricle operates close to the optimum power point and the optimum efficiency. Although their hypothesis can explain the existence of a higher HR in a small animal, it falls short of explaining the slow HR found in a large animal (for details see Elzinga and Westerhof [79]). The above-mentioned shortcomings indicate that there might be other missing optimization criteria in the selection of the optimum HR.

It is a well-known fact that the pulsatile load on left ventricle (LV) is determined by the dynamics of wave propagation and reflection in compliant arterial vasculature [7, 12]. Wave dynamics in a compliant tube is mainly controlled by three parameters: (1) fundamental frequency of the propagating waves; (2) material properties of the tube (which define the wave speed); and (3) reflection sites [8, 9, 18]. Therefore, it is reasonable to assume that the adult cardiovascular system is designed in such a way as to take advantage of this complex wave dynamics. The main objective of this chapter is to develop a better understanding of wave dynamics and its role in the aforementioned optimization process.

I have hypothesized that the interplay between the heart rate (HR), the location of the total reflection site, and the pulse wave velocity (PWV—the clinical term for wave speed) can create an optimum wave condition in which pulsatile workload (or power) is minimized. It is shown in this chapter that the optimization of this condition is a design criterion in the natural selection of the heart rate in mammals.

6.2.1 Wave condition number

I start the analysis by idealizing the aorta as a simple elastic tube. Although it is a complex phenomenon, wave dynamics in a compliant tube is dominated by the fundamental frequency of the excitation, the wave speed, and the locations of the reflection sites [8, 9, 18]. Therefore, it is reasonable to assume that wave dynamics in the aorta is controlled by the heart rate (HR), the pulse wave velocity (PWV) and an *effective length* (L_{eff}). There are numerous reflections sites in the vascular network, but they create a cumulative reflected wave. From the perspective of the heart, the summated waves appear to be reflected from a single reflection site called the total (effective) reflection site. The distance of the total reflection site from the aortic input is called the *effective length* (L_{eff}) [109]. The value of L_{eff} is close to the length of the aorta under normal physiological conditions [109]. In this chapter, I propose a non-dimensional number called the wave condition number denoted by the symbol "α". This dimensionless number is a function of HR, PWV, and L_{eff} and can be derived as follows:

$$\alpha = k(HR)^a(PWV)^b(L_{eff})^c\,, (k \text{ is a constant}). \qquad (6.1)$$

The dimensions for each component are $HR = [T^{-1}]$, $PWV = [LT^{-1}]$, and $L_{eff} = [L]$, where L is the dimension of length and T is the dimension of time. In terms of dimensions, Equation 6.1 can be rewritten as:

$$\alpha = k[T^{-a}][L^{b}T^{-b}][L^{c}]. \tag{6.2}$$

To balance dimensions, one requires that

$$\begin{cases} a = -b \\ c = -b \end{cases}. \tag{6.3}$$

The choice of b is arbitrary, so, without loss of generality, we can set $b=-1$; hence, $a=1$ and $c=1$. The constant k can also be absorbed into α and hence eliminated explicitly from Equation 6.1. Therefore α is related to the wave dynamic parameters as

$$\alpha = \frac{(HR)(L_{eff})}{(PWV)}. \tag{6.4}$$

6.3 Materials and Methods

6.3.1 Equipment and Materials

An *in-vitro* experimental approach was employed to test the hypotheses. Experiments were performed using a hydraulic circuit called an aortic simulator (Figure. 6.1). This hydraulic circuit has physical and dynamical properties similar to a human heart and aorta and is suitable for the *in-vitro* hemodynamic study of the vascular system. The major components of the aortic simulator include a positive displacement piston pump connected to an artificial aorta. Details of all the other aortic simulator components are provided below.

A piston-in-cylinder pump (ViVitro Labs Inc. SuperPump System: Model SPS3891) was used to generate the pulsatile flow and simulate the left ventricle (using a programmed waveform generator WG5891). The artificial model included the aortic arch and main branches of the aorta (see Figure 6.1) and was built on a 1-1 scale of the human aorta. These aortas were made out of clear natural latex (Chemionics Corp.) by dipping method, and silicone (39 Shore A Hardness RTV Silicone) by coating method. By changing the number of applications of dipping or coating, I made aortas with different rigidities. Thus I was able to test different compliant models of the artificial aorta that were then used in order to get different wave speeds (PWV). The PWV of each aorta is provided in Table 6.1, computed by the foot-to-foot method [103].

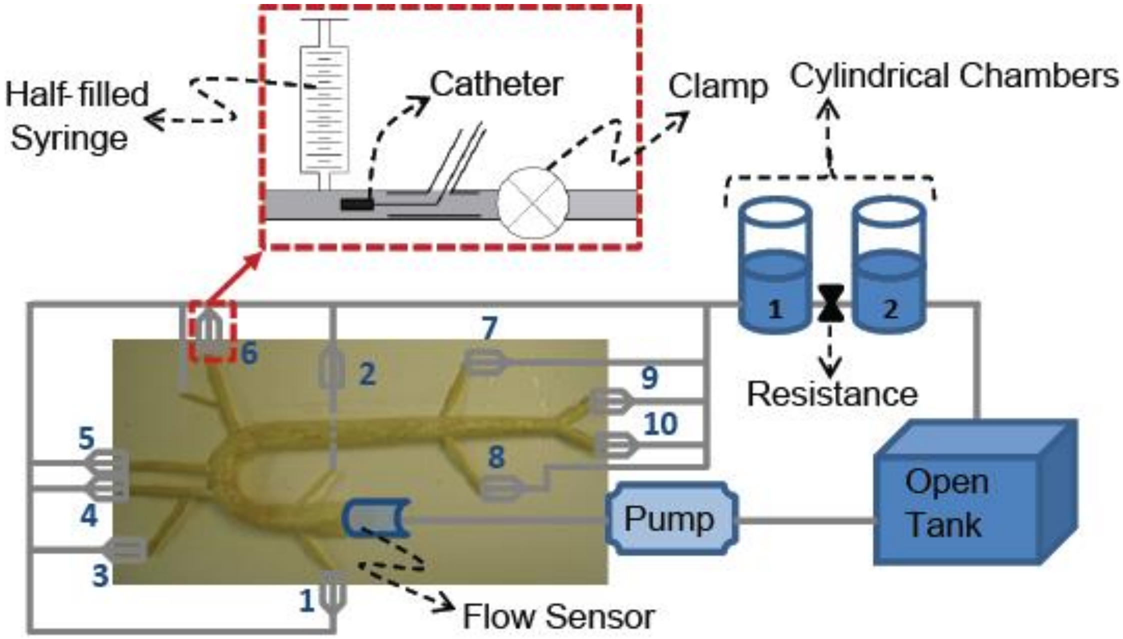

Figure 6.1: Schematic representation of the aortic simulator. There is a unit at each outlet that gives the compliance and resistance of the eliminated vasculature. Schematics of these units are shown in the dashed-red box. The numbers at the outlets correspond to the value given in Table 6.1.

Table 6.1
Pulse wave velocity (PWV) of aortas

No.	material	PWV (*m/s*)
1	*Silicone*	6.7
2	*Latex*	8.6
3	*Latex*	9.5
4	*Silicone*	11.4
5	*Latex*	13
6	*Latex*	13.5
7	*Latex*	15

A unit was attached to the end of each outlet in order to simulate the resistance and compliance of the eliminated arterial network. This unit has three parts: one syringe, one clamp, and one port for catheter insertion (see Figure 6.1). The syringe is half-filled with air to simulate the required compliance of the eliminated vasculature (Table 6.2). In my experiments, the resistance from connecting tubes was high enough to give the physiological mean pressure; however, a clamp could also have been used to increase the terminal resistance. Two half-filled cylindrical chambers were installed at the end of the aortic loop which enabled me to control the total volume compliance (Table 6.2). The two chambers were connected to each other with a hydraulic resistance in between. The last component of our hydraulic loop was a reservoir tank connected to the inlet of the pump. Figure 6.1 shows the schematics of the aortic simulator as well as a sample artificial aorta used in this study.

Table 6.2
Air volume compliance

aortic outlet location*	air volume (*mL*)
Location 1 and 2	*6*
Location 3 and 6	12
Location 4 and 5	15
Location 7 and 8	15
Location 9 and 10	24
Cylindrical Chamber 1	1402
Cylindrical Chamber 2	1402

(*See Figure 6.1 for aortic output locations)

The pressure data was measured at the aortic input (Swan-Ganz 116F4 pediatric double lumen monitoring catheter, Edwards Life Sciences) and measured at the outlet of the compliant aorta at the iliac artery location (Swan-Ganz 116F5 pediatric double lumen monitoring catheter, Edwards Life Sciences) using Utah Medical Disposable pressure transducers (DPT-400). Tri-pack pressure measuring systems TP8891 (Vivitro Labs Inc.) consisting of three bridge amplifiers were used to collect the signals. Volume flow rates were measured at the inlet using a T110 Transonic Bypass flow meter and a H16XL Transonic flow sensor (Transonic Systems Inc.). The pressure and flow data were collected simultaneously.

6.3.2 Procedures

In the aortic simulator, water was used as the circulating fluid. (Note that since the focus of this study is wave dynamics, the effect of fluid viscosity is negligible.) Any visible air bubbles were removed. In all experiments, the pump was operating under 40% systole (waveform C, waveform generator WG5891). Three sets of experiments were completed at various heart rates (ranging from 60 bpm to 200 bpm) with different aortas. These experimental sets are as follows:

Set 1: The experimental setup as shown in Figure 6.1 This setup included both cylindrical chambers and the resistance between the two. The pressure and flow data was collected for 4 seconds and each experiment was repeated at least five times.

Set 2: In this setup, the first chamber was directly connected to the tank and therefore carried a compliance that was lower than Set 1. The resistance was also lower than Set 1 due to the removal of the hydraulic resistance and the shortcutting of the circuit (mean pressure was 84±2 mmHg for Set 2 and 104.5±3.5 mmHg for Set 1). By the shortcutting of the first chamber to the tank, I reduced total volume compliance while still maintaining a constant aortic PWV for each individual aorta. The data was collected for 4 seconds and each experiment was repeated at least five times.

6.3.3 Power Calculation

The pulsatile power is the result of the wave dynamics in a compliant vessel, which can be calculated using

$$\bar{P}_{pulse} = \frac{1}{T}\int_{0}^{T} p(t)q(t)dt - \frac{1}{T^2}\int_{0}^{T} p(t)dt \int_{0}^{T} q(t)dt\ . \tag{6.5}$$

Here, T is the period of the cardiac cycle, *p(t)* is the pressure, and *q(t)* is the flow. Note that in Equation 6.5, the first term is the total power and the second term is the steady power.

6.4 Results

6.4.1 Wave Condition Number and Mammalian Size

The arterial wave dynamics and pressure wave characteristics are similar in all mammals [58, 101, 107] and, therefore, optimum wave reflection should also be similar in all mammals. This means that the optimum wave condition number is the same in all mammals. Although mammals have different HR and they exist at different length scales, the PWV is almost the same across all mammals [98, 110]. Hence, the value of wave condition number (α) was investigated by looking into published data with mammals at different sizes where PWV is constant but L_{eff} and HR are not. Since the L_{eff} is approximately the same as the aortic length (± 10% in healthy humans) [109], the available aortic lengths (L_{Aorta}) of mammals were used for the calculation of α. Figure 6.2 demonstrates the value of α at different L_{Aorta}. The HR and L_{Aorta} values of Figure 6.2 are given in Table 6.3 (values are taken from [98, 106, 107, 110]). This figure demonstrates that α is around 0.1 across a wide range of mammalian size.

6.4.2 Wave Condition Number and Pulsatile Power

In the previous section, it was shown that the wave condition number is universal among all mammals independent of animal size, maintaining an approximate value of 0.1. In this section, through an in-vitro simulation of the human aorta (see Materials and Methods section), it will be shown that the wave condition number of 0.1 signifies an optimum condition where a certain combination of HR and PWV minimizes the input pulsatile power. Figures 6.3a and 6.3b show samples of a flow wave and a pressure wave in the inlet respectively.

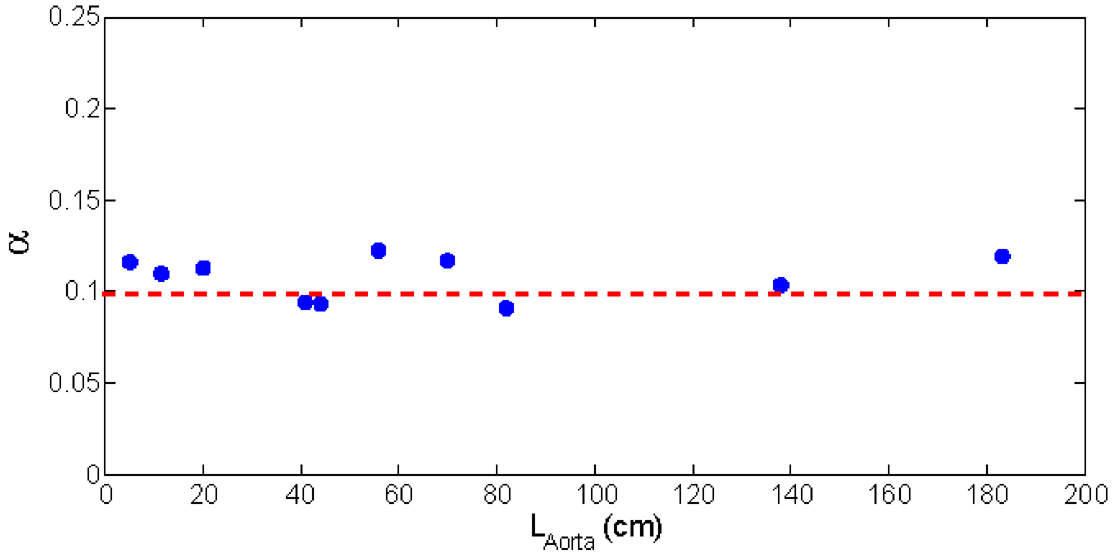

Figure 6.2: Wave condition numbers for mammals with different aortic lengths. The value is 0.1 (with absolute deviation of 0.01) across a large range of aortic lengths. Details of the animal cases used are provided in Table 6.3.

Table 6.3
Mammalian data of Figure 6.2

physical parameters	*HR (bpm)*	L_{Aorta} *(cm)*	α
Mouse	835*	5†	0.116
Rat	346‡	11.5‡	0.110
European Rabbit	205§	20¶	0.113
Dog	83†	41†	0.094
Human	76‡	44‡	0.093
Goat	79 †	56†	0.122
Wild Boar (Sus Scrofa)	60§	70¶	0.117
Lion (Panthera Leo)	60§	82¶	0.091
Bactrian Camel	27§	138¶	0.103
Indian Elephant	23.5*	183¶	0.119

(*Data are taken from Adolph [106]. †Data are taken from Holt *et al* [107]. ‡Data are taken from Milnor [98]. §Data are taken from Altman *et al* [110]. ¶Data were calculated from Holt *et al* allometric equation $L_{Aorta}=16.12\ BW^{0.32}$ where BW is body weight [107]. Wave speed (PWV) was 6 m/sec for α calculation [98].)

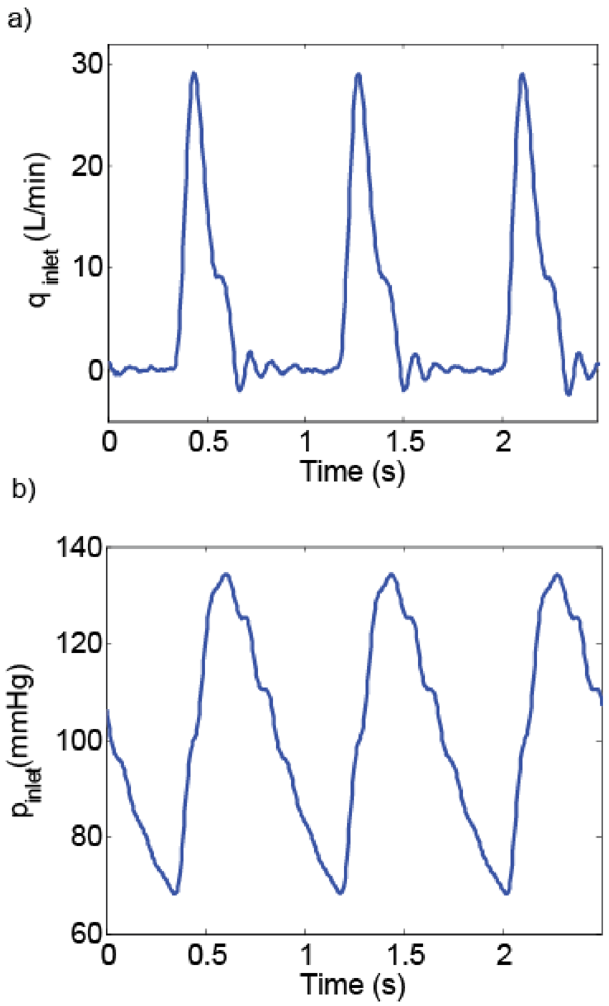

Figure 6.3: a) A sample of an aortic input flow wave at HR= 72 bpm and CO=5 *L/min*. b) A sample of the aortic input pressure wave at HR= 72 bpm and CO=5 *L/min*.

The wave condition number ($\alpha = \frac{HR.L_{eff}}{PWV}$) was calculated at each PWV (*m/s*) and HR (*Hz*). In our experimental setup, the effective length L_{eff} (= 0.56 *m*) is the distance from the aortic input to the end of the compliant aorta where it is connected to the rigid tubes (see Figure 6.1). Graphs of pulsatile power versus the wave condition number (α) are shown in Figure 6.4a and 4b for seven and five different aortas, respectively. These aortas have different rigidities and hence different PWVs. Figure 6.4 shows that the optimum wave condition number has a value around 0.1 for all cases independent of aortic rigidity and experimental setup. Figure 4a and 4b belong to the setups with higher total volume compliance and lower total volume compliance, respectively (see Materials and Methods section for details). Due to the limitations of the pump, the experiments were performed at particular discrete heart rates and, therefore, the exact α_{opt} sometimes could not be identified. Besides this, a few values seemed to deviate (however slightly) from the exact value of $\alpha_{opt} = 0.1$. These experiments were performed under two different setups where total volume compliance and total resistances varied (see Materials and Methods section). Although changing total resistance and total compliance alters mean and pulse pressure, the optimum value of the wave condition number remained at $\alpha_{opt} \approx 0.1$ in all experiments.

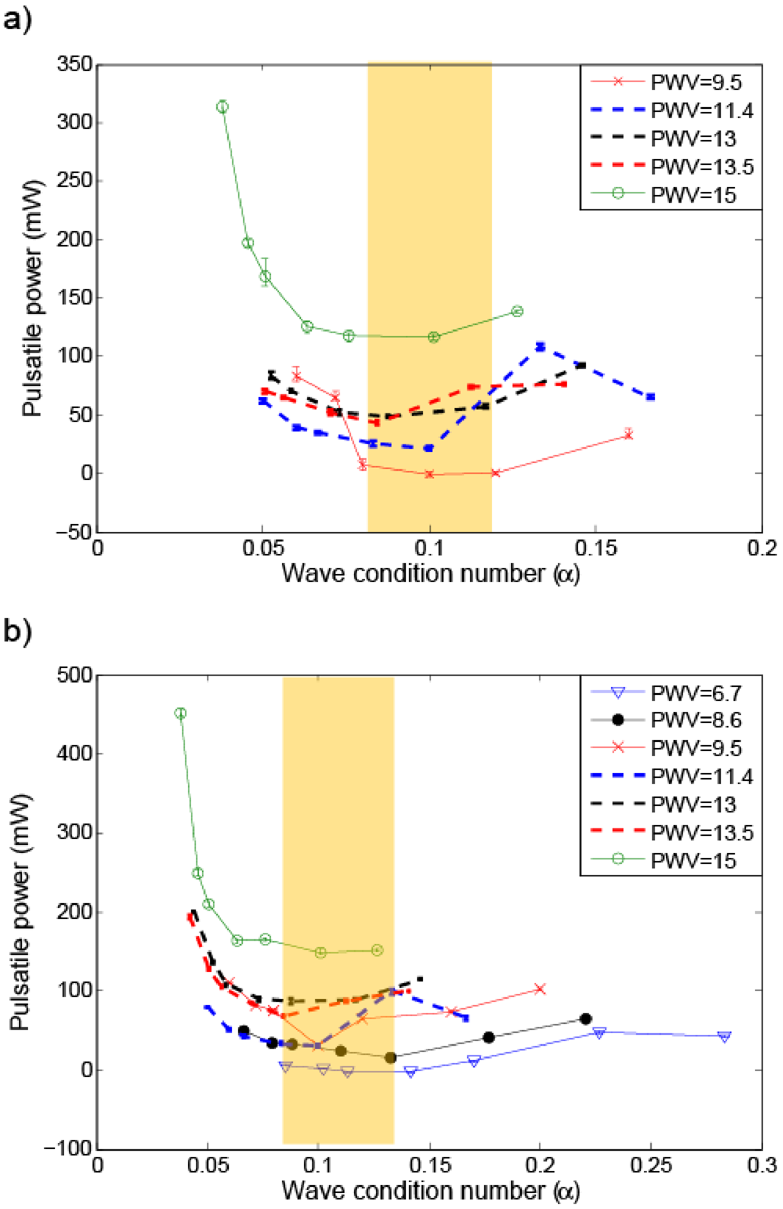

Figure 6.4: Pulsatile power versus wave condition number “α” at different PWVs. a) Results of the aortic hydraulic model in setup with higher total volume compliance (Set 1). b) Results of the aortic hydraulic model in setup with lower total volume compliance (Set 2). The yellow band shows the range of optimum wave condition numbers. It is clear that α_{opt} values scatter around 0.1 for all cases. Note that since the experiments were performed at specific discrete heart rates allowed by our pump, the exact α_{opt} could not be identified and some values seem to deviate (however slightly) from the exact value of $\alpha = 0.1$. Each data point is the result of the respective experiment repeated five times.

6.5 Discussion

I have demonstrated the existence of a non-dimensional number (wave condition number) that can predict the optimum wave state in which the left ventricular (LV) pulsatile power (workload) is minimized in a mammalian cardiovascular system. I have also shown the following: (i) the optimum value of the wave condition number is around 0.1, and it is universal among all mammals independent of their size (their aortic length); (ii) the optimum value of the wave condition number remains the same (0.1) at various levels of aortic rigidity.

6.5.1 Natural Selection of Optimum Heart Rate in Mammals: Wave Optimization Perspective

Arterial wave dynamics are similar in mammals due to functional and geometric similarities in mammalian cardiovascular systems as demonstrated in previous studies [98, 100, 101, 106-108, 111]. It was shown in Figure 6.2 that the wave condition number equals 0.1 in mammals of all sizes ranging from a mouse to an elephant. Larger species will have a larger effective length (aortic length). However, since the pulse wave velocity (PWV) is the same in all mammals regardless of size, the HR must decrease to retain the optimum wave condition. Allometric equations L_{aorta}, *HR*, and *PWV* as functions of animal body weight W also indicate that the optimum wave condition number is invariant of the mammalian size: $L_{aorta} = 16.12\, W^{0.32},\ HR = 3.6\, W^{-0.27}$, and *PWV=6 m/sec* (invariant of animal size) $\Longrightarrow$ $\boxed{\alpha = 0.097W^{0.05}}$.

Here, L_{aorta} is in centimeters (*cm*), W is the animal body weight in kilograms (*kg*), and HR is the heart rate in hertz (*Hz*). The allometric equation of L_{aorta} is taken from Holt *et al* [107] and allometric equation for HR is taken from Adolph [106]. It is necessary to emphasize that retaining the optimum wave condition is only one of several design parameters that optimize the mammalian cardiovascular system. However, there are a very few mammals, such as the guinea pig, whose arterial wave dynamics are different from all other mammals [112], and hence might have a slight deviation from 0.1 in the wave condition number.

Existence of such an optimum state can also be attributed to the possibility of the aorta acting as a passive pump. It has been shown that compliant tubes at certain excitation frequencies, tube compliances, and reflection sites can act as pumps and the process is known as a *Liebau* effect [8, 9, 13, 91]. This will be investigated in the next chapter (Chapter 7).

As described in this chapter, a specific combination of the *HR*, *PWV*, and L_{eff} creates optimum wave dynamics (optimum in the sense that pulsatile power is minimized) where $\alpha_{opt} = 0.1 = \frac{HR.L_{eff}}{PWV}$. In the case of mammals of different sizes where the PWV is the same, a larger animal requires a decrease in HR in order to maintain the optimum condition of $0.1 = \frac{HR\downarrow .L_{eff}\uparrow}{PWV}$f. In the case of smoking, where L_{eff} does not change but aortic rigidity does (higher PWV), the HR increases (see Chapter 4) to retain the optimum value of $0.1 = \frac{HR\uparrow .L_{eff}}{PWV\uparrow}$. Inspired by this finding, a therapeutic approach can be envisioned to reduce the LV pulsatile load by correcting and optimizing wave dynamics as first proposed by O'Rourke [80]. The majority of HF patients show increased arterial stiffness ($PWV \uparrow$)[7, 66]. For these patients, our results suggest that their natural HR should be elevated based on the stiffness of their aorta. Since it is rarely practical to increase the HR in HF patients, one solution would be to modify wave reflection sites (e.g. increasing L_{eff}).

6.6 Conclusion

The results of this chapter suggest that aortic wave optimization is one of the design characteristics of the mammalian cardiovascular system. This is in agreement with the earlier result shown by Quick *et al* [102]. The wave optimization was considered with respect to the pulsatile workload. However, perfusion of coronary arteries is also an important aspect of aortic wave optimization [92, [104, 113, 114], making this an important subject of future studies. A non-dimensional number dubbed the wave condition number (α) was introduced and was shown to have the value of $\alpha_{opt} = 0.1$ at the optimum wave state. This relationship was demonstrated to be universal among all mammals (from mice to elephants). However, this is not the only factor that defines HR in mammals; there are certainly other factors, as shown in previous studies [79, 96-98, 115]. Amazingly, mammalian cardiovascular systems have evolved in such a way as to satisfy them all. I have thus propose using the wave condition number as a scaled cardiovascular risk index. This index could be useful as a new diagnostic tool in the development of new therapeutic strategies.

Chapter 7

WAVE PUMPING EFFECT IN THE HUMAN AORTA

7.1 Chapter Abstract

An impedance pump—also known as Liebau pump—is a simple valveless pump that operates based on the principles of wave propagation and reflection. It has been shown in embryonic zebrafish that a similar mechanism is responsible for the pumping action in the embryonic heart during the early stages before valve formation. Recent studies suggest that the cardiovascular system is designed to take advantage of wave propagation and reflection phenomena in the arterial network. In this chapter I report the results of an *in-vitro* study that examines the hypothesis that the adult human aorta acts as a passive pump based on Liebau effect. A hydraulic model with different compliant models of an artificial aorta was used for a series of in-vitro experiments. The results indicate that wave propagation and reflection can result in a pumping mechanism in a compliant aorta.

7.2 Introduction

At the early stages of vertebrate embryonic life, the heart is a simple valveless tubular vessel that creates a pumping action and sends the blood into the embryo's body. In a zebrafish embryo model, Forouhar *et al*. have shown that this tubular valveless pump works like an impedance pump [20]. An impedance pump—also known as Liebau pump—is a simple valveless pump that works based on wave propagation and reflections. Liebau was the first one who suggested the potential existence of a wave pumping mechanism (now known as an impedance pump) in the human aorta [13, 17].

In its simplest form, an impedance pump requires a compliant tube element bounded by two stiffer tube elements (reflection sites) at its two ends and a wave generator (e.g. a pincher). The generated waves propagate toward the reflection sites. If there is any asymmetric wave condition (i.e. distance to reflection site or wave speed) the wave interaction process will generate a net flow from one end to the other [8, 9, 13]. The net flow and its direction depend on various parameters such as the frequency of pincher excitation (fundamental frequency of waves), the pincher location (distance to the reflection sites), the tube compliance (wave speed), and pincher stroke (wave amplitude)[8-11, 13, 19].

The impedance pump mechanism—which will be referred to as the wave pumping mechanism in this chapter—is responsible for blood circulation in the early embryonic stage before the formation of valves. In the embryonic heart tube, the role of the pincher is played by a band of active contractile cells near the heart tube's entrance [20]. Ultimately, the formation of the mature heart and aorta is the result of the embryonic heart tube's morphing and segmentation during development. Once the mature cardiovascular system is formed, the heart generates waves which propagate in the compliant aorta and which could give rise to a pumping effect similar to an impedance pump. This effect may play a subtle but important role in vertebrate circulatory system. Figure 7.1 shows the schematic of an impedance pump, an embryonic heart tube, and mature heart-aorta system. The goal in this chapter is to investigate if the aorta could act as a conduit for wave reflection and propagation, and the resulting wave pumping effect, therefore, offering the heart a supplementary pumping mechanism that will help to reduce its load.

The aorta assists blood circulation if it generates net flow in forward direction (aorta forward pumping condition). In this case, the measured cardiac output (CO) is the sum of the flow generated by the heart (q_1) and the net flow generated by the wave pumping effect (q_2) in the aorta. However, from a system point of view, what the heart actually feels is quite different. The heart sees the aorta and the vascular network as a resistance composed of passive and dynamic impedance against the flow of blood. Hence, under the aorta forward pumping condition, the heart feels reduced impedance (resistance) which results in reduced pulsatile workload of the heart. Similar to an impedance pump, a backward pumping effect may reduce the net flow. Under the backward pumping condition the heart feels elevated impedance due to generated reverse net flow, so the left ventricular power requirement increases. The measured CO in this condition is the difference between the reverse flow generated by positive displacement of the heart and the net flow created by wave pumping in the aorta ($\mathrm{CO} = q_1 - q_2$). The outcome is different under the heart failure (HF) condition, but the mechanism is still the same. In HF, CO decreases since the failed heart cannot generate enough power to overcome the reverse pumping in the aorta. If the aorta generates net flow in the forward direction, the heart feels reduced impedance and CO increases. Figure 7.2 shows a schematic of the above-mentioned phenomena.

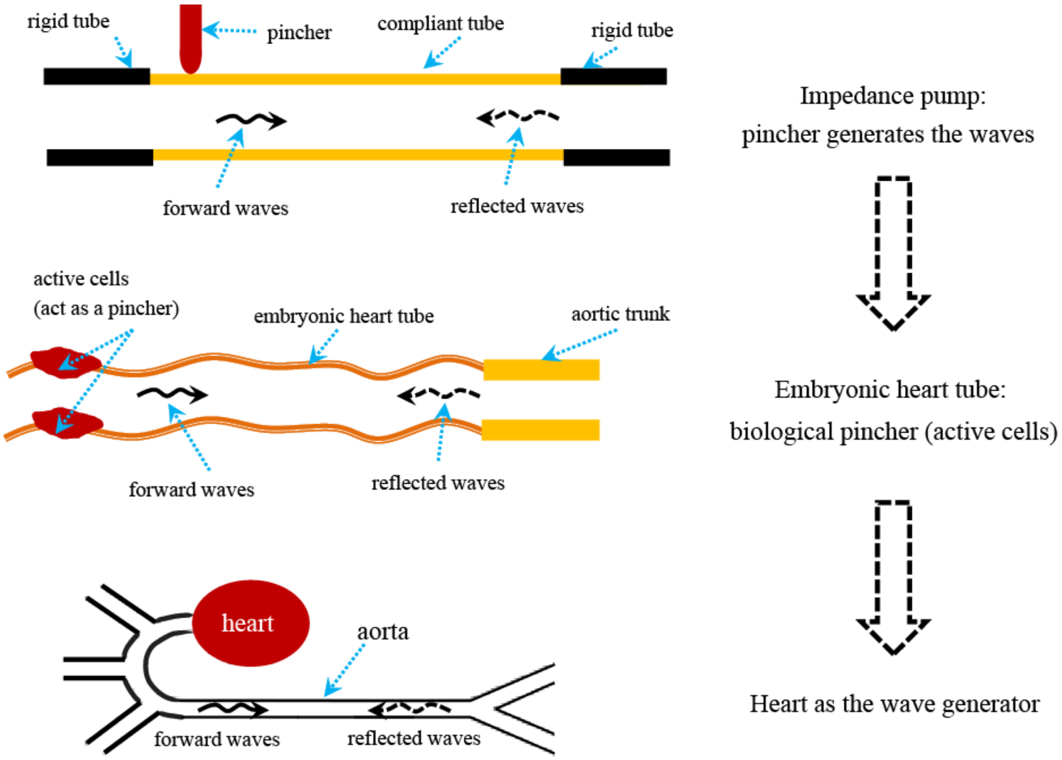

Figure 7.1: A schematic of an impedance pump where a pincher generates the waves [9], an embryonic heart tube where active cells function as a biological pincher [20], and a heart-aorta system where waves are generated by the heart.

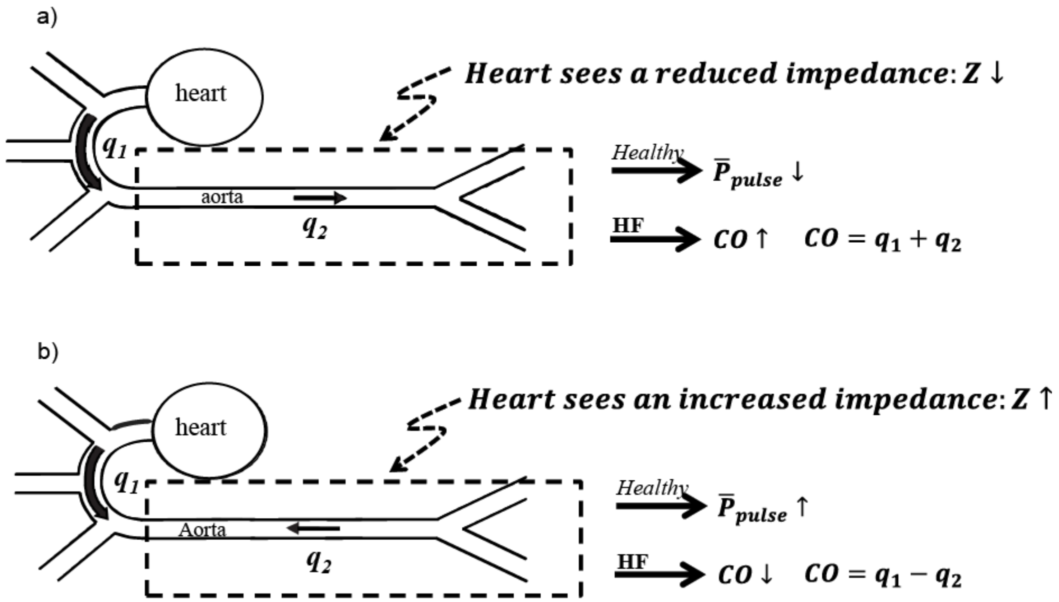

Figure 7.2: A schematic of the impedance pumping phenomenon. The aorta may pump in a forward or backward direction depending on the wave dynamics inside the aorta. a) The aorta is pumping in the forward direction. b) The aorta is pumping in the reverse direction. The heart sees these pumping effects as reduced or increased impedance (Z) which shows up as reduced or increased pulsatile power ($\bar{P}_{pulse}$) respectively. Under the heart failure (HF) condition, the aorta forward pumping effect ($+q_2$) facilitates the blood circulation by increasing the cardiac output (CO). On the other hand, the aorta backward pumping effect ($-q_2$) results in reduced CO since the failed heart cannot overcome the extra load.

The hypothesis is that wave dynamics can in fact create a pumping effect in the aorta similar to an impedance pump such as that found in an embryonic zebrafish heart. The difference between an aortic pump and a classical impedance pump is that there is no external pincher; instead, the waves are being created by the heart. The main goal in this chapter is to show how wave reflection in the aorta can create net flow in forward direction (toward the capillaries) or backward direction (toward the heart). The direction of the net flow and its magnitude depends on the wave dynamic characteristics. I used an *in-vitro* heart-aorta model to test this hypothesis since it would be extremely difficult if not possible to show this effect *in-vivo*.

As shown in Figure 7.2, the aorta pumping effect can be mistaken for increased or reduced impedance. In order to show that aortic waves create a pumping effect, I designed an experimental setup in which the net flow generated by positive displacement of the heart ($q_1 = 0$) was removed, but waves were preserved. In this experiment, the time averaged (per cycle) measured flow (q_2) is caused by the passive pumping created by waves in the aorta (see Figure 7.3).

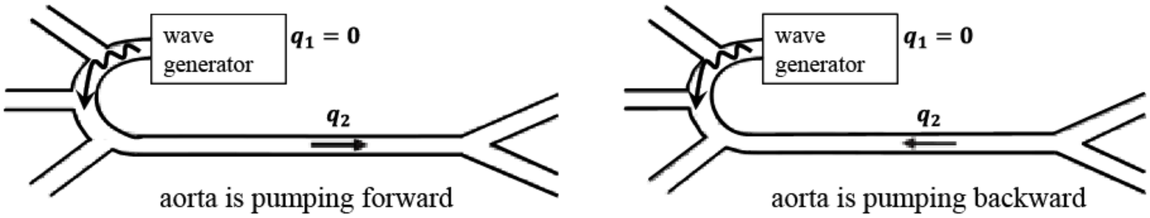

Figure 7.3: Schematic representation of an ideal setup for testing the hypothesis. If the net flow generated by the heart is eliminated ($q_1 = 0$), the measured flow will be the net flow generated by the wave pumping effect in the aorta (measured flow $=q_2$). $q_2 > 0$ and $q_2 < 0$ correspond to the aorta forward pumping and aorta backward pumping conditions respectively.

7.3 Methods

To test the hypothesis, an *in-vitro* experimental approach was considered. The schematic of the experimental setup is shown in Figure 7.4. The setup includes a piston pump connected to a T-junction. An artificial aorta is connected to one side of the T-junction from one end and to rigid tubing from the other end which connects to a reservoir tank. The other side of the T-junction is connected to a rigid tube that is directly connected to the tank.

In order to reveal the contribution of the wave pumping effect the one-way valves have been removed from the piston pump to simulate a heart with zero net flow and enable the generation of waves in the compliant aorta. A small net flow however was unavoidable due to the asymmetric resistance of the flow loop on either side of the pump.

Therefore, in this experimental setup, there are two pumping mechanisms: 1-asymmetric pumping (asymmetric resistance pumping) and 2-wave pumping (impedance pump). Therefore, it is necessary to have control experiments (Setups 2 and 3) to show that the observed pumping is not caused entirely by asymmetric pumping but by waves as well. The asymmetric pumping can happen in both rigid and compliant tubes, and it does not need a medium for wave propagation. The basic mechanism for this pumping mechanism is the asymmetric pressure or kinetic energy loss at both sides of the T-junction. (Further details about this pumping mechanism can be found in the literature [116, 117]). The focus in this study is on the wave pumping mechanism that works based on the wave dynamics phenomena in compliant tubes.

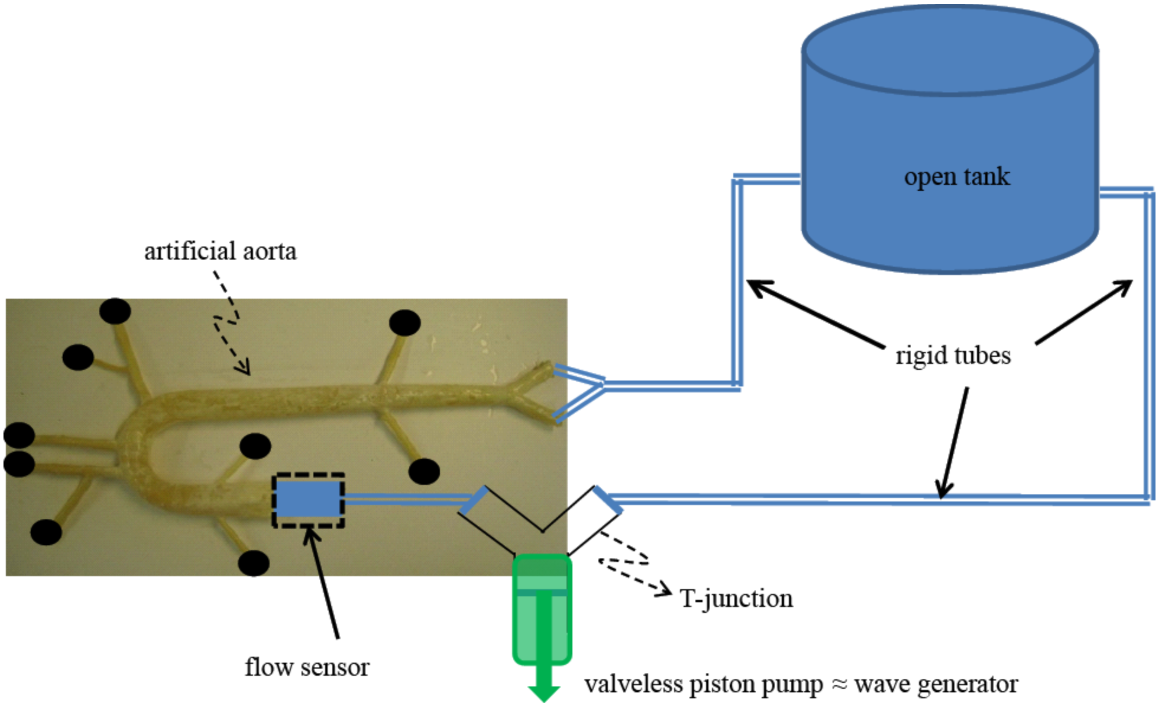

Figure 7.4: Schematic of the experimental setup. The setup includes a valveless piston pump, a T-junction, an artificial aorta, an open surface reservoir (tank), an ultrasonic flow-meter sensor, and rigid tubing.

7.3.1 Equipment and Materials

The piston pump is a piston-in-cylinder pump (ViVitro Labs Inc. SuperPump System: Model SPS3891) that generates the pulsatile flow using a programmed waveform generator (Vivitro WG5891). The artificial aortas were built on a 1-1 scale of the human aorta. These aortas were made out of clear natural latex (Chemionics Corp.) by dipping process. Different compliances were obtained by using the same mold and changing the number of dips in the dipping process. The rigid tubes were Masterkleer PVC tubes with an inner diameter of ¾” and a thickness of ¼”. Due to the flow sensor requirement, a rigid Tygon tube (R-3603) with an inner diameter of ¾” and a thickness of 1/8” was placed at small section right before the aortic inlet where the flow sensor was positioned. A T110 Transonic bypass flow meter and a H16XL Transonic flow sensor (Transonic System Inc.) were used for volume flow rates measurement at the inlet (see Figure 7.4).

7.3.2 Procedures

In these experiments, water was used as the circulating fluid. Any visible air bubbles were removed. In all experiments presented in this chapter, the pump was operating under 30% systole (duty cycle=30%) (waveform A, waveform generator WG5891). Three experimental setups were considered, which are as follows:

Setup 1: This experimental setup is shown in Figure 7.2. The aorta model length is 56 cm and the total length of the aortic side is 203 cm. The total length of the rigid side (the side that directly connects the pump to the tank) is 124.5 cm. Aortas with different compliances were used in this setup. The aortic volume compliances were measured by adding incremental volumes of fluid and measuring the incremental change in pressure (see Table 7.1).

Table 7.1
artificial aortas' compliances

aorta No.	volume compliance *(mL/mmHg)*
1	*0.7337*
2	*0.4354*
3	*0.4124*
4	*0.3151*

Setup 2: The experimental setup is similar to Setup 1, but the compliant aorta model was replaced with a rigid tube of the same length. The rigid tube was Masterkleer PVC tubes with an inner diameter of ¾" (≈19 mm) and a thickness of ¼" (note that the inner diameter of the aortic model is 25mm at the inlet that tapers down to 17 at the end).

Setup 3: The experimental setup is similar to Setup 2, but the length of the rigid tube of the rigid side was reduced from 124.5 cm to 62 cm.

For each setup, the experiments were performed at various piston frequencies (heart rates) ranging from 60 bpm to 200 bpm. The flow data was collected for 4 seconds and each experiment was repeated at least five times.

The Setup 1 and 2 experiments were performed under two different stroke rates, $St_1=5\ L/min$ and $St_2=6.5\ L/min$ (for setup 3, only St_1 was performed). The stroke rate is the average total volume displaced by the piston per cycle which is equivalent to cardiac output when valves are present. Note that a higher stroke rate corresponds to a higher wave amplitude or higher amount of energy carried by the waves (see Appendix C). Stroke rates were measured by placing two one-way valves at both sides of the T-junction (see Figure 7.4) and measuring the volume flow rate (The volume flow rate is equal to the piston stroke rate when valves are present).

7.4 Results

7.4.1 Valveless Piston Pumping in Rigid Tubes: Asymmetric Pumping

With this experimental setup (Setup 1), there are two distinct pumping mechanisms, asymmetric pumping and wave pumping. The asymmetric pumping can occur in any rigid and compliant tubes with periodic excitation if asymmetric pressure or energy loss exists. Different tubing or junction characteristics can create these asymmetric losses [116-118].

Figure 7.5a shows the results from experimental Setup 2. The asymmetric pumping is the only effective pumping mechanism in this setup. Both the magnitude and direction of the net flow depend on the piston frequency. This figure shows that the net flow remains the same at all frequencies when the stroke rate increases from $St_1=5\ L/min$ to $St_2=6.5\ L/min$. It is obvious that the stroke rate does not have any effect on the asymmetric pumping of our system. The results of experimental Setup 3 are shown in Figure 7.5b. As the asymmetry changes, here by reducing the tube length of the rigid side, the overall pattern of the “net flow-frequency” curve remains the same. However, the pumping effect increases (magnitude of the net flow increases) as the asymmetry increases. The flow reversing phenomena (negative net flow) in our asymmetric pumping setups (Setup 2 and 3) are in agreement with previous analytical [116] and experimental [117, 118] results.

7.4.2 Impedance Pumping Effect in Compliant Aorta: Wave Pumping

In experimental Setup 1 with the compliant aorta, both the asymmetric and wave pumping mechanism exist. The total pumping is the summation of these two. Figure 7.6a shows the net total flow at different piston frequencies ranged from 60 to 200 bpm for the compliant aorta No.4 (see Table 7.1) with a stroke rate of $St_2=6.5\ L/min$. As shown in this figure, the range of net flow in the compliant aorta (approximately from -0.48 to 1.61) is almost twice the range of the net flow in the rigid tube (approximately from -0.39 to 0.47) due to the presence of an additional pumping mechanism. Figure 7.6b demonstrates the net flow created by the wave pumping mechanism. The curve was computed by subtracting the two curves of Figure 7.6a. Although the asymmetric pumping produced in the rigid tube is not the same as the one created in the compliant aorta, Figure 7.6b shows the significance of the pumping created by the waves.

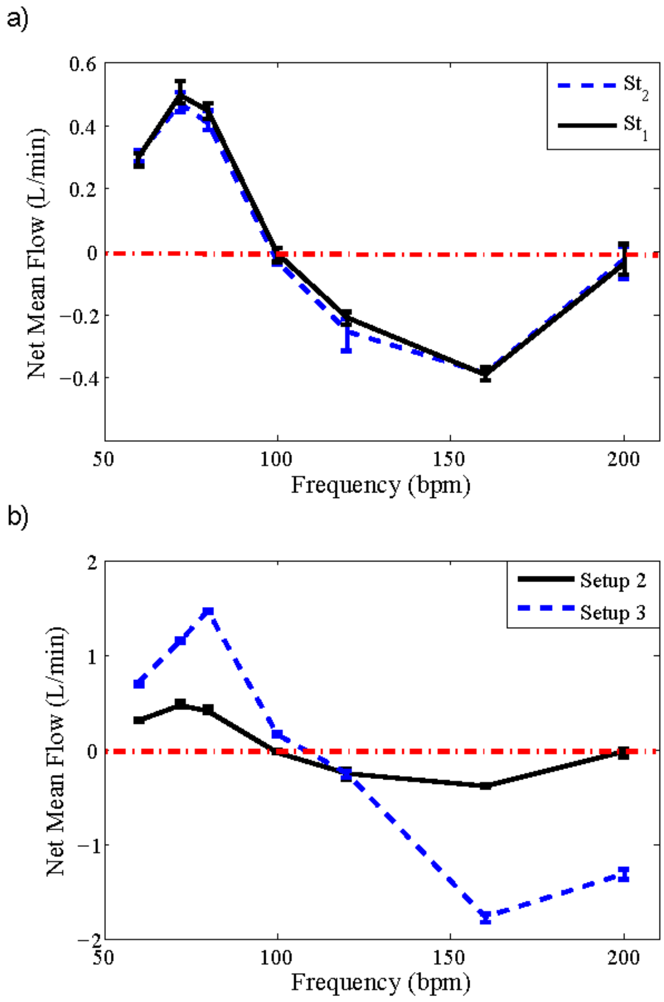

Figure 7.5: Net mean (time averaged) flow at various piston frequencies. a) Results belonging to the experimental setup 2 where St_1=5 *L/min* and St_2=6.5 *L/min*. The two mean flow-frequency graphs are almost identical indicating that the stroke rate has a negligible effect on the asymmetric pumping in our system. b) Comparing the results of setup 2 and 3, the overall pattern is preserved, but the net flow rises as asymmetry increases due to the increased rigid tube's length ratio.

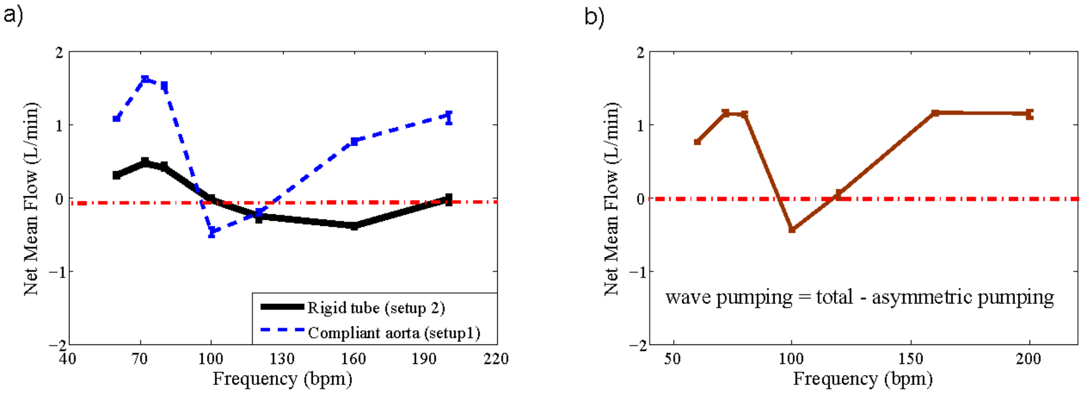

Total pumping in compliant aorta = asymmetric pumping + wave pumping

Figure 7.6: There are two pumping mechanisms in the compliant aorta that create the net flow, asymmetric pumping, and wave pumping. a) Net mean flow at various piston frequencies for Setup 1 with compliant aorta No.4 (Table 7.1) compared with the net flow of the rigid tube (Setup 2). b) Net mean flow of the wave pumping mechanism at various piston frequencies. The graph was created by subtracting the two curves shown in Figure 7.6a. The results are calculated for the stroke rate of $St_2=6.5$ *L/min*.

7.4.3 Effect of Stroke Rate (Wave Energy)

The net flow changed as the stroke rates changed. This is shown in Figure 7.7a for aorta No. 3 with stroke rates of $St_1=5$ *L/min* and $St_2=6.5$ *L/min* at various frequencies ranging from 60 to 200 bpm. At some frequencies, 80 bpm in this case, changing the stroke rate also changes the direction of the flow. This phenomenon was further investigated by repeating the experiment at five different stroke rates ranging from *4.32* to *7.15 L/min*. The results are provided in Figure 7.7b. In this condition, the asymmetric pumping creates a net flow in the opposite direction of the net flow created by the wave pumping mechanism. The total net flow is negative when the wave pumping is not strong enough to overcome the asymmetric pumping at lower stroke rates (red region of Figure 7.7b). Under higher stroke rates, when waves are carrying a higher amount of energy, the wave pumping effect dominates, so the total net flow becomes positive (green region of Figure 7.7b).

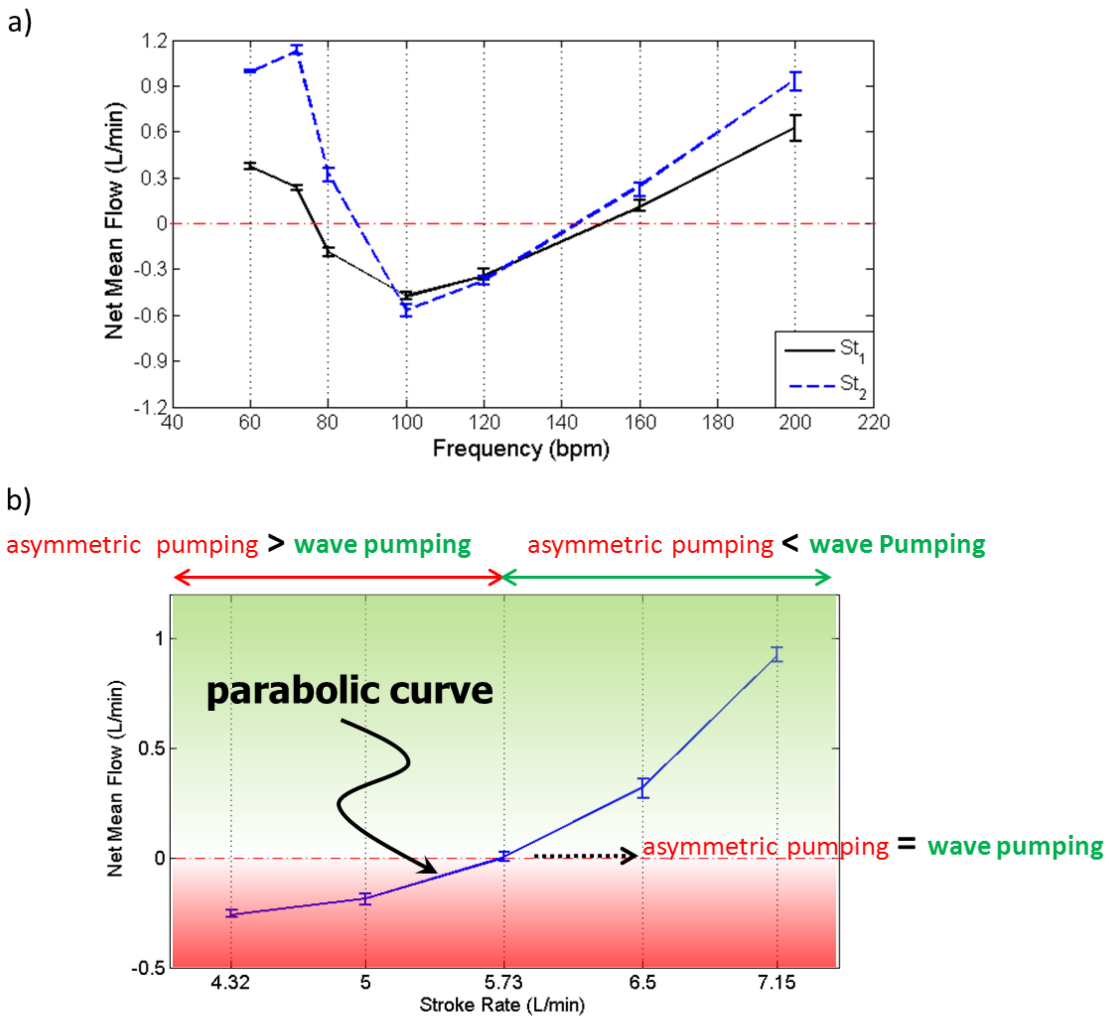

Figure 7.7: Effect of stroke rate (wave amplitude). a) Total net mean flow versus piston frequencies at two stroke rates (St_1=5 *L/min* and St_2=6.5 *L/min*). The net mean flow changes by changing the stroke rate. This indicates the existence of the wave pumping effect since the net flow generated by asymmetric pumping does not change with stroke rate as demonstrated in Figure 7.5a. b) Net mean flow at different stroke rates for aorta No.3 (see Table 7.1) and piston frequency of 80 bpm. As shown, the net flow direction gets reversed by changing the stroke rate in the compliant aorta. In this condition, the asymmetry and the waves are creating a pumping effect in the reverse direction. The red area corresponds to the region where wave energy is not enough to overcome asymmetric pumping. The white region is where the two pumping effects cancel each other. The green region is where waves carry enough energy for wave pumping to overcome asymmetric pumping.

7.4.4 Effect of Compliance (Wave Speed)

The effect of tube compliance on the magnitude and direction of total net flow is shown in Figure 7.7a and 7.7b. The compliance aorta's net flow includes both wave pumping and asymmetric pumping. The rigid case only contains the asymmetric pumping. Figure 7.8a and 7.8b show the net flow for stroke rates of $St_2=6.5\ L/min$ and $St_2=5\ L/min$ respectively. Waves are carrying higher amounts of energy at a higher stroke rate; therefore, the net flow has bigger amplitude at higher stroke rates. This can be observed in Figures 7.8a and 7.8b by comparing the range of the net flow amplitudes. Note that different compliances correspond to different wave speeds. In a similar manner to the behavior of a standard impedance pump, both direction and magnitude of the net mean flow show strong dependence on the tube compliance (the wave speed).

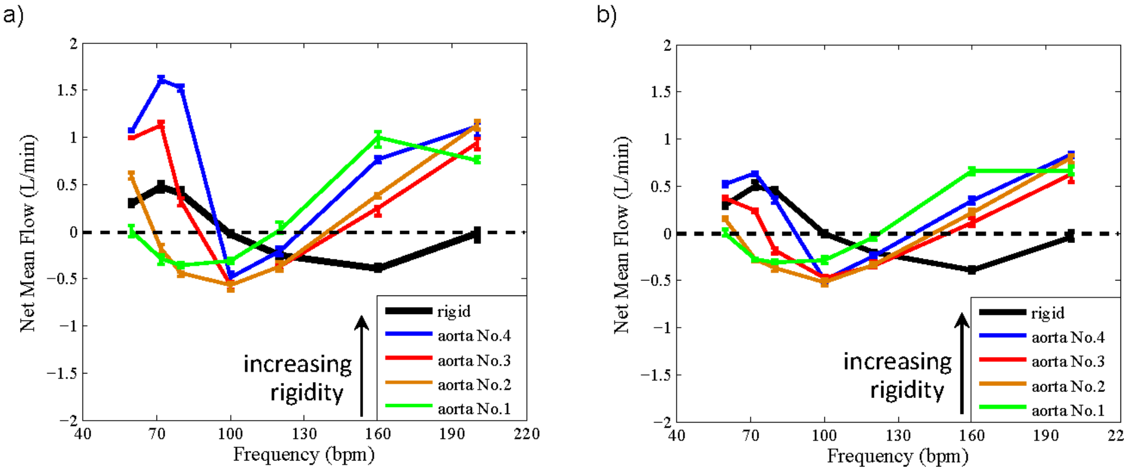

Figure 7.8: Effect of tube compliance (wave speed). The total net mean flow versus piston frequencies for aortas with different compliances (Setup 1) compared to the rigid case (Setup 2). In a similar manner to the behavior of an impedance pump, the magnitude and direction of the net flow change as the tube compliance (wave speed) changes. a) Data are for a stroke rate of $St_2=6.5\ L/min$ b) Data are for a stroke rate of $St_1=5\ L/min$.

7.5 Discussion

The impedance pump (Liebau pump) has been shown to be the effective pumping mechanism in early embryonic life [20]. In addition, Zamir [104] has shown in right coronary arteries that wave reflection can facilitate blood circulation rather than opposing it. This has been recently confirmed in clinical studies [92, 113]. In this chapter, the possible role of wave reflection in creating a pumping effect in the human aorta was investigated. An *in-vitro* model was used to test the hypothesis.

7.5.1 Valveless Piston Pumping in Rigid Tubes: Asymmetric Pumping

Asymmetric pumping can occur in any rigid or compliant tube with periodic excitation if there is any asymmetric resistance and/or energy loss. The wave pumping mechanism, however, happens exclusively in elastic tubes.

The main purpose of Setup 2 and 3 was solely for characterizing the asymmetric pumping of the system and for comparing their results with the results of Setup 1 where both pumping mechanisms are simultaneously active. Asymmetric pumping mechanisms have been studied analytically [116], computationally [117, 118], and experimentally [117, 118] by other investigators and were not the subject of the current study.

The results of experimental Setup 2 were demonstrated in Figure 7.5a. This figure showed that the net flow in asymmetric pumping can be created in both directions depending on the piston frequency. The flow reversing phenomena in asymmetric pumping has also been shown by Propst, analytically [116] and by Takagi *et al.*, experimentally [117, 118]. Using an analytical approach, Propst showed that the pumping direction can be reversed at certain frequencies if the tube friction is sufficiently small [116]. The most important message of this figure is that the stroke rate does not have any effect on the asymmetric pumping of my system.

The results of Setup 2 and 3 were compared in Figure 7.5b. It demonstrated the effect of the tubes' length ratio on the asymmetric pumping. Both graphs have similar patterns in which the maximum net flow in the positive and negative directions happens at the same piston frequencies. The magnitude of the net flow was increased at all frequencies (except when the net flow was close to zero) as the length ratio was increased (hereby reducing the length of the rigid side). The physical explanation is as follows: The loss at each side is proportional to the amplitude of the velocity [116], and the velocity amplitude is inversely proportional to the tube's length [116]. Therefore, as the length ratio increases, the loss difference increases which results in enhancement of the pumping effect (see Propst [116] and Takagi *et al* [117] for more details).

7.5.2 Impedance Pumping Effect in the Compliant Aorta: Wave Pumping

It was demonstrated in Figure 7.6 that the maximum generated total net flow in the compliant aorta (Setup 1) is approximately 3.4 times larger than the one in the rigid tube (Setup 2). Obviously, there must be another pumping mechanism rather than an asymmetric pressure-energy loss mechanism causing the significant elevation of the net flow. The extra assistance in flow generation comes from the wave pumping mechanism. In an impedance pump (a wave pumping mechanism), the net flow depends on various system characteristics such as the frequency of pincher excitation, the pincher location (distance to the reflection sites), the tube compliance (wave speed), and pincher stroke [8-10, 13, 19, 20]. Similarly, the net flow generated by the wave pumping mechanism in the aortic system depends on the piston frequency, the aortic length, the tube's compliance and the piston stroke rate. The asymmetric pumping also depends on the piston frequency and the tube length, so the dependence of the net flow on the piston frequency and aortic length does not help us prove the existence of the wave pumping mechanism. Therefore, the focus in my experiments was on investigating the effect of the stroke rate (wave energy) and the tube's compliance (wave speed).

7.5.3 Effect of the Stroke Rate (Wave Energy)

Figure 7.7a has shown that the stroke rate significantly influences the net total flow. For example, at the frequency of 72 bpm, a 30% increase in the stroke rate results in the net flow increase from *0.23 L/min* to *1.13*. Previously, it was shown in Figure 7.5 that the asymmetric pumping is independent of the stroke rate at all frequencies (ranged from 60 to 200 pbm) in my experimental model. Since the asymmetric pumping is not affected by the piston stroke rate, the dependence of total net flow on the piston stroke rate proves the existence of the wave pumping mechanism in the compliant aorta.

The coexistence of the two pumping mechanisms (asymmetric and wave) in my system is clearly represented in Figure 7.7b. This figure depicts a case where the asymmetric pumping and wave pumping mechanisms are creating net flow in the opposite directions. At a sufficiently low stroke rate (*St <5.73 L/min*), the asymmetric pumping is dominated, so the net flow assumes a negative sign (red region of Figure 7.7b). The net flow generated by the wave pumping mechanism is proportional to the power (or energy) carried by the waves. The power carried by the waves in the system (compliant tube + piston pump) is proportional to

$$\boxed{\bar{P} \propto St^2 \frac{h^2 f_p^2}{c}}. \qquad (7.1)$$

Here, $\bar{P}$ is the time averaged power (energy rate), *St* is the amplitude of the piston stroke rate, f_p is the frequency of the piston wave, and c is the wave speed. Also, h is a function of the tube's material properties, fluid density, fluid viscosity, and tube diameter (see Appendix C for derivations). Hence, for a fixed given experimental setup, aortic model and piston frequency, the net flow generated by the wave pumping mechanism is directly proportional to the square of the stroke rate ($\bar{q} \propto St^2$). As shown in Figure 7.5, the net flow generated by the asymmetry remains constant when the stroke rate increases. On the other hand, the net flow of the wave pumping increases parabolically with the stroke rate. Therefore, by further increasing the stroke rate (*St >5.73 L/min*), the wave pumping overcomes the asymmetric pumping and net flow becomes positive (green region of Figure 7.7b). Note that the parabolic shape of the “net flow-stroke rate” curve is in agreement with the above analytical prediction.

7.5.4 Effect of the Compliance (Wave Speed)

Any small changes in the wave characteristics may significantly affect the wave dynamic in an elastic tube due to nonlinearity of the dynamics and resonance effect of the wave interactions [8, 9, 18, 102, 119]. Wave speed (tube’s compliance) is one of the most influential wave dynamic characteristics that can significantly change the system’s outcome.

Figure 7.8a and b demonstrate the dependence of the outcome (net flow) on the tube compliance (wave speed). These figures show that both direction and magnitude of the net flow can change as tube compliance changes. At some piston frequencies (e.g. 72 and 80 bpm) different tube compliances can produce net flow in the opposite direction. The strong dependency of the net flow on the tube compliance proves that the asymmetric pumping is not the only pumping mechanism in our system; there is another dominant pumping mechanism which is ruled by waves. It was also shown in Figure 7.8a and b that the amplitude and direction of the net flow is significantly influenced by piston frequency and stroke rates which further supports the existence of the wave pumping mechanism in the aortic model.

7.5.5 Limitations

The most important limitation of this study is related to the *in-vitro* modeling of the aorta-heart system. Due to the forward net flow generated by the heart and existence of the aortic valve, the dynamics of the heart-aorta system in a true physiological situation is different from my *in-vitro* experimental model. This means that the model's optimum frequency, in which the maximum net flow (produced by aortic waves) occurs, and its net flow magnitude may not be the same as the ones in a true physiological situation. However, this limitation does not affect the proposed hypothesis since the goal in this study was to prove the existence of the wave pumping mechanism in the aorta. Another limitation of this study is related to neglecting microcirculatory resistance in my *in-vitro* experiment. However, this simplification does not change the main finding of this study since capillary resistance does not influence the wave dynamics (the capillary resistance only affects the mean value of the pressure wave).

The experimental setup (Setup 1) also contains limitations since both asymmetric pumping and the under study wave pumping mechanism are active simultaneously. However, control setups (Setups 2 and 3) were employed to distinguish the features of the wave pumping from the asymmetric pumping.

7.6 Conclusion

The result of this chapter indicates that wave reflection in the aorta creates a pumping effect similar to that of an impedance pump. The pumping effect can generate net flow in both forward and backward directions depending on the state of the wave dynamics. The aorta facilitates the circulation of the blood when it acts as pump. Under the aorta-pump condition, the pulsatile power is reduced which results in workload reduction of the heart. When the aorta is pumping backward, the heart needs to generate more power to overcome the extra load created by the aorta.

The aorta generates a small pumping effect compared to the heart. However, this small pumping effect may play an important role in disease conditions such as heart failure and in extreme conditions, heavy exercise. The results reported here provide a better understanding of aortic wave dynamics and can potentially help us to design methods to optimize wave dynamics. These could include both pharmacologic agents and interventional devices. For example, methods can be created in which the wave reflection sites are modified through surgical implants in order to minimize LV pulsatile load. Reduction of pulsatile load through such techniques may significantly improve LV function in patients with HF.

Chapter 8

CARDIOVASCULAR INTRINSIC FREQUENCY AS A MEDICAL DIAGNOSTIC INDEX

8.1 Chapter Abstract

During the systolic phase of the cardiac cycle when the aortic valve stays open, the left ventricle of the heart and the aorta act as a coupled dynamical system. The heart and aorta act as a decoupled system when the aortic valve is closed. Therefore, the range of characteristic frequencies of the heart-aorta system is different before and after valve closure. The dominant frequencies of these ranges were referred to as *Intrinsic Frequencies*. It will be shown that when the two intrinsic frequencies are equal, the left ventricle pulsatile workload is minimized. Intrinsic frequencies from clinical pressure data indicate that the total frequency variation increases with age or cardiovascular diseases. Using clinical data, the clinical significance of intrinsic frequencies will also be demonstrated. In this respect intrinsic frequency can be considered as a new medical index for cardiovascular disease diagnosis. To obtain intrinsic frequency, only a single waveform, without calibration, is required.

8.2 Introduction

Cardiovascular diseases (CVD) are the underlying cause of over 831,000 deaths in United States each year [1]. Approximately 5,800,000 patients have been diagnosed with heart failure (HF) in the US and this number is growing every year [1]. Clearly, with the advent of telemedicine, there is a need to develop new methods for early diagnosis and monitoring CVDs such as CHF. Such methods have the potential to reduce the death rate and the high medical costs associated with repeated hospitalization. The goal in this chapter is to describe a new method for pressure wave analysis and to introduce a new index for detection of CVDs and evaluation of their severity.

It is perhaps most convenient to think of CHF in terms of the cardio-circulatory or hemodynamic model of heart failure. In this model, heart failure is considered to arise either from deficiencies in heart's pumping capacity or elevation of peripheral vascular resistance or both. Obviously, such model is an oversimplification of the pathogenesis of clinical heart failure which involves a complex interplay between neurohormonal and hemodynamic mechanisms leading to salt and water retention, and reduced cardiac output [120].

The mechanical load on the left ventricle (LV) is composed of steady and pulsatile components[7]. The steady load is due to the total arterial resistance. The pulsatile load is a dynamic type and it is the result of a complex dynamic interaction between the LV and the arterial system. To better understand this complex dynamic process, one should acknowledge that heart is a pulsatile pump which sends pressure and flow waves into the compliant aorta and arterial network. These waves reflect from various reflection sites in the arterial system and partially reflect and interact with the incoming waves. The wave dynamics created by these interacting waves dominates the hemodynamics of the aorta and its branches. These waves also carry information about the diseases of the heart, vascular disease, and coupling of heart and arterial network [66, 94, 119, 121]. This fact was known and used by ancient Chinese and Hindu physicians who over centuries had developed the art of reading cardiovascular health from the heart pulse [122, 123]. Modern efforts in offering a quantitative version of this ancient art has seen a mixed success since these efforts treated the heart and vascular system as a "black box" system and paid less attention to the physical nature and genesis of the vascular wave dynamics. As a result, extracting reliable information from waves about health or disease conditions has remained as a great challenge to modern medicine.

Recent methods for analyzing arterial pulse waveform include methods based on frequency domain (Fourier analysis) [7, 124], and a second group which are based on time domain information such as wave intensity analysis (WIA)[41] . Simultaneous acquisition of pressure and flow waves at a given location is required for these techniques to render results. Efforts to achieve similar objectives based on pressure or flow alone have not been successful in providing conclusive results [7]. Here I introduce a novel method of wave analysis that provides the potential for providing valuable clinical information based on a single pressure or vessel wall displacement waveform.

This approach is based on a deeper understanding of the delicate coupling and balance between heart pumping characteristics and arterial wave dynamics in a healthy cardiovascular system. This optimum coupling and balance can be impaired due to increased arterial stiffness, aging, smoking, or disease conditions such hypertension and heart failure [7]. Significant efforts have been made in the past to elucidate the complex interaction between the left ventricular and wave dynamics of the large central arteries such as the aorta [7, 63, 121, 125, 126]. It is well accepted that the dynamics of the LV, arterial wave dynamics, and the interaction between the two determine the pressure wave [7, 94, 121]. This means the pressure wave contains information about these dynamic systems and their optimum coupling.

It was shown in Chapter 4 that, at a given left ventricle and vascular condition, there exists an optimum HR that minimizes the LV external pulsatile power. In this chapter, it will be demonstrated that a modified version of the Sparse Time-Frequency Representation (STFR) method can be used to identify this optimum heart rate from the pressure wave alone. The Sparse Time-Frequency Representation (STFR) method is inspired by the Empirical Mode Decomposition method (EMD) [127]. It provides a more systematic way to define instantaneous frequency. Like the EMD method, this approach is well suited to analyze nonlinear non-stationary data, and is less sensitive to noise perturbation. Additionally, this method preserves some intrinsic physical properties of the signal [128, 129]. The application of the EMD method in biological problems has been introduced by Huang *et al* [130, 131]. In this chapter, I show the potential of this concept to diagnose heart and vascular diseases as well as its potential to quantify the optimum coupling between the heart and aorta.

The left ventricle of the heart and aorta create a coupled dynamic system before the closure of the aortic valve. The onset of aortic valve closure is marked by the dicrotic notch on the aortic input pressure wave. This coupled dynamic system has a dominant frequency which is not necessarily constant over the cycle and not always equal to the heart rate. However, there is no argument over the idea that this dominant frequency is influenced by the dynamic of both the heart and the aorta. After the valve closure, they get decoupled from each other. This means that the dominant frequency is dictated only by the wave dynamics inside the aorta and its branches. The dominant frequency of the coupled system (heart+aorta) is not necessarily the same as the dominant frequency of the decoupled system (aorta). Furthermore, these dominant frequencies are not necessarily constant in time (they are instantaneous frequencies). I refer to these dominant frequencies as *Intrinsic Frequencies* (ω_1 and ω_2). *The Intrinsic Frequency* (*IF*) is basically the dominant frequency of the heart+aorta system during the specified interval of the cardiac cycle. The main objective in this chapter is to introduce the concept of *Intrinsic Frequency (IF)* as a new medical index for identification of the optimum heart rate and for diagnosis of cardiovascular diseases.

8.3 Methods

8.3.1 Computational Aorta

A three-dimensional axisymmetric model of the aorta was considered. The computational model was physiologically relevant. The methods as well as the physical parameters of the model were the same as Chapter 4 where full details of the computational model were provided.

Information about the physical model, mathematical model, inflow boundary condition, and outflow boundary condition are the same as those given in Chapter 4.

The simulations were performed for different levels of aortic rigidities labeled E_1 through E_7, where E_1 is the aortic rigidity of a 30-year old healthy individual [7]. All the other E_i are multiplicative factor of E_1 as: $E_2=1.25E_1$, $E_3=1.5E_1$, $E_4=1.75\ E_1$, $E_5=2E_1$, $E_6=2.5E_1$, and $E_7=3E_1$. The numerical values of E_i are the same as Chapter 4. At each E_i, simulations were completed for eight heart rates (70.5, 75, 89.5, 100, 120, 136.4, 150, and 187.5 beats per minute (bpm)). All other model parameters such as cardiac output (CO), terminal resistance, terminal compliance, and the shape of inflow wave were kept constant in all simulations.

8.3.2 Sparse Time-Frequency Representation (STFR)

8.3.2.1 Brief Introduction to STFR

In the past decade, there has been an increasing interest in developing new adaptive data analysis methods that can handle non-linear and non-stationary data effectively [132]. Inspired by the Empirical Decomposition Method (EMD)[127], a new method of Sparse Time-Frequency Representation (STFR) was introduced [128]. An essential feature of this approach is that it uses a basis (dictionary) that is adapted to the data itself. By using this data-driven multiscale basis, one can find a sparse representation of a highly complex multiscale signal by solving a nonlinear optimization problem [128, 129] . Each component of this sparse time frequency decomposition gives an Intrinsic Mode Function (IMF) which can be characterized by a slowly varying envelope and an instantaneous frequency. Under certain scale separation assumptions, it can be shown that the STFR decomposition can accurately recover the original signal uniquely up to an approximation error determined by the degree of scale separation. As shown by Hou and Shi [129], the STFR decomposition can recover some of the hidden physical information from the data.

8.3.2.2 Adaptive method of STFR

The notion of *Intrinsic Mode Function (IMF)* was first introduced by Huang *et al* [127]. A more mathematical definition of *IMF* is defined by Hou and Shi [128] as follows:

A signal *f(t)* is called an *Intrinsic Mode Function (IMF)* if there exists an *envelope, a(t) > 0*, and a *phase function ,θ(t)*, satisfying two properties: (i) *a(t)* is smoother (more slowly varying) than *cosθ(t)*, and (ii) *θ(t)* is strictly increasing in time.

$$f(t) \triangleq a(t)\cos\big(\theta(t)\big) \qquad , \qquad t \in \Re\,. \tag{8.1}$$

A real signal *s(t)* is called an *Intrinsic Signal (IS)* if it can be decomposed into a finite sum of IMFs:

$$s(t) = \sum_{i=1}^{M} a_i(t)\cos\theta_i(t)\;. \tag{8.2}$$

The essential idea behind the STFR is to find the sparsest representation of a multiscale data within the largest possible dictionary of IMFs. This huge dictionary consists of elements (or bases) that are not defined a priori. The use of an infinitely dimensional highly redundant data-driven basis is what makes the STFR truly adaptive. Based on an approximation, the STFR method can be reduced to an L_2 minimization problem [129]. The description of the L_2-STFR algorithm is provided in appendix D.

8.3.2.3 Modified STFR for Heart-Aorta System: Intrinsic Frequency Algorithm

In this proposed method, it is assumed that the instantaneous frequency of the coupled heart-aorta and decoupled aorta are piecewise constant in time. This enables us to extract the *Intrinsic Frequencies* directly from the pressure waves. Intrinsic frequency is the frequency that carries the maximum power in Equation 8.2. To extract the intrinsic frequency, a simple but effective norm-2

(L_2) minimization method is proposed. The envelopes of the IMF are also assumed to be piecewise constant in time to distinguish between the two systems. Hence, the L_2 minimization problem, for the extraction of the trend and frequency content of the input aortic pressure wave, is proposed as follows:

$minimize$:

$$\|f(t) - \chi(0, T_0)\, s_1(t) - \chi(T_0, T)\, s_2(t) - c\|_2^2 \,. \tag{8.3}$$

$Subject\ to$:

$$a_1 \cos(\omega_1 T_0) + b_1 \sin(\omega_1 T_0) = a_2 \cos(\omega_2 T_0) + b_2 \sin(\omega_2 T_0), \tag{8.4}$$

$$a_1 = a_2 \cos(\omega_2 T) + b_2 \sin(\omega_2 T), \tag{8.5}$$

$$s_1(t) = a_1 \cos(\omega_1 t) + b_1 \sin(\omega_1 t), \tag{8.6}$$

and

$$s_2(t) = a_2 \cos(\omega_2 t) + b_2 \sin(\omega_2 t). \tag{8.7}$$

Here,

$$\chi(a, b) = \begin{cases} 1 & a \le t \le b \\ 0 & otherwise \end{cases} . \tag{8.8}$$

This problem is now reduced to solving for a_1, a_2, c, b_1, b_2, ω_1, and ω_2. Equation 8.4 and 8.5 are linear constraints that ensure the continuity of the trend at the time T_0 (dicrotic notch) and the periodicity of the trend, respectively. This minimization states that the aortic input pressure wave can be approximated by incomplete sinusoids with different frequencies (ω_1, ω_2), which I refer to as *Intrinsic Frequencies (IF)*. ω_1 is the *IF* for the heart-aorta system (before aortic valve closure = before dicrotic notch), and ω_2 is the *IF* for the decoupled aorta (after aortic valve closure = after dicrotic notch).

The original minimization problem is not convex. Thus there may be several local minima. To find the global minimum, a *brute-force algorithm* over all possible values of frequencies is used to ensure that the corresponding minimizer frequencies $(\omega_1, \omega_2)_m$ are in fact the unique global minimizer frequencies of the original minimization problem. The details about the *brute-force algorithm* are provided in Appendix E.

8.3.3 Clinical Method

The retrospective patient data after de-identification were used. The invasive blind clinical data were obtained from patients having clinically indicated procedures in the cardiac Cath Lab at Keck Medical Center, University of Southern California. Data generated were part of routine procedural processes. There was no modification of the clinical procedure to generate the needed clinical data.

8.4 Results

Three sets of results are provided in this section. First, the adaptive STFR method was applied on the pressure wave to extract the instantaneous frequency $(\dot{\theta}_1(t) = \frac{d\theta_1}{dt})$ of the first intrinsic mode function (IMF). Second, for each aortic rigidity case, the intrinsic frequency ($\omega_1$and ω_2)-HR curve was sketched and compared with the corresponding pulsatile power-HR graph. Third, $\omega_1$and $\omega_2$were extracted from sample clinical data of different human subjects to show the potential of the intrinsic frequency method for CVD diagnosis.

8.4.1 Instantaneous Frequency of the Pressure Waves

The adoptive STFR method [129] was applied to sample aortic input pressure waves. The instantaneous frequency, $(\dot{\theta}_1(t))$, of the first intrinsic mode function (IMF) was extracted from the pressure wave (Figure 8.1).

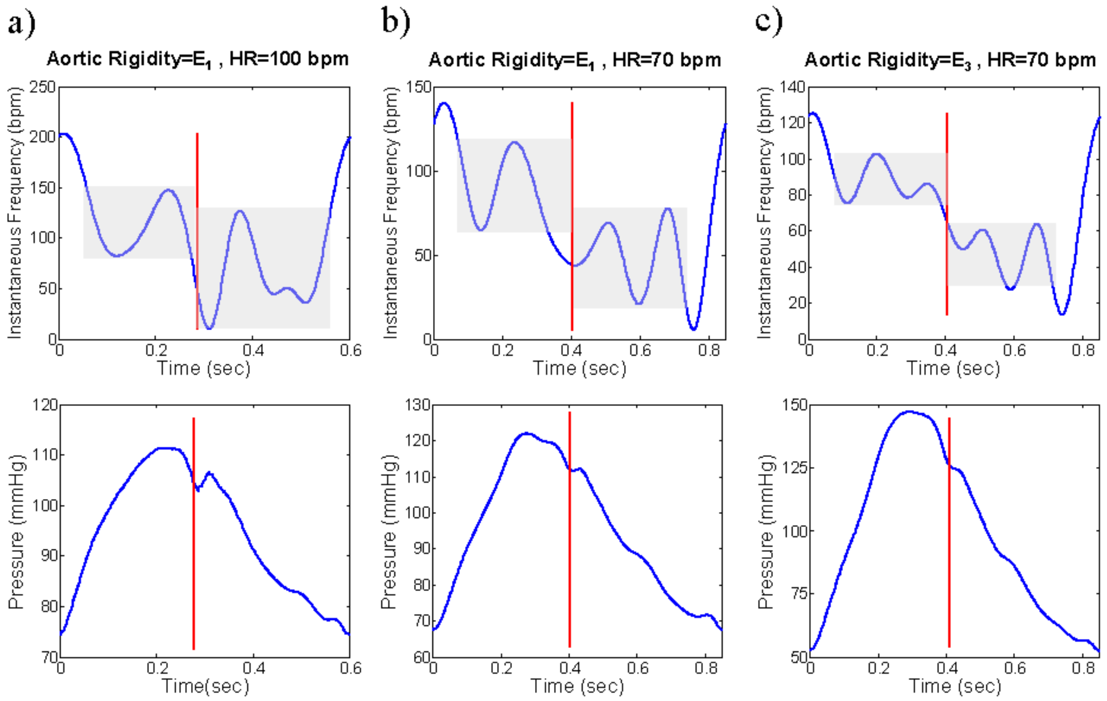

Figure 8.1: Instantaneous frequency of the first IMF. The range of instantaneous frequency oscillation (grey band) changes after the dicrotic notch (marked by the red line). a) Instantaneous frequency (top) of the aortic input pressure (bottom) for an aorta with rigidity E_1 at HR=100 bpm. b) Instantaneous frequency (top) of the aortic input pressure (bottom) for an aorta with rigidity E_1 at HR=70 bpm. c) Instantaneous frequency (top) of the aortic input pressure (bottom) for an aorta with rigidity E_3 at HR=70 bpm ($E_3 = 1.5E_1$). E_1 is the aortic rigidity of a 30-year old healthy individual [7]. The numerical values of E_i are the same as those in Chapter 4.

The instantaneous frequency oscillates around a dominant frequency (marked by a gray band) at the beginning of the cardiac cycle and then drops to a different range of frequencies and oscillates around a different dominant frequency (Figure 8.1). The frequency range transition occurred around the time during the cardiac cycle (marked by a red line) that coincides with the dicrotic notch. These findings indicate that there are two different dominant frequencies before and after the dicrotic notch. I call the above-mentioned dominant frequencies *Intrinsic Frequencies*. Based on the observation from instantaneous frequency graphs (Figure 8.1), the modified version of STFR for the heart-aorta system to calculate the *Intrinsic Frequencies* is proposed (see method section). In this proposed method, it is assumed that the instantaneous frequency of the coupled heart-aorta and decoupled aorta are piecewise constant in time. This enables us to extract the *Intrinsic Frequencies* directly from the pressure waves.

8.4.2 Optimum Heart Rate Prediction

The two intrinsic frequency (IF) graphs, ω_1 and ω_2, cross each other at the optimum HR at which the LV pulsatile power requirement is minimized (Figure 8.2). In other words, the LV pulsatile power reaches its minimum when the two intrinsic frequencies become equal. This is shown in Figure 8.2 for three levels of aortic rigidity (E_1, $E_2=1.25\ E_1$,and $E_3= 1.5\ E_1$).

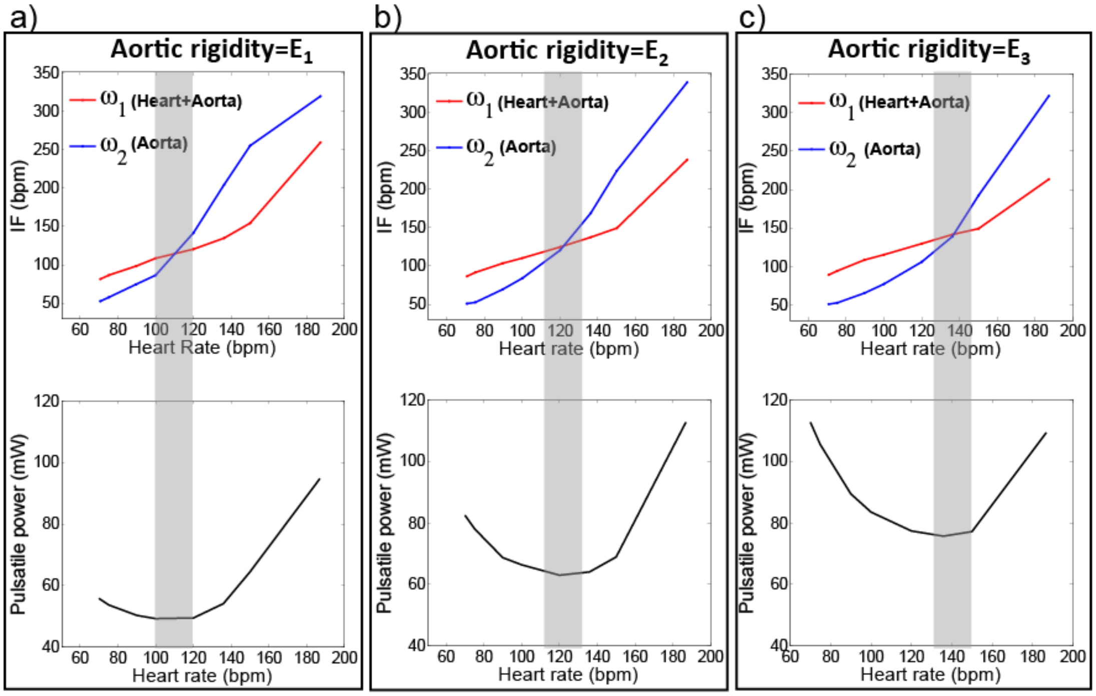

Figure 8.2: Intrinsic frequencies (top) and pulsatile power (bottom) vs. HR. ω_1 (red) is the IF for coupled heart+aorta and ω_2 (blue) is the IF for the decoupled aorta. a) Aortic rigidity is E_1, the grey band shows that the two IF curves cross each other at the optimum HR (≈110 bpm). b) Aortic rigidity is E_2, the two IF curves cross each other at the optimum HR (≈120 bpm). c) Aortic rigidity is E_3, two IF curves cross each other at the optimum HR (≈140 bpm).

Pulsatile power P_{pulse} was calculated using Equation 8.9:

$$P_{pulse} = \frac{1}{T}\int_0^T p(t)q(t)dt - p_{mean}q_{mean} \ , \tag{8.9}$$

where *p(t)* is the pressure, *q(t)* is the flow, p_{mean} is the mean pressure, q_{mean} is the mean flow, and *T* is the period of cardiac cycle.

It is demonstrated in Figure 8.3 that this phenomenon (matching intrinsic frequencies at optimum HR) still exists at high aortic rigidities, two- or three-fold greater than those of Figure 8.2.

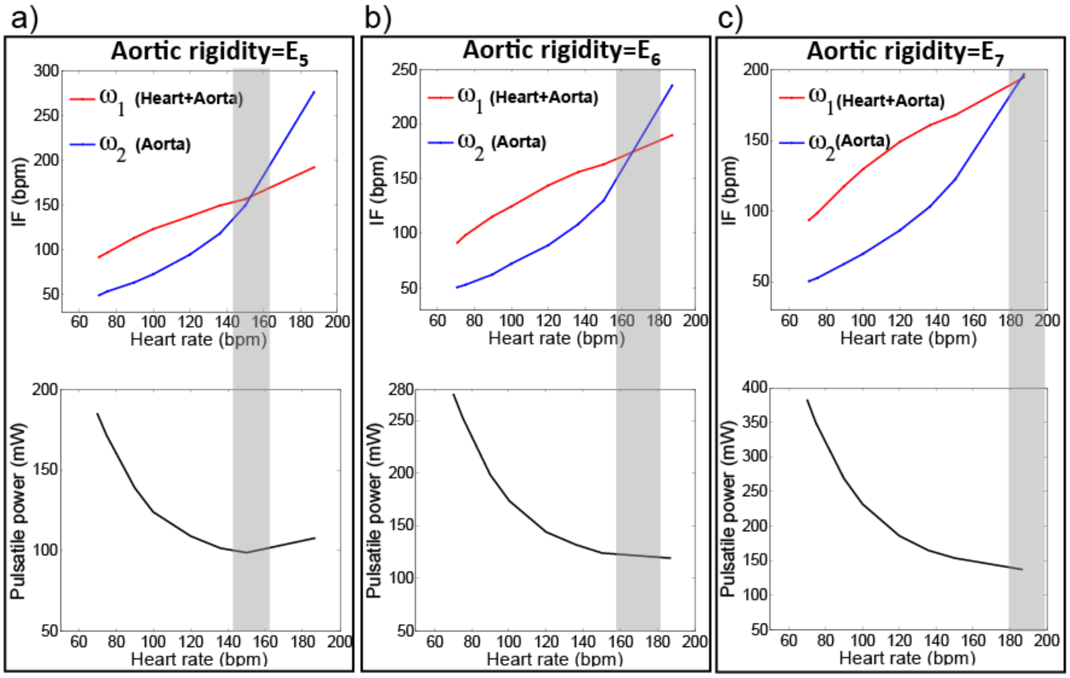

Figure 8.3: Intrinsic frequencies (IFs) and pulsatile power at high values of aortic rigidities. ω_1 (red) is the IF for the coupled heart+aorta and ω_2 (blue) is the IF for the decoupled aorta. The grey band shows that the two IF curves cross each other at their corresponding optimum HR. a), b) and c) are for aortic rigidities of E_5 $(= 2E_1)$, E_6 $(= 2.5E_1)$, and E_7 $(=3E_1)$, respectively.

Another important observation in Figures 8.2 and 8.3 is that at the optimum HR where intrinsic frequencies are equal, the values of intrinsic frequencies are also close to the value of the HR. For example, in aortic rigidity E_2, the optimum HR occurs around 120 bpm where ω_1=125 bpm and ω_2=120 bpm. The same can be seen for all other aortic rigidity cases.

8.4.3 Total Frequency Variation: An Index for Cardiovascular Health and Disease Diagnosis

The total frequency variation ($\Delta\omega$) can be used as an index for quantifying the efficient coupling between heart and arterial system. Figure 8.4 shows $\Delta\omega$ variation with age for healthy and diseased cardiovascular conditions. It suggests that $\Delta\omega$ is near zero for younger subjects when the heart-arterial system is operating close to the optimum condition. Also, it suggests that $\Delta\omega$ increases by aging and CVD due to the ventricular-arterial system shift from its optimum coupling.

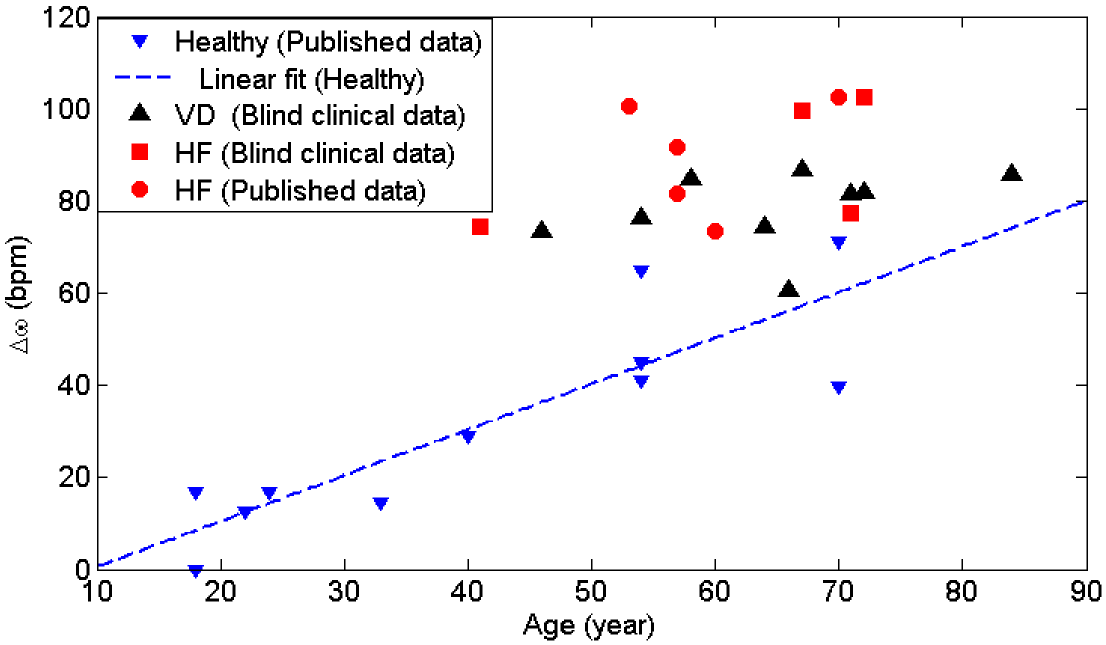

Figure 8.4: Total frequency variation ($\Delta\omega = \omega_1 - \omega_2$) vs age for healthy and CVD condition. The intrinsic frequencies, ω_1 and ω_2, are close to each other in younger subjects; therefore $\Delta\omega$ is zero (or close to zero). Linear fit shows that $\Delta\omega$ increases with age in healthy subjects. $\Delta\omega$ increases in CVD since the ventricular-arterial system shifts away from its optimum coupling. All CVD patients show $\Delta\omega$ >60 bpm. Published data computed from the waveforms taken from Nichols *et al* [7]. HF is heart failure and VD is vascular diseases.

8.4.4 First Intrinsic Frequency (ω_1): A Medical Index for Heart Diseases

The dynamics of the heart-arterial system is dominated by the dynamics of the heart before aortic valve closure. Therefore, ω_1 is more affected by diseases that impair the pumping dynamics of the heart such as heart failure (HF) with LV systolic dysfunction. ω_1 elevates in HF conditions, and remains relatively constant under healthy conditions as age advances (Figure 8.5). It is shown that all subjects with HF in our sample data have $\omega_1>120$ bpm. However, normal healthy subjects have $\omega_1<112$ bpm.

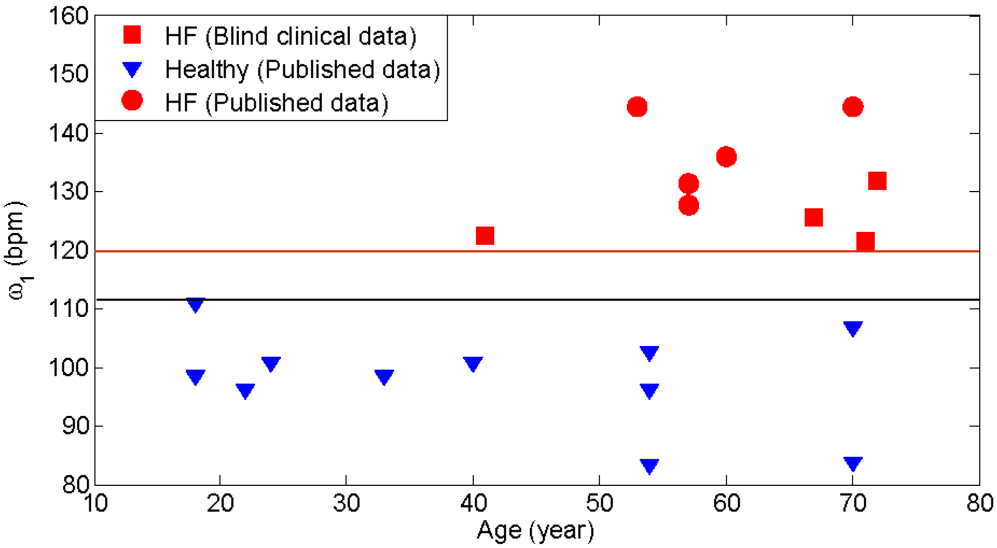

Figure 8.5: ω_1 at different ages and under healthy and HF conditions. All subjects with HF show $\omega_1>120$ bpm (above the red line). Normal subjects show $\omega_1<112$ bpm (below the black line). Published data computed from the waveforms taken from Nichols *et al* [7].

8.4.5 Second Intrinsic Frequency (ω_2): A Medical Index for Vascular Diseases

Aorta and arterial networks dominate the dynamics of the heart-arterial system after aortic valve closure. Hence, ω_2 is more affected by vascular diseases (VD) such as arterial rigidity and hypertension. Figure 8.6 shows variation of ω_2 with age and for healthy and disease conditions. It suggests that ω_2 decreases with age, indicative of arterial rigidity increase with age [66]. This figure also demonstrates that ω_2 drops significantly (below 36 bpm) with certain vascular diseases such as hypertension and peripheral vascular diseases.

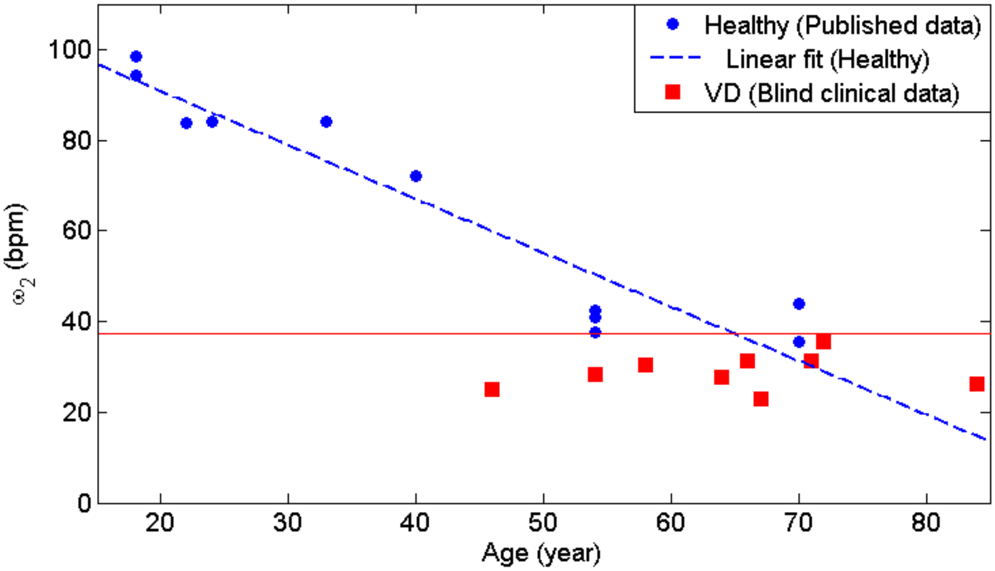

Figure 8.6: ω_2 at different ages and under healthy and VD condition. All VD patients show ω_2<36 bpm (below the red line). Linear fit shows that ω2 decreases with age. Published data computed from the waveforms taken from Nichols *et al* [7].

8.5 Discussion

The main findings of this chapter are as follows: First, the intrinsic frequency concept was introduced for arterial wave analysis. Second, it was shown that at the optimum condition the intrinsic frequencies are equal. Third, the potential use of the intrinsic frequency method was demonstrated for diagnosis of cardiovascular diseases such as arterial stiffening (aging) and heart failure (HF).

It is well accepted that arterial waveform analysis provides clinically valuable information about cardiovascular diseases [7, 66]. In this manuscript, a new method for arterial wave analysis was introduced. This approach is based on a newly developed Sparse Time-Frequency Representation (STFR) method [128]. The main advantage of this method is that only one arterial waveform, namely pressure wave, is required to perform the analysis, in contrast to well-known and widely used impedance and wave intensity methods where both pressure and flow waves are required [7, 41].

A healthy heart operates based on an optimum interaction between wave dynamics of the arterial system and pumping function of the left ventricle (LV). The optimum LV and arterial network coupling can be impaired due to disease conditions (e.g. heart failure and type-2 diabetes) or non-disease conditions (e.g. aging and smoking) [7, 66]. The heart and aorta as a coupled dynamic system have an intrinsic frequency. (Note that in this thesis I use the phrase “heart-aorta system” as an equivalent of “ventricular-arterial system”.) As a dynamic system, the aorta by itself has a different intrinsic frequency. These two frequencies are not necessarily the same and they may not be constant in time during a cardiac cycle. The STFR method was applied to extract the instantaneous frequency of the coupled heart-aorta system and the decoupled aorta from the pressure wave (Figure 8.1). As shown in Figure 8.1, the instantaneous frequency oscillates around different dominant frequencies before and after the dicrotic notch. (The dicrotic notch occurs when aortic valve closes.) These dominant frequencies are the intrinsic frequencies of the system within the considered interval. Here, one interval starts from the beginning of the cardiac cycle and ends at the time of the aortic valve closure. The other interval starts from aortic valve closure time and finishes at the end of the cardiac cycle. The shift in instantaneous frequency range before and after the dicrotic notch was significant in some cases (Figure 8.1b and 8.1c) and it was insignificant in a few others (Figure 8.1a).

The instantaneous frequency was assumed to be piecewise constant in time with the step that occurs at a certain time T_0. This piecewise constant frequency was called the *Intrinsic Frequency (IF).* The choice of T_0 depends on the physics of the system. In the heart-aorta system, the heart and the aorta are coupled with each other when the aortic valve is open. During this time interval, the pressure wave depends on the inflow wave, which is determined by the left ventricle of the heart, and on the characteristics of the aorta and arterial network (e.g. anatomy, physical properties of the vessel and wave reflection). After the closure of the aortic valve, the aorta gets decoupled from the heart and the pressure wave is mostly determined by the characteristics of the aorta and vascular network. Therefore, the pressure wave contains information about the heart, aorta (arterial network), and the coupling between the two. Based on the above explanation, the correct choice of time T_0 is when the aortic valve closes, which is marked by the dicrotic notch in the pressure wave.

To extract the *IF* directly from the waves (here pressure waves), a modified STFR problem was developed using a norm-2 (L_2) minimization method. A brute-force algorithm was applied to solve this problem. This algorithm considers all possible values of frequencies to ensure that the corresponding minimizer frequencies are in fact the unique minimizers of the problem. The piecewise constant frequency before the dicrotic notch is the *IF* of the heart-aorta system and the one after the dicrotic notch is the *IF* of the aortic system (see Equations 8.3, 8.6, and 8.7).

8.5.1 Intrinsic Frequency Matching and Optimum Heart Rate

It has been recently shown that there is an optimum HR at which LV pulsatile power is minimized, and this optimum HR shifts to a higher value as the aortic rigidity increases (see Chapter 4 for details). In order to calculate the pulsatile power, both flow and pressure waves are required. In addition, identifying the optimum HR requires having pressure and flow waves of the same subject at different heart rates. This modified STFR method and intrinsic frequency index can identify this optimum HR using only the pressure wave (Figures 8.2 and 8.3). As it was shown, the two IF curves cross each other at the optimum HR (Figures 8.2 and 8.3). This means that at the optimum HR, the intrinsic frequencies of the heart-aorta system before and after decoupling are equal.

Matching IFs at the optimum HR have been demonstrated for six different levels of aortic rigidity in Figures 8.2 and 8.3.

8.5.2 Intrinsic Frequency as a Cardiovascular Disease Index

The potential clinical application of the intrinsic frequency index was demonstrated in Figures 8.4, 8.5, and 8.6. The intrinsic frequencies are close to each other in young subjects when there is an optimum balance between heart pumping characteristics and wave dynamics of the aorta and its branches (Figure 8.4). This finding suggests that the total frequency variation ($\Delta\omega$) can be considered as a marker of optimum left ventricular-arterial coupling. It is also shown that $\Delta\omega$ increases as the age advances (in agreement with the results of Figures 8.2 and 8.3). For example, in the case of aortic rigidity E_1 with the optimum HR of 110 bpm, the total frequency variation ($\Delta\omega$) is zero; with aging (when aortic rigidity increases) $\Delta\omega$ increases to 31bpm for E_3 (= $1.5E_1$) and to 55 bpm for E_6 (= $3E_1$). Additionally, it is illustrated that $\Delta\omega$ increases (over the predicted increase due to aging) for the cases that show heart or vascular diseases (Figure 8.4).

The potential application of the intrinsic frequency concept in heart disease monitoring and diagnosis can be elucidated by the information depicted in Figure 8.5. It is shown that ω_1 is higher than 120 bpm in patients with LV systolic dysfunction (in this case HF). This indicates that ω_1 can potentially be used to detect impaired LV systolic function. This finding may also indicate that a high value of ω_1 is associated with low ejection fraction (EF). Future work will aim at confirmation of the above observations using more diverse clinical data sets at various stages of heart failure.

Figure 8.6 demonstrates that the changes in the dynamics of the aorta and arterial network due to aging or vascular diseases will be reflected in the value of ω_2. This figure shows that ω_2 decreases with aging. Therefore, ω_2 can be used as a marker of vascular aging. Additionally, it is illustrated that ω_2 drops below 36 bpm, independent of age, under vascular disease conditions. Hence, ω_2 can be potentially be used for diagnosis of vascular diseases and evaluation of their severity.

8.6 Conclusion

A new index, intrinsic frequency, and a quantitative method based on instantaneous frequency theory have been introduced. This index enables physicians to diagnose various cardiovascular diseases and to detect the optimum ventricular-arterial coupling. Using only the pressure waveform, the intrinsic frequency concept can be used to quantify the impaired balance between the heart and aorta under various disease conditions. One important advantage of this method is that only the shape of pressure waveform, not the magnitude, is required to extract the intrinsic frequencies. In this study, the intrinsic frequencies of cardiovascular system were extracted from clinical data under resting conditions. Further investigations will be needed to analyze the intrinsic frequency indices under non-resting conditions such as exercise. These indices may also potentially hold value in the design and evaluation of cardiovascular devices. Future studies are planned to verify the predictive value of this concept in the detection of cardiovascular disease states.

Chapter 9

PATHOLOGICAL WAVE DYNAMICS: A POSTULATE FOR SUDDEN CARDIAC DEATH IN ATHLETES

9.1 Chapter Abstract

Sudden death (SD) in young athletes is a shocking and disturbing event with significant societal impact. Previous studies have demonstrated that sudden cardiac death (SCD) is the leading medical cause of SD in athletes. Various structural and pathological cardiovascular abnormalities have identified as the underlying causes of SCD in young athletes. However, there have been reported cases of SCD in athletes with no structural or pathological cardiovascular disorders. The proposed hypothesis in this chapter is that abnormalities in aortic wave dynamics and coronary wave dynamics may be responsible for SCD in these athletes. These abnormal waves—pathological waves—can act as a trigger toward cardiac death in the presence of cardiovascular diseases. These waves may initiate SCD in the absence of apparent cardiovascular abnormalities. In summary, when the aortic and coronary wave dynamics are abnormal, the myocardial oxygen demand can exceed the oxygen delivery during exercise, hence creating acute ischemia which leads to death. It is explained in this article how increased oxygen demand may be the result of pathological aortic waves while reduced oxygen delivery is mainly due to pathological coronary waves. Additionally, this pathological wave hypothesis is able to provide a plausible explanation for commotio cordis.

9.2 Introduction

Sudden death is always a disturbing event regardless of the cause or the age. The societal impact of the sudden death of an athlete significantly increases when it happens during a live broadcast game or in an international competition. SCD is an unusual event and its actual frequency in athletes is unknown. In fact, the risk of SCD has been underestimated due to inappropriate data collection methods [133]. Recent statistical studies of NCAA compiled lists of athlete deaths have demonstrated that sudden cardiac death (SCD) (16%) is the second leading cause of all sudden deaths in young athletes after accidents (51%), occurring at a higher frequency than athlete deaths by suicide (9%), cancer (7%), homicide (6%), and drug overdose (2%)[133] . This suggests that SCD is the leading medical cause of sudden death in young athletes and demonstrates the need to further investigate the underlying causes of SCD in athletes and young adults.

Various structural and pathological cardiovascular abnormalities have been identified as the underlying causes of SCD in young athletes [134]. These abnormalities include, but are not limited to, hypertrophic cardiomyopathy (HCM), dilated cardiomyopathy (DCM), coronary artery diseases (CAD), left ventricle hypertrophies (LVH), valvular disease, myocarditis, aneurysms, aortic diseases, congenital heart diseases, rhythm and conduction disorders, cardiopulmonary diseases, etc. Among all of these identified causes, cardiomyopathies are the number one cause of SCD in athletes younger than 35 years old, and CAD is by far the leading cause of SCD in athletes older than 35 [135].

There have also been reported cases of SCD with no structural or pathological cardiovascular disorders. The subjects appeared to be normal during autopsy and their cause of SCD remained unknown [136, 137]. The reported incidence of SCD in athletes with no cardiovascular abnormality varies in different studies. However, in general, these account for approximately 21% of total SCD cases [136, 137], and occur more frequently in athletes younger than 21 years old [136]. Given that nearly one out of five SCD cases happen in the absence of cardiovascular abnormalities, it is reasonable to assume that these cases account for roughly 3.4% of all sudden deaths in athletes.

In this chapter, I briefly explain the concept of wave dynamics in cardiovascular systems, and propose abnormal wave dynamics as a form of dynamic pathology that can lead to SCD in athletes. I then investigate different scenarios where abnormalities in aortic and/or coronary waves can cause SCD through acute myocardial ischemia.

9.3 Background

9.3.1 Dynamic Pathology: The Neglected Element

The term dynamic pathology was first introduced by Zamir [114], referring to a pathological condition in which the dynamic of the system diverges from its normal condition. The structural and functional pathology may coexist with the dynamic pathology. However, the absence of structural and functional abnormalities does not preclude the presence of dynamic pathology. SCD does not always occur in all athletes with functional or structural abnormalities, and can occur in apparently healthy young athletes, suggesting that there is a form of special abnormality that does not leave any footprint. I refer to this special abnormality as a form of dynamic pathology. In other words, if a sudden cardiac death is caused solely by a form of dynamic pathology, the subject will appear normal during autopsy. A simple and well-known example of the dynamic pathology is arrhythmia. The dynamic of the heart pumping condition changes during arrhythmia. This alters the optimum coupling between the heart and the aorta. The disturbed heart-aorta coupling affects the arterial network dynamics which results in altered cardiac output [114].

Dynamic pathology can contribute to SCD in young athletes through three different forms: (1) acting acutely as the main cause; (2) acting as the trigger (a trigger is the final component that is necessary for the initiation of the corresponding medical complication); or (3) acting chronically to develop a so-called idiopathic condition (e.g. idiopathic-LVH). If dynamic pathology acts as the main cause of death, the underlying cause remains unknown during autopsy since this form of pathology cannot be identified after the event. Since dynamic pathology can coexist with a structural or functional pathology, it can instigate some fatal event. This could explain why SCD does not occur in all athletes with certain structural abnormality.

9.3.2 Wave Dynamics in Compliant Aorta as a Tube

Aorta is a compliant tube that acts as a conduit for propagation and reflection of the waves. The wave dynamics in a compliant tube is a complex nonlinear phenomenon that includes wave interactions and resonance [8, 10, 12]. Waves in compliant tubes can create a pumping effect as observed in impedance pumps (Liebau pump) [8, 10, 11, 13, 20]. In its simplest form, an impedance pump is composed of a compliant tube connected to two rigid tubes at both ends and a pincher. The pincher hits the compliant tube and creates waves. These waves propagate toward both ends where they reflect upon the impact on the rigid boundary. The wave propagation and reflection in the elastic tube create wave dynamics which may produce pumping effects. The direction and magnitude of the net flow in the impedance pump depends on the state of the wave dynamics which are mainly dominated by three factors: (1) material properties of the compliant tube (defined the wave speed), (2) frequency of the excitation (pincher's frequency), and (3) locations of reflection sites (distance between pincher and rigid tubes) [50, 100, 104, 106, 107].

Despite the complicated physics of the impedance pump, it provides a simple message: *waves can assist circulating fluid in a compliant tubing system in a certain direction*. Note that assisting the flow in one direction means impeding the flow in the opposite direction. The direction and the magnitude of the net flow depend on the wave dynamic characteristics that show nonlinear-type behavior and resonance [8, 10, 11].

9.3.3 Wave Dynamics in Cardiovascular System

The heart creates pulsatile flow. The pulsatile flow generates waves when it enters the compliant aorta. These waves propagate as forward and reflected pressure, flow, and wall displacement waves in the arterial network. The mere existence of these waves establishes unique "wave dynamics" in the arterial system. Previous studies have shown that the cardiovascular system in mammals is designed to optimize the effects of arterial wave dynamics to benefit arterial circulation [58, 98, 102]. These studies have provided valuable information about the constructive interaction, destructive interaction, and resonance behavior of the arterial waves.

The pulsatile workload on the heart is the result of the abovementioned complex wave interactions in the aorta and the arterial network. It has been shown that reducing the heart pulsatile load through optimization of the arterial wave reflection is one of the apparent design criteria in the mammalian cardiovascular system [58, 98]. The aortic (arterial) wave dynamics can reduce the workload on the heart by assisting blood circulation in a forward direction (from heart to the organs) or increase the workload by impeding it (in other words, pushing the blood in the opposite direction). In fact, aortic waves can potentially make the aorta act as a passive pump similar to an impedance pump as shown in Chapter 7. Figure 9.1 depicts this phenomenon.

Another important effect of arterial wave dynamics is the perfusion of coronary arteries. Zamir [104] showed that the effect of wave dynamics in coronary perfusion is far more significant than what was previously assumed. Subsequent clinical studies have confirmed Zamir's finding by showing that the coronary blood flow is completely dominated by the wave dynamics in the coronary arteries [92, 138]. It has been shown in clinical studies that coronary wave dynamics are the result of the interaction of two different wave dynamics: one is created by aortic waves that enter coronary vasculature; the other one is generated at the coronary microcirculation (myocardium) level by the contraction and relaxation of the heart (see Figure 9.2) [92]. Note that the coronary flow is affected by both the timing and magnitude of these waves. Any abnormality in each of these waves and their timings can adversely affect coronary blood flow. For example, Davies *et al* [92] have shown that in LVH patients the reduction of waves generating at the myocardial end is responsible for the impairment of coronary perfusion.

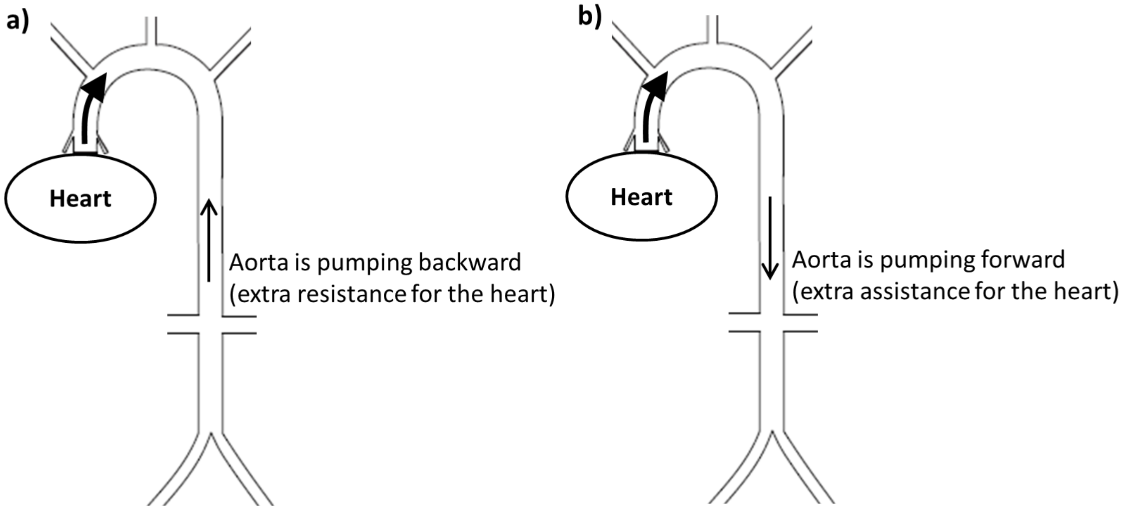

$Waves\ impede \Rightarrow Workload \uparrow$ $Waves\ assist \Rightarrow Workload \downarrow$

Figure 9.1: Effect of aortic waves on the heart workload. a) Aortic waves act destructively and push the flow in the opposite direction. This impedes the blood flow and increases the workload on the heart. b) Aortic waves act constructively and push the flow in a forward direction hence decreasing the workload on the heart.

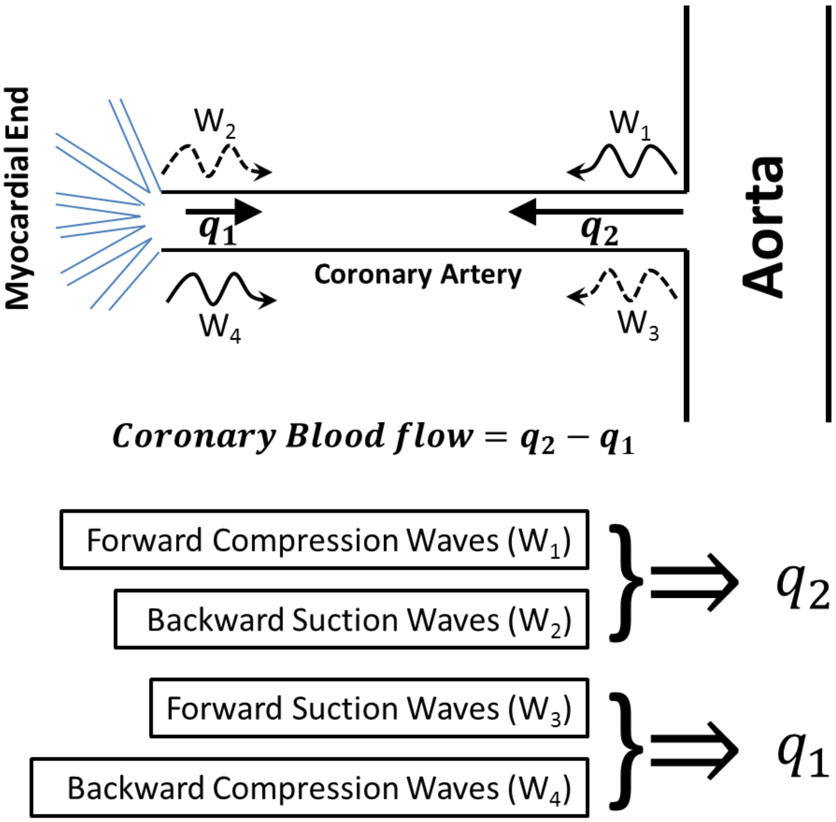

Figure 9.2: Coronary blood flow and coronary wave dynamics. The coronary wave dynamics are composed of four different waves. At the aortic side, compression waves (W_1) and suction waves (W_3) are created during the cardiac cycle. These waves are determined by the dynamics inside the aorta. At the myocardial end, both compression waves (W_4) and suction waves (W_2) are also being created by contraction and relaxation of the heart. q_2 is the blood flow from the aortic side toward the coronary microcirculation, and q_1 is the blood flow in the reverse direction from coronary microcirculation toward the aorta. Since the favored direction of the coronary blood flow is from aorta to myocardium, W_1 (aortic compression) and W_2 (myocardial suction) are assisting and W_3 (aortic suction) and W_4 (myocardial compression) are impeding the blood flow toward the myocardium.

9.3.4 Pathological Waves

Despite the complicated physics of waves in the aorta and coronary vessels, the message is rather simple: (1) aortic waves affect the workload on the heart; (2) waves generated at the myocardial end of coronary vasculature and aortic waves create coronary wave dynamics which determine the coronary blood flow (myocardial perfusion); (3) these waves can act constructively or destructively. Under normal conditions, these waves act constructively where they minimize the heart workload and maximize coronary perfusion. Under abnormal conditions, the waves act destructively which results in the elevation of the heart workload and/or reduction of the coronary blood flow. This abnormal wave condition is a form of dynamic pathology. Here, they are referred to as *pathological waves*. Similar to other forms of dynamic pathology, pathological waves can be the result of a structural pathology or they can be generated by a destructive dynamic interplay among heart, aorta and coronary arteries. The previously mentioned LVH and coronary wave dynamics case is an example of dynamic pathology (abnormal coronary waves) that is caused by a structural pathology (hypertrophied left ventricle).

There are certain structural abnormalities for which an underlying cause cannot be identified; these abnormalities are called idiopathic. Chronically, pathological waves may also be responsible for creating these so-called idiopathic structural pathologies such as idiopathic-LVH. For example, chronic pathological aortic waves can cause idiopathic-LVH by increasing the pulsatile workload on the heart. Using wave intensity analysis, it was shown in Chapter 3 that the left ventricle pulsatile workload can be abnormally high due to the resonance of reflected waves even though both pulse pressure and mean pressure are within a normal range.

Aortic (arterial) and coronary wave dynamics play important roles in both rest and exercise. However, their effects on the heart workload and coronary blood flow are far more significant during exercise since heart rate, ejection fraction, heart contractility, stroke volume, blood pressure, and aortic rigidity are all increasing.

9.4 Hypothesis

I propose that abnormalities in the dynamics of aortic and coronary waves are responsible for sudden cardiac death in athletes. These pathological waves can act as a trigger toward cardiac death when a structural abnormality is present. They are also capable of initiating sudden cardiac death when there are no apparent cardiovascular structural abnormalities.

9.5 Discussion

The very basic mechanism that pathological waves can generate during exercise is as follows: Abnormal aortic waves' interactions first increase the workload on the heart. This then increases the myocardial oxygen demand. At the same time the aortic wave interplay may adversely affect coronary waves as well. (Note that abnormality in aortic wave dynamics is not a necessary condition for pathological coronary waves.) The pathological coronary waves decrease the myocardial oxygen delivery. If the oxygen demand exceeds the oxygen delivery, acute ischemia will occur that may initiate a fatal ventricular arrhythmia (VA) or ventricular fibrillation (VF) (Figure 9.3).

9.5.1 Increased Workload due to Pathological Aortic Waves

The mammalian cardiovascular system is designed to minimize the workload on the heart through different mechanisms [58, 79, 97, 98, 102]. One of these mechanisms is the reduction of the heart workload (the pulsatile part of it) by optimizing the aortic (arterial) wave reflection [98, 102]. It was already shown in Chapter 4 (computationally) and Chapter 5 (experimentally) that there is an optimum heart rate at each level of aortic rigidity that minimizes this pulsatile workload . This optimum shifts to a higher value as rigidity increases. This phenomenon is schematically shown in Figure 9.4.

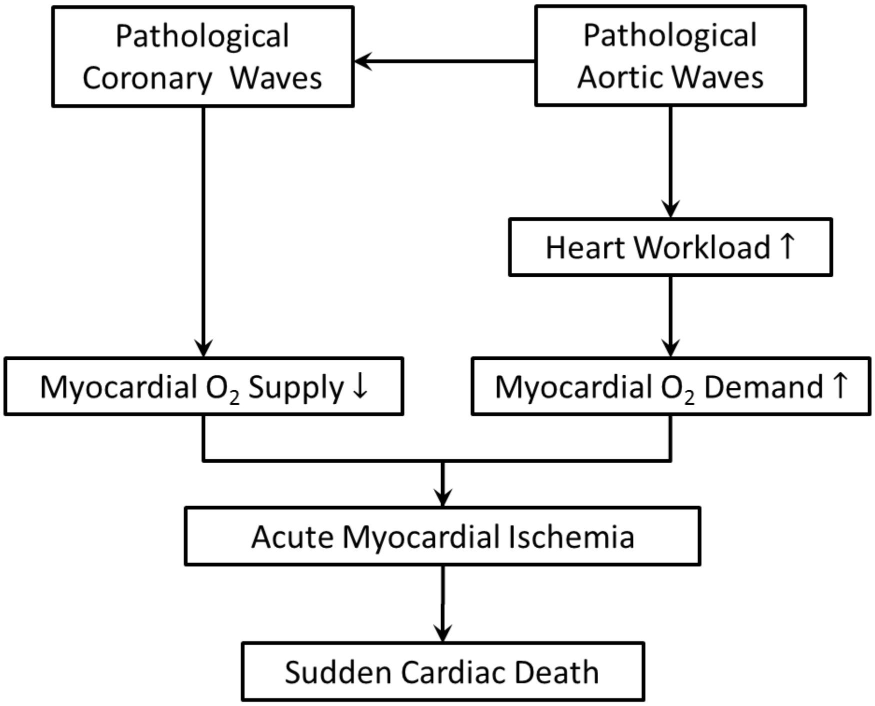

Figure 9.3: Overall mechanism of pathological waves in sudden cardiac death.

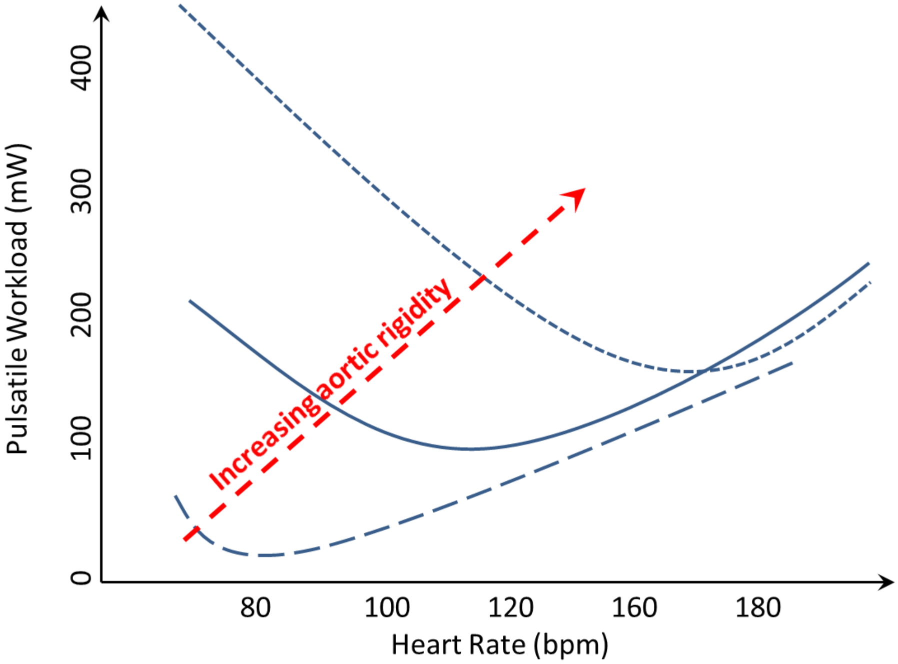

Figure 9.4: Schematic diagram of pulsatile workload vs. heart rate at different levels of aortic rigidity (see Chapters 4 and 5 for details).

During exercise, aortic rigidity (as a consequence of pressure elevation and diameter extension [7]) and heart rate (HR) are both increasing. Under normal (optimized) conditions, the heart beats at its shifted optimum HR during exercise as well. In other words, pulsatile workload on the heart is minimized during exercise under healthy optimal condition as depicted in Figure 9.5. Although an optimal condition at rest dictates a suboptimal state during extreme conditions (e.g. exercise or fight)[99], this suboptimal situation has its own optimum operating point. Note that during exercise, cardiac output and ejection fraction are both increasing. The elevated cardiac output and increased ejection fraction during exercise may slightly shift the pulsatile workload-HR graph up/down or right/left compared to the one presented in Figure 9.5.

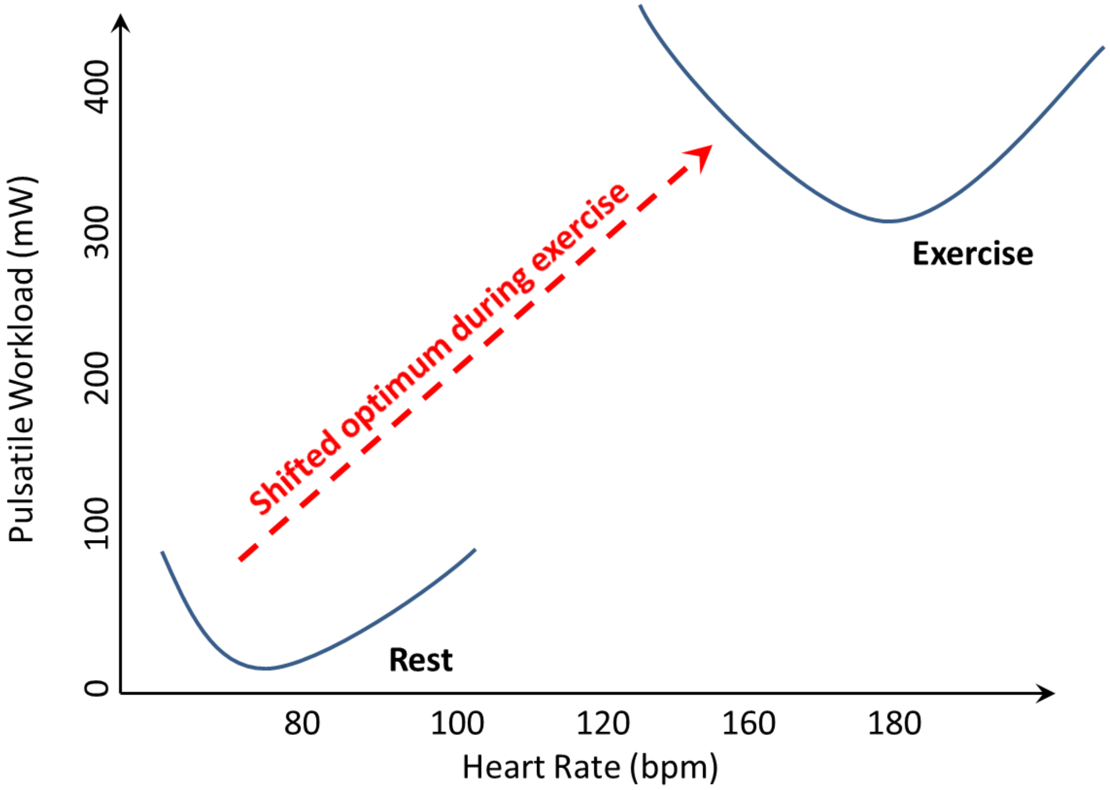

Figure 9.5: Pulsatile workload vs. heart rate curve under resting and exercise condition. Changes in stoke volume and ejection fraction during exercise may shift the exercise curve up-down or right-left. The heart beats at its new shifted optimum HR during exercise when aortic waves are healthy (normal).

Pathological wave condition can occur due to abnormalities in the dynamics of the heart (e.g. HR), dynamics of the aorta and its branches (e.g. HR, arterial rigidity, and reflection site), and/or the dynamic coupling between the heart and the aortic system. Pathological aortic waves may have an underlying structural pathology, or similarly to the other forms of dynamic pathologies, they may occur in the absence of any structural pathology (Figure 9.6).

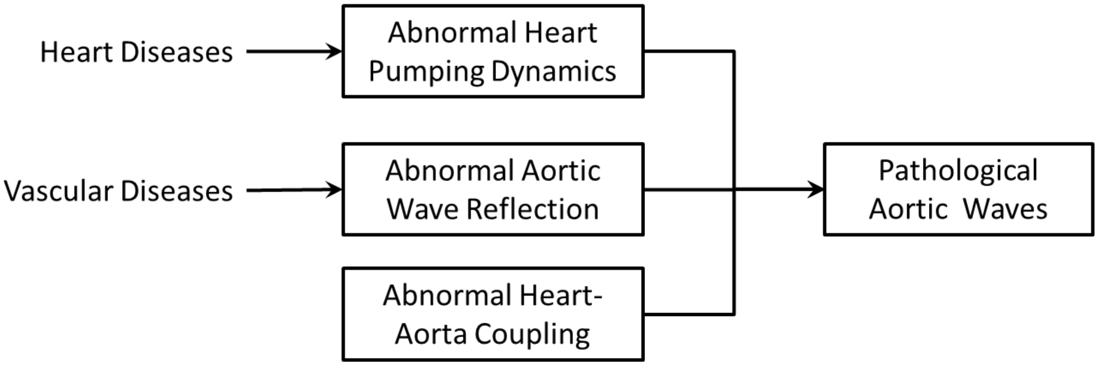

Figure 9.6: Underlying causes of pathological aortic waves.

Due to the resonance behavior of aortic waves, any small change may produce significant impact (positive or negative) on the outcome. During exercise and under the pathological wave condition, the resonance behavior of waves can significantly increase the pulsatile workload. Figure 9.7 shows the constructive and destructive effect of wave resonance on the heart pulsatile workload.

Under the pathological aortic wave condition, the optimum HR diverges from exercise HR which increases heart workload (Figure 9.8). The situation is exacerbated if a destructive resonance accompanies the pathological wave condition (Figure 9.8).

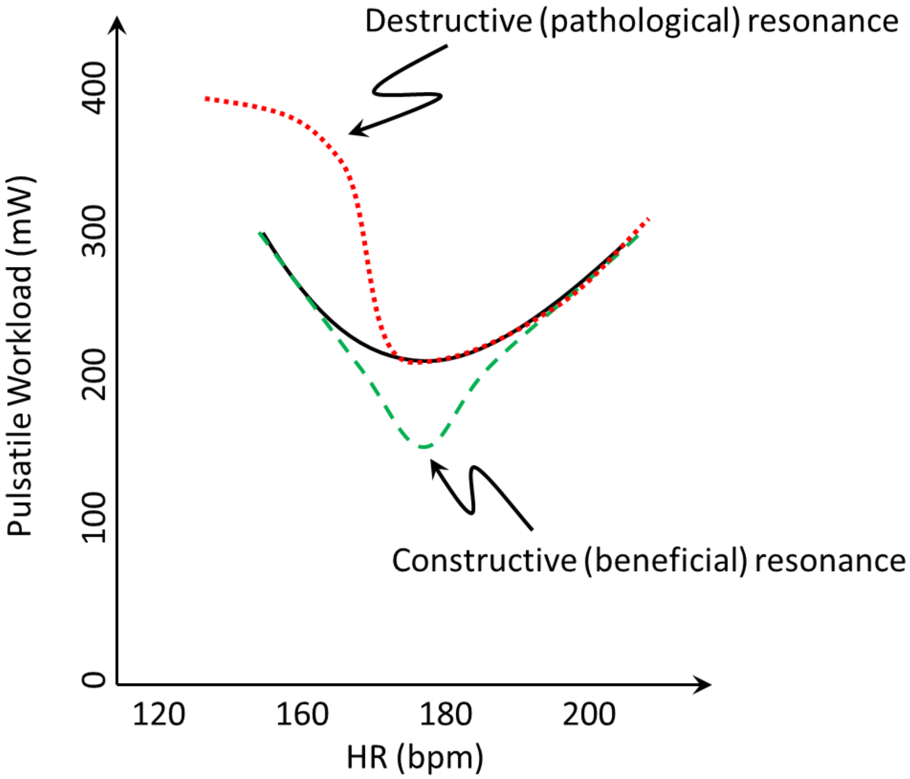

Figure 9.7: Demonstration of the effect of resonance on pulsatile workload during exercise. Black solid curve is the pulsatile workload-heart rate graph without resonance. Green dashed curve is an example of a constructive (beneficial) resonance where pulsatile workload drops due to constructive wave dynamics. Red dotted curve is an example of a destructive (pathological) resonance where pulsatile workload jumps due to destructive wave dynamics.

9.5.2 Reduced Coronary Blood Flow due to Pathological Coronary Waves

Coronary blood flow is the result of the complex interactions of four different waves (Figure 9.2)[92]. Two of these waves propagate from the aortic side (forward waves), and the other two are generated at the myocardial end (backward waves). During the exercise, the cardiovascular system operates close to its limit; hence, the optimal interactions of these waves become crucial for the myocardial perfusion. The blood is pushed toward coronary microcirculation (q_2) by forward compression wave (W_1) and backward suction wave (W_2). It is opposed—or pushed in the reverse direction (q_1) — by forward suction wave (W_3) and backward compression wave (W_4) (see Figure 9.2).

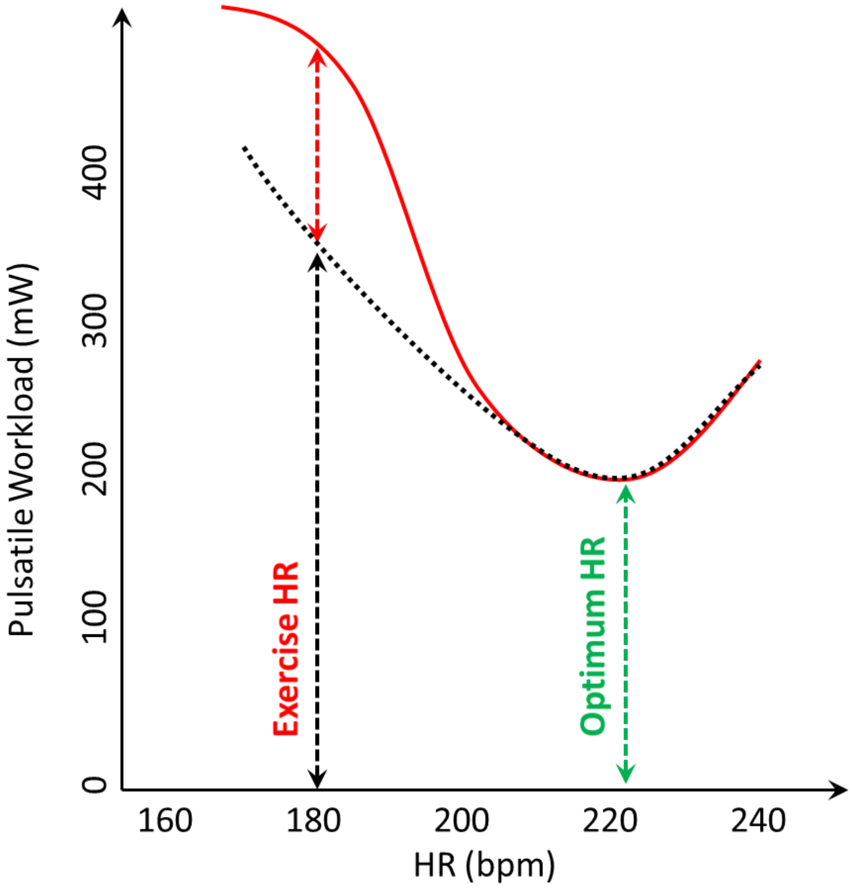

Figure 9.8: Black dotted curve is an example of pulsatile workload on the heart with a pathological wave condition during exercise showing that when the exercise HR is shifted away from the optimum HR the workload on the heart is increased. Red solid curve is an example of pathological wave condition accompanied by a destructive resonance. In this case the pulsatile workload at the exercise HR is increased further.

Any cardiovascular abnormality can enhance the opposing coronary waves (W_3 and W_4) or weaken the assisting coronary waves (W_1 and W_2) resulting in coronary blood flow reduction (pathological coronary waves). In the absence of cardiovascular diseases, the pathological coronary waves can occur if a constructive resonance occurs for the opposing wave or/and a destructive resonance forms for the assisting waves. These resonances can simply happen if the timing of the waves is not right. Figure 9.9 schematically demonstrates the effect of pathological coronary waves on coronary blood flow.

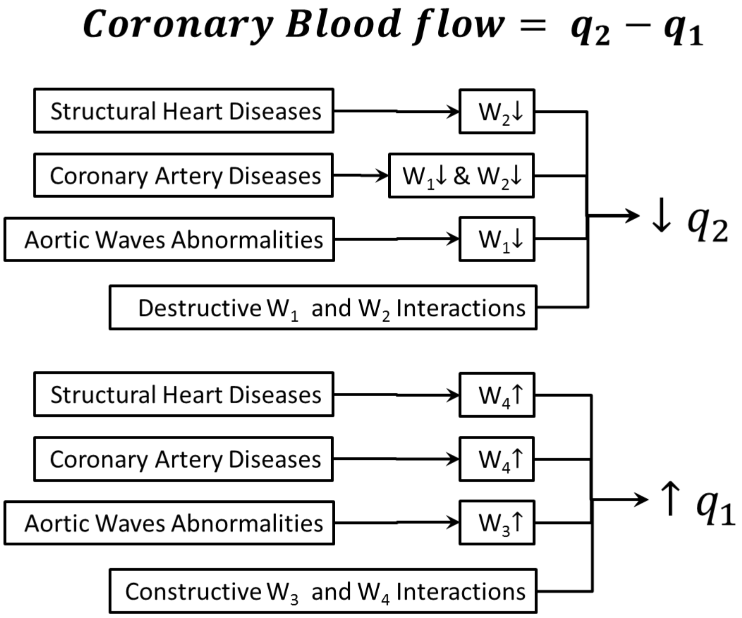

Figure 9.9: Formation of pathological coronary waves and consequent reduction of the coronary blood flow. q_1, q_2, W_1, W_2, W_3, and W_4 are the same as described in Figure 9.2.

9.5.3 Pathological Wave Dynamics and Sudden Cardiac Death

The cardiovascular system operates close to its limit during the exercise. The presence of any structural abnormalities may lower the threshold for the onset of acute ischemia and/or ventricular fibrillation. Therefore, formation of pathological waves significantly increases the chance of SCD in athletes with structural cardiovascular diseases. However, both pathological aortic waves and pathological coronary waves can be created without any structural abnormalities. This is probably the case when SCD happens for athletes with no cardiovascular diseases (21% of SCD equal to 3.4% of all sudden death in athletes)[133].

Aside from their own negative effect on cardiovascular functioning, each cardiovascular disease can alter the dynamics of the heart-aorta-coronary system and create pathological waves. In this situation, pathological waves are acting as a trigger helping the preexisting poor conditions to initiate SCD during exercise. As stated in the introduction section, various cardiovascular diseases have been observed and reported as underlying causes of SCD in athletes. Some of them have been observed frequently, such as cardiomyopathies and coronary diseases, and some have been rarely reported, such as right ventricular dysplasia [135].

In hypertrophic heart diseases such as HCM and LVH, the coronary blood flow (CBF) is impaired due to abnormalities of both W_2 and W_4 waves (see Figure 9.2) that are generated at the myocardial end of the coronary arteries. The reduced CBF results in acute ischemia of the diseased heart, initiating sudden cardiac death during exercise. Under DCM conditions, the mechanism is slightly different as only the W_2 wave contributes toward reduction of CBF. However, due to the abnormality of the left ventricular flow wave, there is a possibility of the formation of pathological aortic waves which can enhance LV workload. The aortic compression waves (W_2) get impaired in coronary arterial origin anomaly diseases. This situation further decreases the already reduced CBF and initiates SCD. Similarly, abnormal coronary wave interaction caused by atherosclerotic coronary artery diseases decreases CBF promoting acute ischemia and death during exercise. The plausible mechanism of SCD in athletes with aortic stenosis (AS) is as follows: The myocardial workload is abnormally high in AS athletes. AS also causes formation of pathological aortic waves. These abnormal waves adversely affect coronary waves and consequently reduce CBF. The combination of the elevated myocardial workload and reduced CBF initiate SCD in athletes with AS disease. Figure 9.10 graphically demonstrates the heart diseases and possible formation of pathological waves that are acting as the final component for the initiation of SCD. Figure 9.11 shows how waves can cause SCD in the absence of any cardiovascular diseases. It must be mentioned that increasing workload and reducing coronary blood flow is not the only mechanism through which pathological waves can trigger or cause SCD. Pathological waves can cause aneurysm rupture or aortic rupture (e.g. in Marfan syndrome) by creating resonance in radial wall dilation waves that propagate on the vessel wall.

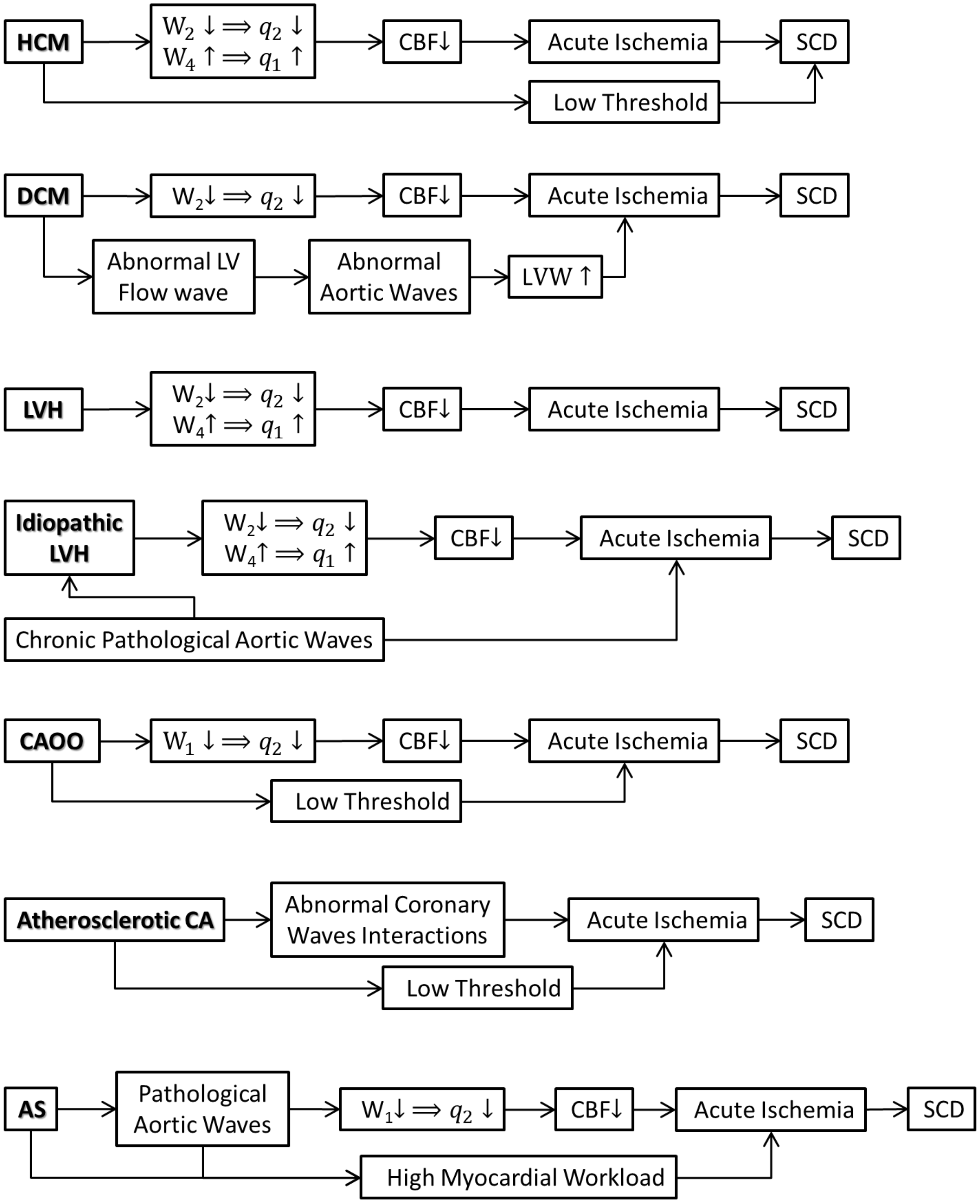

Figure 9.10: Cardiovascular diseases and pathological waves. CBF: coronary blood flow; HCM: hypertrophic cardiomyopathy; DCM: dilated cardiomyopathy; LVW: Left ventricular workload; LVH: Left ventricle hypertrophy; CAOA: coronary arterial origin anomalies; CA: coronary arteries; AS: aortic stenosis. See Figure 9.2 for explanation of q_1, q_2, W_1, W_2, W_3, and W_4.

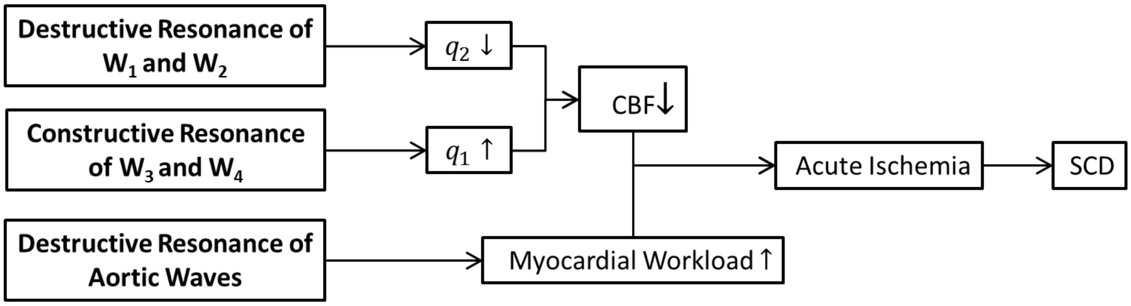

Figure 9.11: Pathological waves as the main cause of SCD in athletes in the absence of structural pathologies. See Figure 9.2 for explanation of q_1, q_2, W_1, W_2, W_3, and W_4.

9.5.4 Commotio Cordis, Pathological Waves, and Sudden Cardiac Death

Commotio cordis is defined as sudden death due to non-penetrating impact on the chest without any structural injuries. Commotio cordis is a rare event and the percentage of commotio cordis survivors is extremely low [139]. The true mechanism(s) of death in commotio cordis is not known, but several hypotheses have been proposed such as the disturbing of the electrical rhythm of the heart which initiate the fatal VF and trauma-induced coronary vasospasm that causes acute ischemia initiating VF [139].

This pathological wave hypothesis is able to provide a plausible explanation for Commotio Cordis. When the projectile impact hits the chest wall where it overlays the heart, it creates a vibrational wave propagating toward coronary arteries and the ascending aorta. As the vibrational waves reach the wall of the aorta and coronary arteries, they act as pinchers displacing the vessel wall. Similar to an impedance pump, these pinchers are creating additional waves propagating in the aorta and coronary arteries. If the new wave dynamics interact destructively with the existing wave dynamics (before the impact), a sudden jump in heart workload and a sudden reduction in coronary blood flow occur. Under this condition severe acute ischemia happens, which may initiate the deadly VF. The fact that commotio cordis only occurs in children and young adults who have a more pliable chest wall [139] supports this hypothesis. Figure 9.12 shows a schematic of this phenomenon.

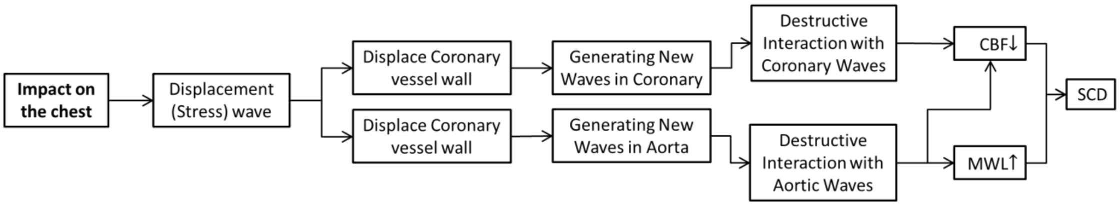

Figure 9.12: The plausible mechanism of SCD in Commotio Cordis through formation of pathological wave dynamics. CBF: coronary blood flow; MWL: myocardial workload.

9.6 Hypothesis Summary

Pathology in the wave dynamics could be the missing element in understanding the cause of sudden cardiac death during exercise. In summary, when the interaction of hemodynamic waves (pressure wave, flow wave, and wall displacement wave) is abnormal during exercise, the myocardial oxygen demand can exceed the oxygen delivery, hence creating acute ischemia which leads to VF and death.

It was explained how increased oxygen demand may be the result of pathological aortic waves while reduced oxygen delivery is mainly due to pathological coronary waves. Preexisting cardiovascular diseases such as HCM, LVH, and CAD can worsen the oxygen demand/delivery balance and/or reduce the threshold for the initiation of the SCD. Abnormal wave interactions can create resonance in the wall displacement wave at the origin of the vessel which can cause rupture in athletes with aneurysms and Marfan syndrome, a scenario that has not been discussed here.

9.6.1 Clinical Perspective

It has been shown that the mammalian cardiovascular system is designed to operate in an optimal condition [58, 79, 97, 98, 102]. Although most of the past studies have considered the resting condition, a suboptimal condition during intense activity (e.g. fight or exercise) has its own optimum operating point. Preserving an optimal condition across all mammals with different cardiac output, heart rate, and body length strongly support this theory.

For that reason, it is logical to assume that the existence of a non-optimal condition at rest indicates a non-optimal condition during exercise. The existence of pathological waves in a resting condition, although they are not deadly, implies the existence of pathological waves during exercise when they become dangerous. Therefore, screening athletes during rest to detect abnormal wave dynamics could be a starting point in preventing sudden cardiac death during exercise.

9.6.2 Future Studies

The first step would be to detect the signatures of all abnormal wave conditions as it has been done by Davies *et al* [92] and Pahlevan *et al* [119](also see Chapter 3). This would enable physicians to screen athletes and select those who suffer from pathological wave during rest. These athletes are probably in high risk of having this dynamic pathology during exercise as well. Therefore, recording athletes' waveforms at rest could help prevent future incidence. Designing animal studies to investigate the pathological waves and sudden cardiac death hypothesis is a necessary step toward the prevention of SCD in athletes. In addition, multiscale computational modeling of the heart and coronary arteries could help detect the pathological wave signatures and move toward solving this problem.

Appendix A

IMPACT OF WAVE SPEED ESTIMATION ON REFLECTED WAVE INTENSITY COMPUTATION

A.1 Wave Speed and Reflected Wave Intensity (RWI)

There is no question that wave speed calculated from the PU-loop method, Foot-to-Foot method, or any other analytical formulation is not exact. However, this does not influence the pattern of wave intensity significantly. Figure A1 shows samples of RWI calculated with a wave speed computed from PU-loop method (blue), wave speed containing +6% error (red), and wave speed containing 6% error (black). This figure shows that the RWI pattern is well preserved.

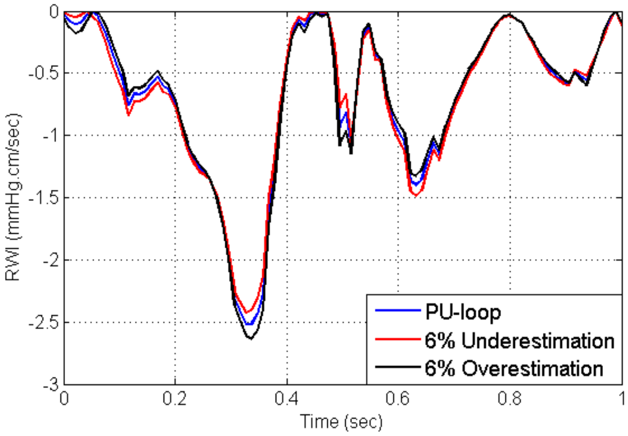

Figure A1: Effect of wave speed error on reflected wave intensity pattern

It has been also shown by Khir *et al* [44] that even a 20% error in the calculation of the wave speed does not significantly change the pattern of the reflected wave intensity.

Appendix B

EFFECT OF AORTIC RIGIDITY AND HEART RATE ON REFLECTED WAVE INTENSITY

B.1 Aortic Rigidity and Reflected Wave Intensity (RWI)

Figure B1 demonstrates that the WI of the reflected (backward) waves increases at higher rigidities, and that the first peak of the wave intensity shifts towards the beginning of the cardiac cycle. This shift was expected since reflected waves arrive earlier due to higher wave speed at higher rigidities [7, 12]. This figure shows that at higher rigidities the reflected waves come back earlier with higher intensity amplitudes. The higher amplitude of RWI indicates that the reflected waves are carrying more energy.

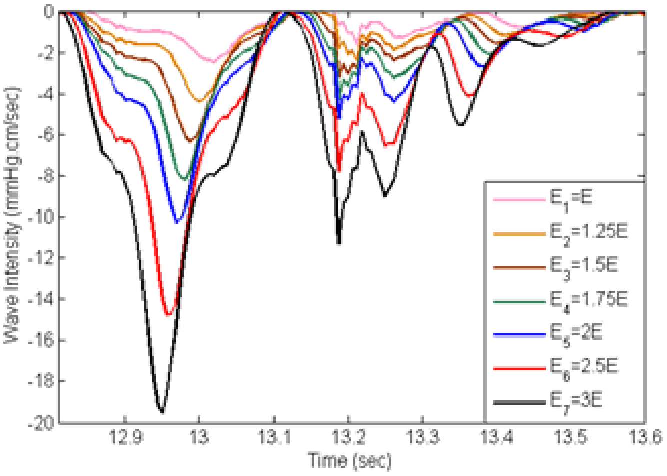

Figure B1: Wave intensity of reflected waves at the aortic input during a complete cardiac cycle. The length of the incremental time interval for calculating dI_- was taken to be $dt = 0.00625$ *sec*. Different colors in the legend correspond to the different levels of aortic rigidities. The value of E_1-E_7 corresponds to the values given in Chapter 3. The results are for HR = 75 bpm.

B.2 Heart Rate and Reflected Wave Intensity (RWI)

As HR increased, the backward WI decreased and the peak of the WI shifted to a later point in the cycle. This shift was a natural consequence of the normalization to the period of the cardiac cycle. Since the location of the reflection sites and the wave speeds were the same, the shortened length of the period for higher HR delayed the arrival time of the backward waves within the time-normalized cycle. With a fixed cardiac output, the amplitude of the reflected WI decreases as the HR increases since stroke volume decreases. Therefore, reflected waves contain higher energy and show higher amplitude in their WI at lower HR (Figure B2).

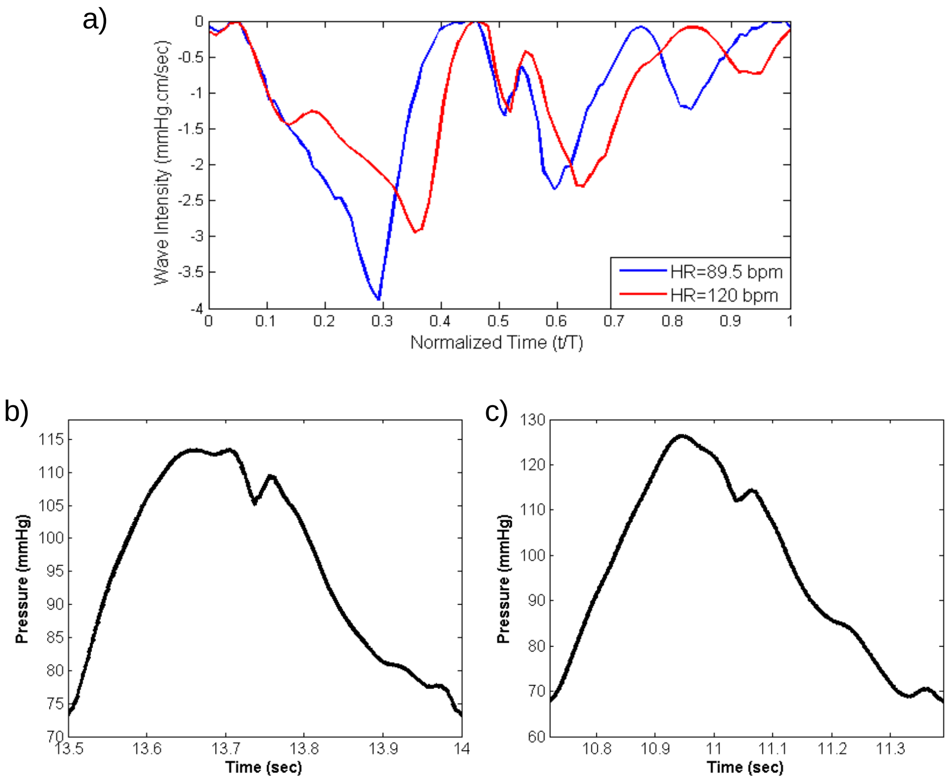

Figure B2: a) Wave intensity of reflected waves at the aortic input during a complete cardiac cycle. Three distinct peaks are observed for both cases. The time was normalized with the cardiac period (T). Blue is for HR=89.5 bpm and red is for HR=120 bpm. Both curves correspond to the same aortic rigidity (E_2). The length of the incremental time interval for calculating dI- was taken to be $dt = 0.00625\ s$. b) Aortic input pressure for HR=120 bpm for aortic rigidity of E_2 . c) Aortic input pressure for HR=89.5 bpm for aortic rigidity of E_2. The value of E_2 corresponds to the values given in Chapter 3.

Figure B3a shows the reflected wave intensities of HR=100 and HR=150 bpm for the case of aortic rigidity of E_1. Figures B3b, 3c show the aortic input pressure of HR=100 and HR=150 bpm respectively. Because of the destructive interactions of reflected waves under these conditions (see Chapter 3 for more details), in contrast to the previous case, higher HR was found to be associated with higher pulsatile power ($\overline{P}_{pulse}(HR=100) < \overline{P}_{pulse}(HR=150)$) although due to higher stroke volume waves are carrying more energy.

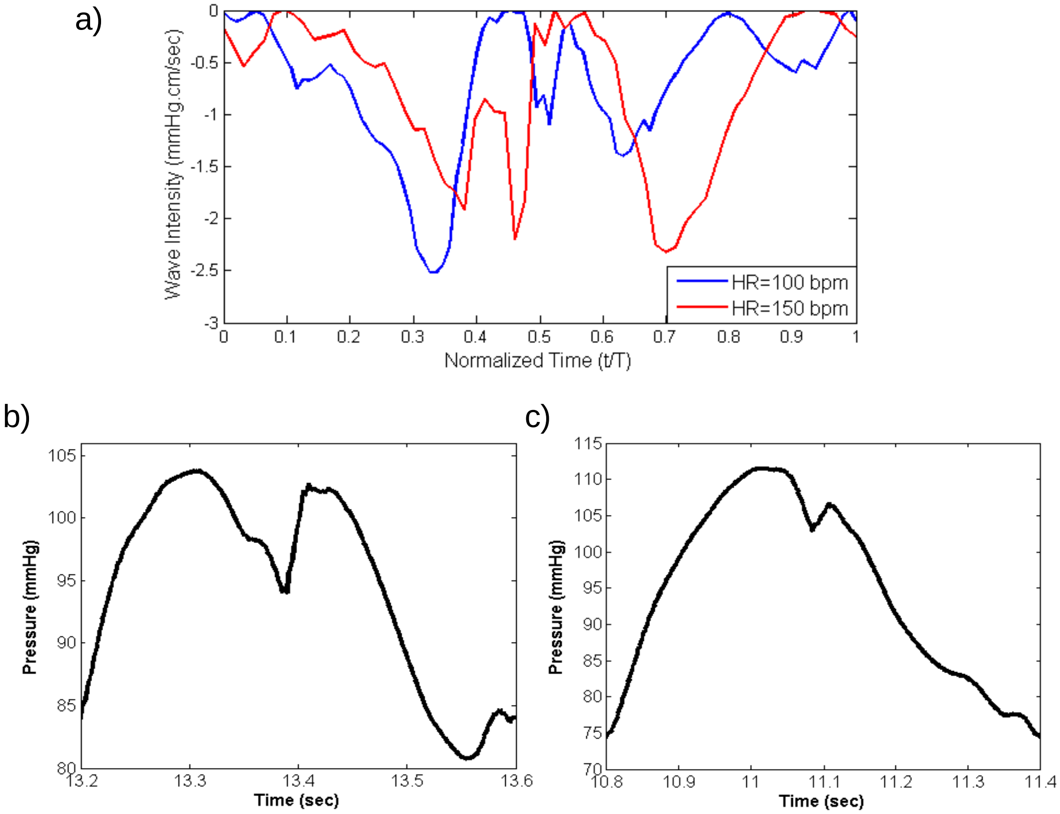

Figure B3: Wave intensity of reflected waves at the aortic input during a complete cardiac cycle. The time was normalized with the cardiac period (*T*). Blue is for HR=100 bpm and red is for HR=150 bpm. Both curves correspond to the same aortic rigidity (E_1). There are three peaks for HR=150, but only two for HR=150. The length of the incremental time interval for calculating dI_- was taken to be $dt = 0.00625\ s$. b) Aortic input pressure for HR=150 bpm for aortic rigidity of E_1. c) Aortic input pressure for HR=100 bpm for aortic rigidity of E_1. The value of E_1 corresponds to the values given in Chapter 3.

Appendix C

WAVE ENERGY AS A FUNCTION OF PISTON PUMP STROKE RATE

C.1 Derivation of a Single Harmonic

A single harmonic flow wave in an elastic tube can be written in the form of [12]

$$q = q_0 h \cos\left(2\pi f \left(t - \frac{x}{c}\right)\right). \tag{C1}$$

Here, *f* is the frequency of the wave, *c* is the wave speed (which depends on material properties and frequency), and q_0 is the wave amplitude in the absence of wave reflections. *h* depends on the system and is a function of the tube's material properties, fluid density, fluid viscosity, and tube diameter. In the case of an elastic tube and a piston pump, f becomes the frequency of the piston (f_p) and q_0 will be the amplitude of the piston stroke rate (*St*). Hence, Equation (*C1*) takes the form of

$$q = (St) h \cos\left(2\pi f_p \left(t - \frac{x}{c}\right)\right). \tag{C2}$$

For any wave with a mechanical nature, the energy rate (power) is proportional to the product of the spatial derivative and time derivative of the wave [140]. Using Equation (*C2*) the time-averaged power carried by the piston generated flow wave is proportional to

$$\bar{P} \propto \frac{1}{T}\int_0^T \frac{dq}{dt}\frac{\partial q}{\partial x}dt \propto \frac{1}{T}\int_0^T f_p St\, h\ \sin 2\pi f_p\left(t - \frac{x}{c}\right) \frac{f_p}{c} St\, h\ \sin 2\pi f_p\left(t - \frac{x}{c}\right) dt\ ,$$

$$\xrightarrow{yields} \boxed{\bar{P} \propto St^2 \frac{h^2 f_p^2}{c}}\ , \tag{C3}$$

where, T is the period of one cycle and $\bar{P}$ is the average power over a cycle. At a fixed piston frequency for the same compliant aorta and circulating fluid (*h* and *c* remain constant), it can be concluded from Equation *C3* that the energy carried by the wave is proportional to the square of the stroke rate ($\bar{P} \propto St^2$).

Appendix D

SPARSE TIME-FREQUENCY REPRESENTATION

D.1 Introduction

Signals and data are the most direct ways to get information about the real world. Most of the data that we deal with in studying the natural phenomena are nonlinear and non-stationary in nature. As a result, it is of great importance to develop a truly adaptive signal analysis method that can be applied to extract hidden physical information from these nonlinear and non-stationary data. Many traditional data analysis methods are designed to process data. Fourier analysis and wavelet analysis are two of the most commonly used methods for this purpose. An important feature of these traditional data analysis methods is that a pre-determined basis and well-established discrete fast transforms are used (Fast Fourier Transform and Fast Wavelet Transform) to perform data analysis. Thus these methods can be implemented very efficiently. On the other hand, since these methods are pre-determined, they are not very effective in dealing with nonlinear and non-stationary data. In the past decade, there has been an increasing interest in developing new adaptive data analysis methods that can handle non-linear and non-stationary data effectively [132]. Inspired by the Empirical Decomposition Method (EMD)[127], a new adaptive method of Sparse Time-Frequency Representation (STFR) was introduced [128, 129].

D.2 Adoptive Sparse Time-Frequency Representation (STFR) Method

The adaptive STFR method consists of two major steps. The first step is to construct a highly redundant dictionary of all IMFs, *D*. The second step is to find the sparsest decomposition by solving a nonlinear optimization problem:

$$Minimize \qquad M$$

$$Subject\ to\colon\ s(t)=\sum_{i=1}^{M}a_i(t)\cos\theta_i(t),\quad a_i(t)\cos\theta_i(t)\in D,\qquad (i=1,\dots,M). \qquad (D1)$$

This problem is an L_0 minimization problem. Solving this problem is extremely difficult. It is a non-linear and non-convex optimization problem [128, 129]. To overcome this difficulty, a nonlinear matching pursuit method is proposed to approximate the original L_0 minimization problem. Based on an approximation, the STFR method can be reduced to a L_2 minimization problem [129]. A brief description of this algorithm is provided below:

$$minimize \qquad \|f(t)-a(t)\cos\theta(t)\|_2^2 \qquad (D2)$$

$$subject\ to\colon \qquad a(t)\cos\theta(t)\in D. \qquad (D3)$$

In this formulation, the dictionary *D* is defined as

$$D=\left\{a(t)\cos\theta(t)\colon\ \frac{d\theta}{dt}=\dot{\theta}(t)\geq 0,\qquad a(t),\dot{\theta}(t)\in V(\theta)\right\}. \qquad (D4)$$

Where, $V(\theta)$ is a linear space consisting of functions smoother than $\cos\theta(t)$:

$$V(\theta)=span\left\{1, cos\left(\frac{k\theta}{2L_\theta}\right), sin\left(\frac{k\theta}{2L_\theta}\right), k=1,\dots,L_\theta\right\}. \qquad (D5)$$

More detail about the dictionary, *D,* can be found in Hou *et al* [129].

At any step of the algorithm, an IMF is extracted. The residual is treated as a new signal and the L_2 minimization is again applied to the residual. By this nonlinear matching pursuit method, one can extract the different scales of a multiscale, non-stationary and nonlinear signal [129].

Appendix E

BRUTE-FORCE ALGORITHM FOR CARDIOVASCULAR INTRINSIC FREQUENCY

E.1 Brute-force Algorithm

In order to solve the modified STRF problem, a brute-force algorithm was used. First, the domain *D* was taken as

$$D = \{(\omega_1, \omega_2)\ such\ that\ 0 < \omega_1, \omega_2 \leq C\ \} \qquad (E1)$$

In domain *D*, the frequencies ω_1, ω_2 are bounded above by some constant *C*. This is a valid assumption since the aortic pressure wave signal has a certain level of smoothness, and the signal is not rough; therefore, certain frequencies cannot be accepted physically and mathematically as the solution of the problem.

Next, we discretize *D* for pairs of (ω_1, ω_2). For each point (ω_1, ω_2) in the discretized domain, the modified STFR problem is solved and the solution is stored as $P(\omega_1, \omega_2)$. Note that the minimum of the modified STFR problem for the whole domain D corresponds to the minimum of $P(\omega_1, \omega_2)$ over (ω_1, ω_2); this is a simple search problem. The corresponding minimum frequencies are denoted as $(\omega_1, \omega_2)_m$. The original minimization problem is not convex. Thus we may have several local minima. However, the brute-force algorithm looks over all possible values of frequencies and ensures that the corresponding minimizer frequencies $(\omega_1, \omega_2)_m$ are in fact the unique global minimizer. Figure E1 shows all value of $P(\omega_1, \omega_2)$ for a sample pressure wave. The global minimizer is shown by a black triangle.

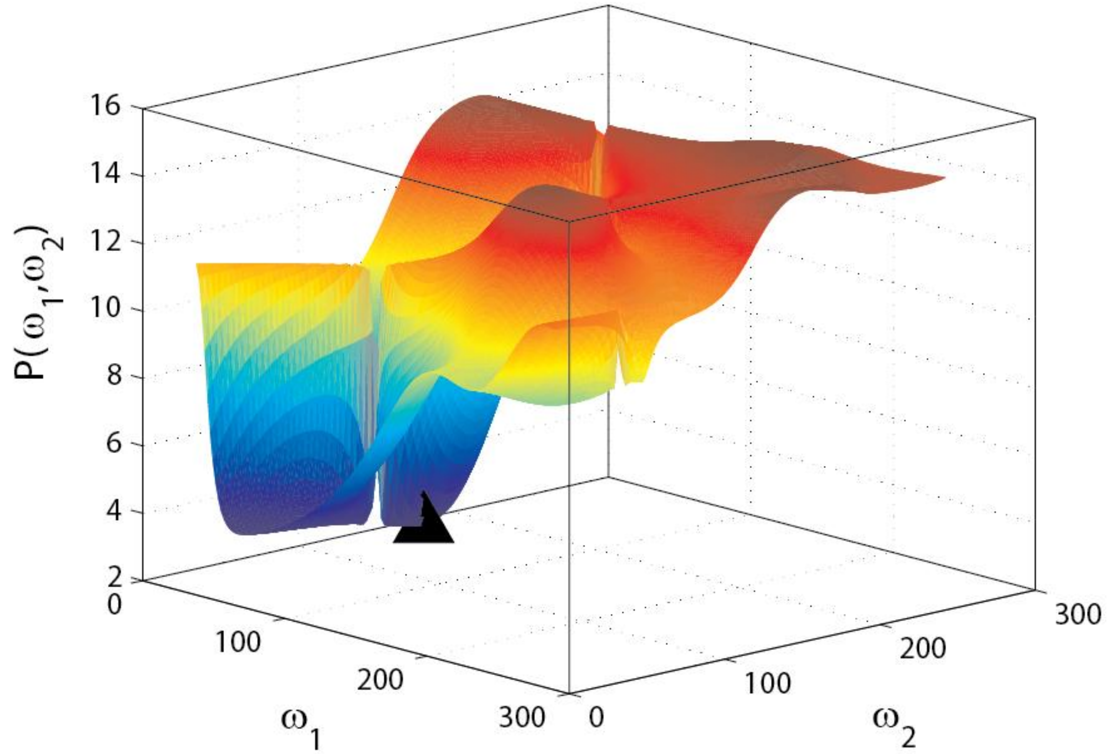

Figure E1: Brute-force algorithm applied on sample pressure waves in order to calculate the intrinsic frequencies (ω_1, ω_2). The black triangle is the global minimizer that gives cardiovascular intrinsic frequencies.

BIBLIOGRAPHY

1. WRITING GROUP MEMBERS, Lloyd-Jones D, Adams RJ, Brown TM, Carnethon M, Dai S, De Simone G, Ferguson TB, Ford E, Furie K, Gillespie C, Go A, Greenlund K, Haase N, Hailpern S, Ho PM, Howard V, Kissela B, Kittner S, Lackland D, Lisabeth L, Marelli A, McDermott MM, Meigs J, Mozaffarian D, Mussolino M, Nichol G, Roger VL, Rosamond W, Sacco R, Sorlie P, Stafford R, Thom T, Wasserthiel-Smoller S, Wong ND, Wylie-Rosett J, Committee obotAHAS, Stroke Statistics Subcommittee. Heart disease and stroke statistics--2010 update: A report from the American Heart Association. *Circulation*. 2010;121:e46-215
2. Petrasek D. Systems biology: The case for a systems science approach to diabetes. *Journal of Diabetes Science and Technology (Online)*. 2008;2:131
3. Berne R, Levy M, Koeppen B, Tanton B. Textbook of physiology. *Philadephia: Mosby*. 2004
4. Parker S, Winston R. *The human body book*. Dorling Kindersley; 2007.
5. Pedley TJ. *Fluid Mechanics of Large Blood Vessels*. Cambridge University Press 1995
6. Caro CG, Pedley JG, Schroter RC, Seed WA. *The Mechanics of the Circulation*. Oxford: Oxford University Press; 1978.
7. Nichols WW, O'Rourke MF. *Mcdonald's blood flow in arteries: Theoretical, Experimental and Clinical Principles*. London: Arnold; 1998.
8. Avrahami I, Gharib M. Computational studies of resonance wave pumping in compliant tubes. *Journal of Fluid Mechanics*. 2008;608:139-160
9. Hickerson A, Rinderknecht D, Gharib M. Experimental study of the behavior of a valveless impedance pump. *Experiments in Fluids*. 2005;38:534-540
10. Hickerson AI, Gharib M. On the resonance of a pliant tube as a mechanism for valveless pumping. *Journal of Fluid Mechanics*. 2006;555:141-148
11. Meier JA. A novel experimental study of a valveless impedance pump for applications at lab-on-chip, microfluidic, and biomedical device size scales. 2011; Thesis Ph.D, California Institute of Technology, California, US.
12. Zamir M. *The physics of pulsatile flow*. New York: Springer-Verlag; 2000.
13. Liebau G. On a valveless pump principle (ger). *Naturwissenschaften*. 1954:327
14. Korteweg D. Ueber die fortpflanzungsgeschwindigkeit des schalles in elastischen röhren. *Annalen der Physik*. 1878;5:525-542
15. Morgan GW, Kiely JP. Wave propagation in a viscous liquid contained in a flexible tube. *The Journal of the Acoustical Society of America*. 1954;26:323-328
16. Womersley JR. Oscillatory flow in arteries: The constrained elastic tube as a model of arterial flow and pulse transmission. *Physics in Medicine and Biology*. 1957;2:178
17. Liebau G. Über periphere blutförderung. *Phenomen der pulsierenden Strömung im Blutkreislauf aus technologischer, physiologischer und klinischer Sicht.* Mannheim, Wien, Zürich: Bibliographisches Institut. 1970:67-78
18. Loumes L, Avrahami I, Gharib M. Resonant pumping in a multilayer impedance pump. *Physics of Fluids*. 2008;20:023103
19. Ottesen JT. Valveless pumping in a fluid-filled closed elastic tube-system: One-dimensional theory with experimental validation. *Journal of Mathematical Biology*. 2003;46:309-332

20. Forouhar AS, Liebling M, Hickerson A, Nasiraei-Moghaddam A, Tsai H-J, Hove JR, Fraser SE, Dickinson ME, Gharib M. The embryonic vertebrate heart tube is a dynamic suction pump. *Science*. 2006;312:751-753
21. De Pater L, van den Berg J. An electrical analogue of the entire human circulatory system. *Medical and Biological Engineering and Computing*. 1964;2:161-166
22. Noordergraaf A, Verdouw PD, Boom HBK. The use of an analog computer in a circulation model. *Progress in Cardiovascular Diseases*. 1963;5:419-439
23. Westerhof N, Bosman F, De Vries CJ, Noordergraaf A. Analog studies of the human systemic arterial tree. *Journal of Biomechanics*. 1969;2:121-134, IN121, 135-136, IN123, 137-138, IN125, 139-143
24. Grinberg L, Karniadakis G. Outflow boundary conditions for arterial networks with multiple outlets. *Annals of Biomedical Engineering*. 2008;36:1496-1514
25. Vignon-Clementel IE, Figueroa CA, Jansen KE, Taylor CA. Outflow boundary conditions for 3d simulations of non-periodic blood flow and pressure fields in deformable arteries. *Computer Methods in Biomechanics and Biomedical Engineering*. 2010;13:625-640
26. Sherwin SJ, Franke V, Peiró J, Parker K. One-dimensional modelling of a vascular network in space-time variables. *Journal of Engineering Mathematics*. 2003;47:217-250
27. Taylor CA, Draney MT, Ku JP, Parker D, Steele BN, Wang K, Zarins CK. Predictive medicine: Computational techniques in therapeutic decision-making. *Computer Aided Surgery*. 1999;4:231-247
28. Stergiopulos N, Young DF, Rogge TR. Computer simulation of arterial flow with applications to arterial and aortic stenoses. *Journal of Biomechanics*. 1992;25:1477-1488
29. O'Rourke MF, Nichols WW. Aortic diameter, aortic stiffness, and wave reflection increase with age and isolated systolic hypertension. *Hypertension*. 2005;45:652-658
30. Olufsen MS. Structured tree outflow condition for blood flow in larger systemic arteries. *Am J Physiol Heart Circ Physiol*. 1999;276:H257-268
31. Vignon-Clementel IE, Alberto Figueroa C, Jansen KE, Taylor CA. Outflow boundary conditions for three-dimensional finite element modeling of blood flow and pressure in arteries. *Computer Methods in Applied Mechanics and Engineering*. 2006;195:3776-3796
32. Avolio A. Ageing and wave reflection. *Journal of Hypertension*. 1992;10:S83-S86
33. Franklin SS, Weber MA. Measuring hypertensive cardiovascular risk: The vascular overload concept. *American Heart Journal*. 1994;128:793-803
34. Laskey W, Kussmaul W. Arterial wave reflection in heart failure. *Circulation*. 1987;75:711-722
35. Laurent S, Boutouyrie P, Asmar R, Gautier I, Laloux B, Guize L, Ducimetiere P, Benetos A. Aortic stiffness is an independent predictor of all-cause and cardiovascular mortality in hypertensive patients. *Hypertension*. 2001;37:1236-1241
36. London GM, Blacher J, Pannier B, Guerin AP, Marchais SJ, Safar ME. Arterial wave reflections and survival in end-stage renal failure. *Hypertension*. 2001;38:434-438
37. Mitchell GF, Tardif J-C, Arnold JMO, Marchiori G, O'Brien TX, Dunlap ME, Pfeffer MA. Pulsatile hemodynamics in congestive heart failure. *Hypertension*. 2001;38:1433-1439
38. Self DA, Ewert DL, Swope RD, Crisman RP, Latham RD. Beat-to-beat determination of peripheral resistance and arterial compliance during +Gz centrifugation. *Aviat Space Environ Med*. 1994;65:396-403
39. Stergiopulos N, Meister JJ, Westerhof N. Simple and accurate way for estimating total and segmental arterial compliance: The pulse pressure method. *Annals of Biomedical Engineering*. 1994;22:392-397
40. Stergiopulos N, Meister JJ, Westerhof N. Evaluation of methods for estimation of total arterial compliance. *Am J Physiol Heart Circ Physiol*. 1995;268:H1540-1548

41. Parker KH, Jones CJH. Forward and backward running waves in the arteries: Analysis using the method of characteristics. *Journal of Biomechanical Engineering*. 1990;112:322-326
42. Anliker M, Rockwell RL, Ogden E. Nonlinear analysis of flow pulses and shock waves in arteries. *Zeitschrift für Angewandte Mathematik und Physik (ZAMP)*. 1971;22:217-246
43. Parker KH, Jones CJH, Dawson JR, Gibson DG. What stops the flow of blood from the heart? *Heart and Vessels*. 1988;4:241-245
44. Khir AW, O'Brien A, Gibbs JSR, Parker KH. Determination of wave speed and wave separation in the arteries. *Journal of biomechanics*. 2001;34:1145-1155
45. Koh TW, Pepper JR, DeSouza AC, Parker KH. Analysis of wave reflections in the arterial system using wave intensity: A novel method for predicting the timing and amplitude of reflected waves. *Heart and Vessels*. 1998;13:103-113
46. Fung YC. *Biomechanics of the circulation*. New York, NY: Springer-Verlag; 1997.
47. Whitaker S. *Introduction to fluid mechanics*. Krieger Pub Co.; 1992.
48. Bathe KJ. *Finite element procedures*. Prentice-Hall; 2006.
49. ADINA R&D I. *Theory and modeling guide, volume i: ADINA solids & structures*. Watertown, MA; 2009.
50. ADINA R&D I. *Theory and modeling guide, volume iii: ADINA CFD & FSI*. Watertown, MA; 2009.
51. Bathe KJ, Zhang H, Wang MH. Finite element analysis of incompressible and compressible fluid flows with free surfaces and structural interactions. *Computers & Structures*. 1995;56:193-213
52. Bathe KJ, Zhang H, Zhang X. Some advances in the analysis of fluid flows. *Computers & Structures*. 1997;64:909-930
53. Bathe M, Kamm RD. A fluid-structure interaction finite element analysis of pulsatile blood flow through a compliant stenotic artery. *Journal of Biomechanical Engineering*. 1999;121:361-369
54. Bathe K-J, Hou Z, Ji S. Finite element analysis of fluid flows fully coupled with structural interactions. *Computers & Structures*. 1999;72:1-16
55. Bathe K-J, Zhang H. Finite element developments for general fluid flows with structural interactions. *International Journal for Numerical Methods in Engineering*. 2004;60:213-232
56. Zhang H, Bathe K-J. Direct and iterative computing of fluid flows fully coupled with structures. *Computational Fluid and Solid Mechanics*. 2001:1440-1443
57. Matthys KS, Alastruey J, Peiro J, Khir AW, Segers P, Verdonck PR, Parker KH, Sherwin SJ. Pulse wave propagation in a model human arterial network : Assessment of 1-d numerical simulations against in vitro measurements. *Journal of Biomechanics*. 2007;40:3476-3486
58. Milnor WR. *Haemodynamics*. Baltimore, Md: Williams & Wilkins Co; 1989.
59. Curtis SL, Zambanini A, Mayet J, McG Thom SA, Foale R, Parker KH, Hughes AD. Reduced systolic wave generation and increased peripheral wave reflection in chronic heart failure. *Am J Physiol Heart Circ Physiol*. 2007;293:H557-562
60. Hashimoto J, Nichols WW, O'Rourke MF, Imai Y. Association between wasted pressure effort and left ventricular hypertrophy in hypertension: Influence of arterial wave reflection. *Am J Hypertens*. 2008;21:329-333
61. Mitchell GF, Hwang S-J, Vasan RS, Larson MG, Pencina MJ, Hamburg NM, Vita JA, Levy D, Benjamin EJ. Arterial stiffness and cardiovascular events: The Framingham Heart Study. *Circulation*. 2010;121:505-511

62. Mitchell GF, Parise H, Benjamin EJ, Larson MG, Keyes MJ, Vita JA, Vasan RS, Levy D. Changes in arterial stiffness and wave reflection with advancing age in healthy men and women: The Framingham Heart Study. *Hypertension*. 2004;43:1239-1245
63. Ooi H, Chung W, Biolo A. Arterial stiffness and vascular load in heart failure. *Congestive Heart Failure*. 2008;14:31-36
64. Williams B, Lacy PS. Central haemodynamics and clinical outcomes: Going beyond brachial blood pressure? *European Heart Journal*. 2010;31:1819-1822
65. O'Rourke MF. Steady and pulsatile energy losses in the systemic circulation under normal conditions and in simulated arterial disease. *Cardiovascular Research*. 1967;1:313-326
66. Safar M, O'Rourke MF. *Arterial stiffness in hypertension*. Elsevier; 2006.
67. Rinderknecht D, Hickerson AI, Gharib M. A valveless micro impedance pump driven by electromagnetic actuation. *Journal of Micromechanics and Microengineering*. 2005;15:861-866
68. Saito GE, Vander Werff TJ. The importance of viscoelasticity in arterial blood flow models. *Journal of biomechanics*. 1975;8:237-245
69. Pahlevan N, Amlani F, Hossein Gorji M, Hussain F, Gharib M. A physiologically relevant, simple outflow boundary model for truncated vasculature. *Annals of Biomedical Engineering*. 2011;39:1470-1481
70. Manisty CH, Zambanini A, Parker KH, Davies JE, Francis DP, Mayet J, McG Thom SA, Hughes AD, on behalf of the Anglo-Scandinavian Cardiac Outcome Trial Investigators. Differences in the magnitude of wave reflection account for differential effects of amlodipine- versus atenolol-based regimens on central blood pressure: An Anglo-Scandinavian Cardiac Outcome Trial Substudy. *Hypertension*. 2009;54:724-730
71. Chae CU, Pfeffer MA, Glynn RJ, Mitchell GF, Taylor JO, Hennekens CH. Increased pulse pressure and risk of heart failure in the elderly. *JAMA*. 1999;281:634-643
72. Franklin SS, Lopez VA, Wong ND, Mitchell GF, Larson MG, Vasan RS, Levy D. Single versus combined blood pressure components and risk for cardiovascular disease: The Framingham Heart Study. *Circulation*. 2009;119:243-250
73. Burattini R, Knowlen G, Campbell K. Two arterial effective reflecting sites may appear as one to the heart. *Circ Res*. 1991;68:85-99
74. Lloyd-Jones DM, Larson MG, Leip EP, Beiser A, D'Agostino RB, Kannel WB, Murabito JM, Vasan RS, Benjamin EJ, Levy D. Lifetime risk for developing congestive heart failure: The Framingham Heart Study. *Circulation*. 2002;106:3068-3072
75. Moser M, Hebert P. Prevention of disease progression, left ventricular hypertrophy and congestive heart failure in hypertension treatment trials. *J Am Coll Cardiol*. 1996;27:1214-1218
76. Matthys KS, Alastruey J, Peiro J, Khir AW, Segers P, Verdonck PR, Parker KH, Sherwin SJ. Pulse wave propagation in a model human arterial network : Assessment of 1-d numerical simulations against in vitro measurements. *Journal of Biomechanics*. 2007;40:11
77. Pahlevan NM, Amlani F, Gorji H, Hussain F, Gharib M. A physiologically relevant, simple outflow boundary model for truncated vasculature. *Annals of Biomedical Engineering*. 2011;39:1470-1481
78. Kelly R, Tunin R, Kass D. Effect of reduced aortic compliance on cardiac efficiency and contractile function of in situ canine left ventricle. *Circ Res*. 1992;71:490-502
79. Elzinga G, Westerhof N. Matching between ventricle and arterial load. An evolutionary process. *Circ Res*. 1991;68:1495-1500
80. O'Rourke MF. Toward optimization of wave reflection: Therapeutic goal for tomorrow? *Clinical and Experimental Pharmacology and Physiology*. 1996;23:s11-s15

81. Levenson J, Simon A, Cambien F, Beretti C. Cigarette smoking and hypertension. Factors independently associated with blood hyperviscosity and arterial rigidity. *Arterioscler Thromb Vasc Biol*. 1987;7:572-577
82. Levent E, Ozyürek AR, Ülger Z. Evaluation of aortic stiffness in tobacco-smoking adolescents. *Journal of Adolescent Health*. 2004;34:339-343
83. Stefanadis C, Tsiamis E, Vlachopoulos C, Stratos C, Toutouzas K, Pitsavos C, Marakas S, Boudoulas H, Toutouzas P. Unfavorable effect of smoking on the elastic properties of the human aorta. *Circulation*. 1997;95:31-38
84. Giannattasio C, Mangoni AA, Stella ML, Carugo S, Grassi G, Mancia G. Acute effects of smoking on radial artery compliance in humans. *Journal of Hypertension*. 1994;12:691-696
85. Kool MJF, Hoeks APG, Struijker Boudier HAJ, Reneman RS, Van Bortel LMAB. Short and long-term effects of smoking on arterial wall properties in habitual smokers. *Journal of the American College of Cardiology*. 1993;22:1881-1886
86. Mahmud A, Feely J. Effect of smoking on arterial stiffness and pulse pressure amplification. *Hypertension*. 2003;41:183-187
87. Feldman MD, Alderman JD, Aroesty JM, Royal HD, Ferguson JJ, Owen RM, Grossman W, McKay RG. Depression of systolic and diastolic myocardial reserve during atrial pacing tachycardia in patients with dilated cardiomyopathy. *The Journal of Clinical Investigation*. 1988;82
88. Laniado S, Yellin E, Yoran C, Strom J, Hori M, Gabbay S, Terdiman R, Frater R. Physiologic mechanisms in aortic insufficiency. I. The effect of changing heart rate on flow dynamics. Ii. Determinants of austin flint murmur. *Circulation*. 1982;66:226-235
89. Ohte N, Cheng C-P, Little WC. Tachycardia exacerbates abnormal left ventricular–arterial coupling in heart failure. *Heart and Vessels*. 2003;18:136-141
90. Westerhof N, O'Rourke MF. Haemodynamic basis for the development of left ventricular failure in systolic hypertension and for its logical therapy. *Journal of Hypertension*. 1995;13:943-952
91. Jung E, Peskin CS. Two-dimensional simulations of valveless pumping using the immersed boundary method. *SIAM Journal on Scientific Computing*. 2002; 23:19-45
92. Davies JE, Whinnett ZI, Francis DP, Manisty CH, Aguado-Sierra J, Willson K, Foale RA, Malik IS, Hughes AD, Parker KH, Mayet J. Evidence of a dominant backward-propagating "suction" wave responsible for diastolic coronary filling in humans, attenuated in left ventricular hypertrophy. *Circulation*. 2006;113:1768-1778
93. Ishikawa J, Matsui Y, Russo C, Hyodo E, Arai K, DiTulio MR, Homma S, Kario K. Increased aortic wave reflection and longitudinal regional diastolic dysfunction in patients with left ventricular hypertrophy. *Artery Research*. 2012;6:97-102
94. Manisty C, Mayet J, Tapp RJ, Parker KH, Sever P, Poulter NH, Thom SAM, Hughes AD. Wave reflection predicts cardiovascular events in hypertensive individuals independent of blood pressure and other cardiovascular risk factors: An ASCOT (anglo-Scandinavian Cardiac Outcome Trial) substudy. *Journal of the American College of Cardiology*. 2010;56:24-30
95. Pahlevan NM, Gharib M. Aortic wave dynamics and its influence on left ventricular workload. *PLoS ONE*. 2011;6:e23106
96. Attinger EO. Pulsatile blood flow. 1964
97. Knight GEW, Wolstenholme J. *Circulatory and respiratory mass transport*. Ciba Foundation; 1971.
98. Milnor WR. Aortic wavelength as a determinant of the relation between heart rate and body size in mammals. *Am J Physiol Regul Integr Comp Physiol*. 1979;237:R3-6

99. O'Rourke M, Yaginuma T, Avolio A. Physiological and pathophysiological implications of ventricular/vascular coupling. *Annals of Biomedical Engineering*. 1984;12:119-134

100. Li JK, Noordergraaf A. Similar pressure pulse propagation and reflection characteristics in aortas of mammals. *American Journal of Physiology - Regulatory, Integrative and Comparative Physiology*. 1991;261:R519-R521

101. Westerhof N, Elzinga G. Normalized input impedance and arterial decay time over heart period are independent of animal size. *American Journal of Physiology - Regulatory, Integrative and Comparative Physiology*. 1991;261:R126-R133

102. Quick CM, Berger DS, Noordergraaf A. Constructive and destructive addition of forward and reflected arterial pulse waves. *American Journal of Physiology - Heart and Circulatory Physiology*. 2001;280:H1519-H1527

103. Westerhof N, Stergiopulos N, Noble MIM. *Snapshots of hemodynamics: An aid for clinical research and graduate education*. Springer; 2005.

104. Zamir M. Mechanics of blood supply to the heart: Wave reflection effects in a right coronary artery. *Proceedings of the Royal Society of London. Series B: Biological Sciences*. 1998;265:439-444

105. Li JK-J. *Dynamics of the vascular system*. World Scientific Pub Co Inc; 2004.

106. Adolph EF. Quantitative relations in the physiological constitutions of mammals. *Science*. 1949;109:579-585

107. Holt JP, Rhode EA, Holt WW, Kines H. Geometric similarity of aorta, venae cavae, and certain of their branches in mammals. *American Journal of Physiology - Regulatory, Integrative and Comparative Physiology*. 1981;241:R100-R104

108. Li JK-J. *Comparative cardiovascular dynamics of mammals*. CRC Press; 1995.

109. Segers P, Rietzschel ER, Buyzere MLD, Bacquer DD, Bortel LMV, Backer GD, Gillebert TC, Verdonck PR. Assessment of pressure wave reflection: Getting the timing right! *Physiological Measurement*. 2007;28:1045

110. Altman PL, Dittmer DS. Respiration and Circulation. 1971

111. Noordergraaf A, Li JKJ, Campbell KB. Mammalian hemodynamics : A new similarity principle. *Journal of Theoretical Biology*. 1979;79:485-489

112. Avolio A, O'rourke M, Mang K, Bason P, Gow B. A comparative study of pulsatile arterial hemodynamics in rabbits and guinea pigs. *American Journal of Physiology -- Legacy Content*. 1976;230:868-875

113. Davies JE, Parker KH, Francis DP, Hughes AD, Mayet J. What is the role of the aorta in directing coronary blood flow? *Heart*. 2008;94:1545-1547

114. Zamir M. *The physics of coronary blood flow*. Springer; 2005.

115. Flores J, Corvera Poiré E, del Río JA, López de Haro M. A plausible explanation for heart rates in mammals. *Journal of Theoretical Biology*. 2010;265:599-603

116. Propst G. Pumping effects in models of periodically forced flow configurations. *Physica D: Nonlinear Phenomena*. 2006;217:193-201

117. Takagi S, Saijo T. Study of a piston pump without valves : 1st report, on a pipe-capacity-system with a t-junction. *Bulletin of JSME*. 1983;26 1366-1372

118. Takagi S, Takahashi K. Study of a piston pump without valves : 2nd report, pumping effect and resonance in a pipe-capacity-system with a t-junction. *Bulletin of JSME*. 1985;28:831-836

119. Pahlevan NM, Gharib M. Low pulse pressure with high pulsatile external left ventricular power: Influence of aortic waves. *Journal of biomechanics*. 2011;44:2083-2089

120. Mann DL, Bristow MR. Mechanisms and models in heart failure: The biomechanical model and beyond. *Circulation*. 2005;111:2837-2849

121. Denardo SJ, Nandyala R, Freeman GL, Pierce GL, Nichols WW. Pulse wave analysis of the aortic pressure waveform in severe left ventricular systolic dysfunction. *Circulation: Heart Failure*. 2009

122. Bedford DE. The ancient art of feeling the pulse. *British Heart Journal*. 1951;13:423

123. Fields A. The pulse in ancient chinese medicine. *California Medicine*. 1947;66:304

124. Avolio AP, Butlin M, Walsh A. Arterial blood pressure measurement and pulse wave analysis—their role in enhancing cardiovascular assessment. *Physiological Measurement*. 2010;31:R1

125. Garcia D, Barenbrug PJC, Pibarot P, Dekker ALAJ, van der Veen FH, Maessen JG, Dumesnil JG, Durand L-G. A ventricular-vascular coupling model in presence of aortic stenosis. *American Journal of Physiology - Heart and Circulatory Physiology*. 2005;288:H1874-H1884

126. Wang Y-YL, Sze W-K, Bau J-G, Wang S-H, Jan M-Y, Hsu T-L, Wang W-K. The ventricular-arterial coupling system can be analyzed by the eigenwave modes of the whole arterial system. *Applied Physics Letters*. 2008;92:153901-153903

127. Huang NE, Shen Z, Long SR, Wu MC, Shih HH, Zheng Q, Yen N-C, Tung CC, Liu HH. The empirical mode decomposition and the Hilbert spectrum for nonlinear and non-stationary time series analysis. *Proceedings of the Royal Society of London. Series A: Mathematical, Physical and Engineering Sciences*. 1998;454:903-995

128. Hou TY, Shi Z. Adaptive data analysis via sparse time-frequency representation. *Advances in Adaptive Data Analysis*. 2011;3:1-28

129. Hou TY, Shi Z. Data-driven time–frequency analysis. *Applied and Computational Harmonic Analysis*. 2012

130. Huang W, Shen Z, Huang NE, Fung YC. Engineering analysis of biological variables: An example of blood pressure over 1 day. *Proceedings of the National Academy of Sciences*. 1998;95:4816-4821

131. Huang W, Shen Z, Huang NE, Fung YC. Use of intrinsic modes in biology: Examples of indicial response of pulmonary blood pressure to ± step hypoxia. *Proceedings of the National Academy of Sciences*. 1998;95:12766-12771

132. Daubechies I. The wavelet transform, time-frequency localization and signal analysis. *Information Theory, IEEE Transactions on*. 1990;36:961-1005

133. Harmon KG, Asif IM, Klossner D, Drezner JA. Incidence of sudden cardiac death in national collegiate athletic association athletes / clinical perspective. *Circulation*. 2011;123:1594-1600

134. Katcher MS, Salem DN, Wang PJ, EstesIII NAM. Mechanisms of sudden cardiac death in the athlete. In: EstesIII NAM, Salem DN, Wang PJ, eds. *Sudden Cardiac Death in the Athlete*. Futura Publishing Company; 1998:3-24.

135. Myerburg RJ, Mitrani R, Interian A, Castellanos A. Identification of risk of cardiac arrest and sudden cardiac death in athletes. In: EstesIII NAM, Salem DN, Wang PJ, eds. *Sudden Cardiac Death in the Athlete*. Futura Publishing Company; 1998:25-55.

136. Virmani R, Burke AP, Farb A. Sudden cardiac death. *Cardiovascular Pathology*. 2001;10:211-218

137. Virmani R, Burke AP, Farb A, Kark JA. Causes of sudden death in young and middle-aged competitive athletes. *Cardiology Clinics*. 1997;15:439-466

138. Davies JE, Francis DP, Hadjiloizou N, Whinnett ZI, Manisty CH, Aguado-Sierra J, Malik IS, Parker KH, Hughes AD, Mayet J. Augmentation of coronary blood flow in systole by reflected waves in the proximal aorta. In: Dössel O, Schlegel WC, eds. *Ifmbe proceedings, world congress on medical physics and biomedical engineering*. Springer Berlin Heidelberg; 2010:61-64.

139. Link MS, Maron BJ, EstesIII NAM. Commotio cordis. In: EstesIII NAM, Salem DN, Wang PJ, eds. *Sudden Cardiac Death in the Athlete*. Futura Publishing Company; 1998:515-528.

140. Lindsay RB. *Mechanical Radiation*. McGraw-Hill; 1960.